Karlsruhe Institute of Technology

Optimization of a KATRIN source analysis tool and investigations of the potential to constrain the relic neutrino background

Master Thesis of

Florian Heizmann

At the Department of Physics
Institute of Experimental Nuclear Physics

Reviewer:	Prof. G. Drexlin
Second reviewer:	Prof. U. Husemann
Advisor:	Dr. K. Valerius
Second advisor:	Dr. M. Babutzka

January 2015

ABSTRACT

The KArlsruhe TRItium Neutrino (KATRIN) experiment – currently under construction at KIT – will determine the neutrino mass with an unprecedented sensitivity of 200 meV at 90 % C.L. by high-precision tritium β-decay spectroscopy.

In order to reach this new level of neutrino mass sensitivity it is very important to understand the tritium source properties and the related systematic measurement uncertainties. Therefore, in the scope of this thesis, the electromagnetic design of a source analysis tool is optimized. Furthermore, the unique tritium source opens up the possibility to search for the elusive relic neutrinos, at least to set limits on the local relic neutrino overdensity, in a laboratory experiment. The potential of KATRIN to set those limits is also explored in this thesis.

Das KArlsruhe TRItium Neutrino (KATRIN) Experiment – welches sich momentan im Aufbau am KIT befindet – ist konstruiert, um mittels hochauflösender β-Zerfall Spektroskopie die Neutrinomasse mit einer bisher unerreichten Sensitivität von 200 meV zu 90 % C.L. zu bestimmen.

Das Erreichen dieses Sensitivitätsziels erfordert ein detailliertes Verständnis der Eigenschaften der Quelle und der damit verbundenen systematischen Messunsicherheiten. Im Rahmen dieser Arbeit wurde zu diesem Zweck das elektromagnetische Design eines Quellanalyseinstruments optimiert. Die einzigartige Tritiumquelle ermöglicht zudem die Suche nach sogenannten Urknallneutrinos; zumindest eine obere Grenze für eine mögliche lokale Überdichte des Neutrinohintergrundes sollte mit diesem Laborexperiment gesetzt werden können. Das Potential von KATRIN, Modelle bezüglich des Neutrinohintergrundes zu testen, wird in dieser Arbeit ebenfalls untersucht.

CONTENTS

Abstract iii

1. Introduction 1

2. Neutrino physics 3
2.1. The postulation & discovery of the neutrino . . . 3
2.2. Neutrinos in the Standard Model of particle physics . . . 5
2.3. Extension of the Standard Model of particle physics . . . 5
2.3.1. Neutrino oscillations . . . 6
2.3.2. Neutrino mass generation . . . 10
2.4. Determination of the neutrino mass . . . 13
2.4.1. Model-dependent measurements . . . 13
2.4.2. Model-independent measurements . . . 16

3. The KArlsruhe TRItium Neutrino Experiment 21
3.1. Neutrino Mass from tritium beta-decay . . . 21
3.2. Components of the KATRIN experiment . . . 22
3.2.1. Source section – WGTS . . . 22
3.2.2. Transport section – DPS and CPS . . . 23
3.2.3. Spectrometer section – pre- and main spectrometer . . . 24
3.2.4. Detector section . . . 28
3.2.5. Rear Section . . . 28
3.3. Monitoring and impact of tritium source parameters . . . 28

4. Electromagnetic Design for the Rear Section of the KATRIN Experiment 31
4.1. Requirements for the electromagnetic design of the Rear Section . . . 31
4.2. Electromagnetic components . . . 32
4.2.1. Magnets . . . 33
4.2.2. Electrodes . . . 36
4.3. KASSIOPEIA . . . 40
4.3.1. Usage of KASSIOPEIA . . . 40
4.3.2. Geometry definition . . . 40
4.3.3. Field computation . . . 41
4.3.4. Particle tracking . . . 44

4.4. Simulations . . . 46
4.4.1. Tracking performance optimization . . . 46
4.4.2. Performance tests . . . 49
4.4.3. Optimization of electron gun parameters . . . 50
4.5. Summary . . . 53

5. Cosmic Neutrino Background 57
5.1. Theory of the cosmic neutrino background . . . 58
5.1.1. Cosmic microwave background cosmology . . . 58
5.1.2. Cosmic neutrino background cosmology . . . 61
5.1.3. Detection of cosmic neutrino background . . . 65
5.2. Signal identification of the cosmic neutrino background at KATRIN . 69
5.2.1. Energy resolution . . . 70
5.2.2. Doppler effect . . . 71
5.2.3. Final state distribution . . . 71
5.3. Signal implementation of the cosmic neutrino background . . . 73
5.3.1. SSC and KaFit . . . 74
5.3.2. Statistical methods . . . 75
5.3.3. FSD implementation . . . 77
5.3.4. Implementation challenges . . . 78
5.3.5. Implementation result . . . 79
5.4. Sensitivity of KATRIN for measuring the cosmic neutrino background 80
5.4.1. Sensitivity for the cosmic neutrino background overdensity . . 81
5.4.2. Sensitivity for the neutrino mass . . . 82
5.4.3. Cosmic neutrino background overdensity systematics . . . 83
5.4.4. Discussion of the results . . . 84
5.5. Summary . . . 86

6. Conclusions & Outlook 89

A. Rear Section geometry definitions of components 91
A.1. Beam tube geometry definition . . . 91
A.2. E-gun geometry definition . . . 93
A.3. Post acceleration geometry definitions . . . 97
A.4. Electric dipole electrodes geometry definitions . . . 99
A.5. Solenoid geometry definitions . . . 100
A.6. Magnetic dipoles geometry definitions . . . 102

B. Rear Section assembly of components 105
B.1. Rear Section complete geometry . . . 105
B.2. Rear Section object properties . . . 107

C. Rear Section simulation 113

D. Rear Section settings 121

Bibliography 131

List of Acronyms 139

Acknowledgements **141**

CHAPTER 1

INTRODUCTION

Since the postulation of the neutrino in 1930 [PKW64] and its first detection in 1953 [RC53], neutrino physics has developed into an active and continuously growing research field. Since then, many properties of these particles have been measured. The present neutrino model consists of three active neutrinos, participating only in the weak interaction due to the fact that they carry neither electric nor color charge. Oscillation experiments showed that there is evidence for a yet unknown but nonzero neutrino mass [F^+98, A^+01]. The strongest neutrino mass limits today come from tritium β-decay experiments at Mainz and Troitsk [Oli14].

The KArlsruhe TRItium Neutrino (KATRIN) experiment aims to measure the neutrino mass with unprecedented sensitivity of 200 meV at 90 % C.L. The main foundations for this factor 10 improvement in neutrino mass sensitivity with respect to previous experiments are an ultra-luminous tritium source combined with high precision β spectroscopy. Since the observable in β-decay experiments is the squared neutrino mass, this requires an overall improvement of statistical and systematic uncertainties of a factor 100. In order to achieve this goal, the properties of the KATRIN source and transport section (STS) will be continuously measured by the calibration and monitoring systems (CMS). As part of the CMS, the so-called "Rear Section" is designated to serve as a versatile tritium source analysis tool.

To enable various calibration procedures for the KATRIN experiment the Rear Section must provide an electron beam with precisely known characteristics. The properties of this beam strongly depend on the electromagnetic design (EMD) of the Rear Section. Therefore, previous EMD simulations are re-evaluated and extended in this thesis by the implementation of the Rear Section into the most recent KATRIN particle tracking software Kassiopeia.

Furthermore, the large amount of tritium in the gaseous source enables the search for relic neutrinos forming a cosmic neutrino background (CνB), the neutrino pendant to the cosmic microwave background (CMB). This CνB originates 1 s after the Big Bang, providing a time window very close to the origin of the universe. Today, these neutrinos are non-relativistic due to their rest mass, motivating models of relic neutrino clustering [RW04] which may result in a local relic neutrino overdensity. Up to now, the most promising method for relic neutrino detection seems to be

induced β-decay [KFM10], since the process does not involve a kinematic threshold. Therefore, the KATRIN experiment with its ultra-luminous tritium source – though not a dedicated CνB experiment – will be in a prime position to constrain the local relic neutrino overdensity, as will be shown in this thesis.

In chapter 2, a brief introduction to neutrino physics is given. It recapitulates the status of this broad field of particle physics, including the role of the neutrinos in the Standard Model of particle physics, neutrino oscillations and recent neutrino mass experiments. Chapter 3 gives an overview of the next generation neutrino mass experiment KATRIN. Briefly, the measuring principle of KATRIN and its main components are explained. Furthermore, the purpose and role of the source analysis tool Rear Section in the context of the KATRIN experiment is outlined. After introducing the Rear Section, its EMD properties are discussed in chapter 4. To this end, the implementation of the Rear Section into the most recent KATRIN particle simulation software Kassiopeia is explained in detail. By this implementation, optimizations for the EMD of the Rear Section are enabled. Subsequently, in chapter 5, the properties of KATRIN's unique tritium source are exploited to investigate the sensitivity of the experiment for constraining the CνB. The thesis closes with a recapitulation of the conducted work and an outlook on future developments in chapter 6.

CHAPTER 2

NEUTRINO PHYSICS

The KATRIN experiment wants to achieve an unprecedented sensitivity on the neutrino mass of 200 meV. The determination will be a direct, model-independent measurement of the neutrino mass scale by investigating the kinematics of tritium β-decay. This chapter aims to set the KATRIN experiment in the context of neutrino physics, starting with a short chronological overview including the postulation and discovery of the neutrino, given in sec. 2.1. The recent discovery of a Higgs-Boson with a mass of 125.7 GeV (see fig. 2.1) was a strong hint for the validity of the Standard Model of particle physics (SM). However, neutrinos are massless in the SM (sec. 2.2) which is clearly at odds with the observation of neutrino flavor oscillations (sec. 2.3.1). The fact that neutrinos have non-vanishing masses hence provides evidence for physics beyond the SM, in the sense that an extension of the SM is required (sec. 2.3). In sec. 2.4 finally, several approaches to determine the nonzero neutrino mass are presented.

2.1. The postulation & discovery of the neutrino

"I have done a terrible thing, I have postulated a particle that cannot be detected."
- Wolfgang Pauli, 1930 -

Soon after postulating a new particle in order to explain the measured continuous β-decay spectrum [PKW64], Wolfgang Pauli recognized the trouble with proving its existence due to the particles properties. At that time, the only particles observed during β-decay were the decaying nucleus, the daughter nucleus and the electron. If these were all the participating particles, the spectrum of the electron would be a mono-energetic line at the decay energy as for α- and γ-decay. By contrast, the measured electron spectrum was continuous [Cha14], so another particle was needed to explain the spectrum shape. This new particle was supposed to be neutral and to have spin 1/2 to fulfill energy and (angular) momentum conservation:

$$ {}^{A}_{Z}N \rightarrow {}^{A}_{Z+1}N' + \mathrm{e}^- + \bar{\nu}_\mathrm{e} \qquad \text{and} \qquad {}^{A}_{Z}N \rightarrow {}^{A}_{Z-1}N' + \mathrm{e}^+ + \nu_\mathrm{e} \tag{2.1} $$

Because of its electric and color neutrality, the new particle only interacts weakly, making it very hard to detect. The theory of the β-decay and weak interaction of the neutrinos was first developed by Enrico Fermi in 1934 [Fer34]. It was also Fermi who changed the name of the new particle from Pauli's initial 'neutron' to its present value, after James Chadwick discovered the neutron in 1932 [Cha32]. With some extensions, Fermi's point-like interaction of four particles is still valid today and known as theory of weak interaction. It is the postulated small cross section $\sigma < 10^{-44}\,\mathrm{cm}^2$ [BP34] that prevented an experimental detection of the neutrino until the "Poltergeist" experiment of Cowan and Reines [RC53]. They used the inverse β-decay reaction

$$\bar{\nu}_\mathrm{e} + \mathrm{p} \rightarrow \mathrm{e}^+ + \mathrm{n} \tag{2.2}$$

in water with electron anti-neutrinos from the Savannah River nuclear reactor. After adding cadmium chloride to the water, the signal of the interacting $\bar{\nu}_\mathrm{e}$ was very characteristic: The positron e^+ quickly finds an electron and they annihilate into two 511 keV gamma rays. The neutron slows down within a few microseconds due to collisions with the molecules in the tank and is then captured by the highly effective neutron absorber cadmium. The excited cadmium nucleus Cd* relaxes to its ground state via emission of a gamma ray, so the characteristic signal consisted of the two 511 keV gamma rays together with the five microseconds delayed gamma ray from the deexcitation. This allowed for a very easy ν-signal identification and lead to a cross section of $\sigma = \left(1.2^{+0.7}_{-0.4}\right) \cdot 10^{-43}\,\mathrm{cm}^2$ [RCH$^+$60] which is an order of magnitude larger than the cross section postulated by Bethe and Peierls 1934 [BP34].
In 1962, a second type of neutrino was discovered at the Brookhaven National Laboratory [DGG$^+$62] when investigating the pion decay:

$$\pi^+ \rightarrow \mu^+ + \nu_\mu \qquad \text{and} \qquad \pi^- \rightarrow \mu^- + \bar{\nu}_\mu \tag{2.3}$$

The experiment demonstrated that the charged leptons created additional to the neutrino only were muons and no electrons. Therefore, Danby et al. concluded that their neutrinos, produced in the decay reactions eq. (2.3), were different from those produced in β-decay. This discovery was rewarded with the Nobel prize even before Reines got his Nobel prize for the discovery of the electron neutrino.
The neutrino family predicted by the SM was complete when the DONUT collaboration discovered a third neutrino 2001 [K$^+$01], different from the two before: the τ neutrino ν_τ. They used a proton beam to create a particle shower containing $\mathrm{D_S}$ mesons, which decay into τ and ν_τ leptons. The τ particle tracks have a typical kink like signature, due to the invisible ν_τ.
There were already hints for the existence of three types of neutrinos in 1989, when amongst others the ALEPH experiment compared the observed decay width of the Z^0 boson with the theoretical one [D$^+$89]. They found that the best fitting curve was the one with

$$N_\nu = 3.27 \pm 0.30, \tag{2.4}$$

ruling out speculations about a fourth light neutrino at 98 % C.L. However, there is still the possibility of additional sterile neutrinos, because they, by construction, do not participate in the weak interaction.

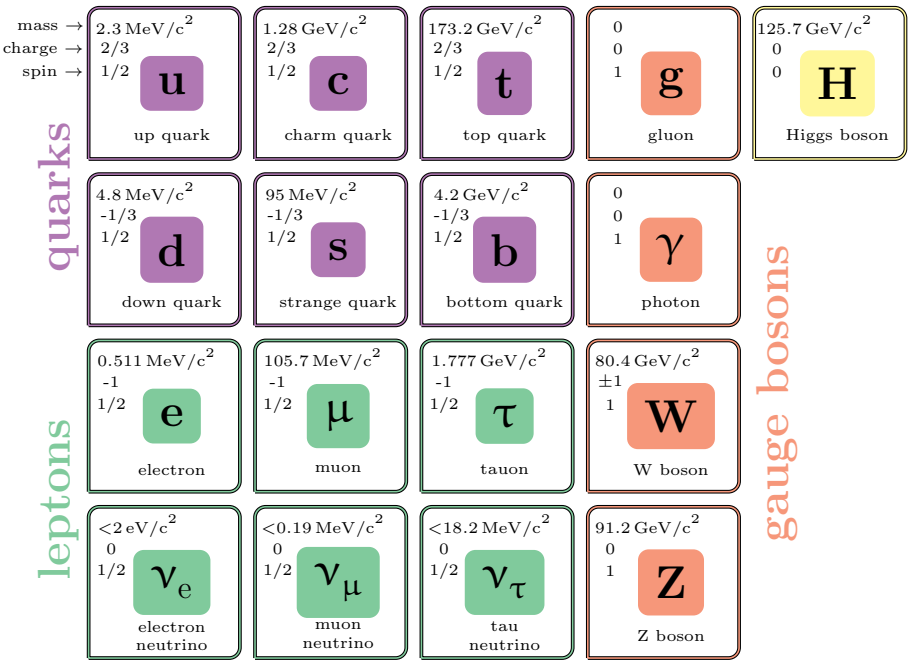

Figure 2.1.: **The Standard Model of particle physics** - It contains three generations of leptons and quarks (elementary particles of matter), four gauge bosons and the Higgs Boson. Particle properties adopted from [Oli14].

2.2. Neutrinos in the Standard Model of particle physics

The Standard Model of particle physics (fig. 2.1) today contains three generations of neutrinos. Together with the three charged leptons they form the three weak isospin doublets, transforming under the weak (SU2) symmetry. Neutrinos are stable, uncharged fermions and therefore only interact via the weak force, making them unique in the Standard Model of particle physics (SM): they are the only fermions which can be their own antiparticles. If so, the lepton number L would be violated by $\Delta L = 2$, which would be physics beyond the SM. In 1958, Goldhaber et al. measured the helicity of neutrinos to be $h_\nu = -1.0 \pm 0.3$ [GGS58], meaning that only left-handed neutrinos ($h_\nu = -1$) and right-handed anti-neutrinos ($h_{\bar{\nu}} = +1$) participate in the weak interaction. From this maximum violation of parity in the weak interaction it follows, that neutrinos are massless in the SM and travel at the speed of light: otherwise one might find a reference frame in which the momentum direction and therefore the helicity of the neutrino would be reversed.

2.3. Extension of the Standard Model of particle physics

Though the Standard Model of particle physics received another advantage in 2012 by the discovery of a Higgs-like particle [ATL12, CMS12], which was the last piece of the puzzle, the picture is still not complete: in the past two decades, the hints for massive neutrinos have been confirmed by measuring neutrino oscillations as shown in section 2.3.1. In section 2.3.2, an introduction to proposals for the mass generation of neutrinos is given.

2.3.1. Neutrino oscillations

Since the first results of the Homestake experiment [DHH68], physicists struggled with the so called "solar neutrino problem": the experimentalists found the flux of solar neutrinos to be only about 1/3 of the expected flux predicted by the standard solar model (SSM). It took until 2001 to resolve this problem and to show that the SSM was correct: the SNO experiment measured not only the charged current (CC) but also the neutral current (NC) and therefore was sensitive to all neutrino flavors [A$^+$01]. SNO made use of heavy water (D_2O), so the neutrinos could transform the deuterium either in two protons and one electron (CC, only possible for "not oscillated" electron neutrinos) or just break the deuterium into proton and neutron (NC, also possible for "oscillated" neutrinos):

$$\nu_e + D \to p + p + e^- \qquad \text{(CC)} \tag{2.5}$$

$$\nu_\alpha + D \to p + n + \nu_\alpha \qquad (\alpha = e, \mu, \tau) \qquad \text{(NC)} \tag{2.6}$$

Another milestone in neutrino oscillation investigation was the Super-Kamiokande experiment, which was amongst others measuring atmospheric neutrinos. Atmospheric neutrinos are products of the decay of pions, which originate from the collision of a cosmic ray particle (mainly protons) with a molecule of the atmosphere. Using a large water tank as target for the atmospheric neutrinos, the Super-Kamiokande experiment showed that there is a zenith angle dependent deficit of muon neutrinos, inconsistent with what was expected from the atmospheric neutrino flux [F$^+$98]. For the analysis, Fukuda et al. made use of the different signals of muons and electrons in a (water) Cherenkov detector: the muons form a sharp Cherenkov ring, whereas the electron signal results in a more diffuse ring, due to electromagnetic showering. The up-going muon neutrino deficit was interpreted as an oscillation of the form $\nu_\mu \to \nu_\tau$ since the electron neutrino rate was consistent with expectations.

Neutrino mixing

The theoretical formalism of neutrino oscillations was mainly developed during the 50's and 60's by Pontecorvo [Pon57, Pon58, Pon68] and Maki, Nakagawa and Sakata [MNS62]. Neutrinos are created in one of the three weak flavor eigenstates $|\nu_\alpha\rangle$ ($\alpha = e, \mu, \tau$) with well-defined weak interactions. To enable oscillations, these weak eigenstates must be superpositions of three mass eigenstates $|\nu_i\rangle$ ($i = 1, 2, 3$) with well-defined masses. The connection between these eigenstates can be described with a unitary matrix U:

$$|\nu_\alpha\rangle = \sum_i U^*_{\alpha i} |\nu_i\rangle \qquad \text{and} \qquad |\nu_i\rangle = \sum_\alpha U_{\alpha i} |\nu_\alpha\rangle \tag{2.7}$$

The unitary matrix can be thought of as a rotation matrix, in this case the so called PMNS matrix[1] U is a 3×3 matrix [E+04]:

$$U = \begin{bmatrix} U_{\mathrm{e}1} & U_{\mathrm{e}2} & U_{\mathrm{e}3} \\ U_{\mu 1} & U_{\mu 2} & U_{\mu 3} \\ U_{\tau 1} & U_{\tau 2} & U_{\tau 3} \end{bmatrix} \tag{2.8}$$

$$= \begin{bmatrix} c_{12}c_{13} & s_{12}c_{13} & s_{13}\mathrm{e}^{-\mathrm{i}\delta} \\ -s_{12}c_{23} - c_{12}s_{23}s_{13}\mathrm{e}^{\mathrm{i}\delta} & c_{12}c_{23} - s_{12}s_{23}s_{13}\mathrm{e}^{\mathrm{i}\delta} & s_{23}c_{13} \\ s_{12}s_{23} - c_{12}c_{23}s_{13}\mathrm{e}^{\mathrm{i}\delta} & -c_{12}s_{23} - s_{12}c_{23}s_{13}\mathrm{e}^{\mathrm{i}\delta} & c_{23}c_{13} \end{bmatrix} \cdot \begin{bmatrix} \mathrm{e}^{\mathrm{i}\alpha_1/2} & 0 & 0 \\ 0 & \mathrm{e}^{\mathrm{i}\alpha_2/2} & 0 \\ 0 & 0 & 1 \end{bmatrix}$$

with $s_{ij} = \sin\theta_{ij}$ and $c_{ij} = \cos\theta_{ij}$. The matrix contains up to six free parameters: three mixing angles ($\theta_{ij} = [0, \pi/2]$) and up to three CP-violation describing phases (δ, α_1, α_2), depending on the nature of neutrinos. The mixing angles represent the contribution of each mass eigenstate to a given flavor eigenstate (which also applies inversely). If neutrinos are Dirac particles, the only physical phase is the Dirac phase δ and if they are Majorana particles, the CP-violation in the lepton sector is induced by the two Majorana phases α_1 and α_2. Together with the three masses of the eigenstates, this – in the case of three neutrino mixing – leads to 7 or 9 fundamental parameters.
For the case of one additional sterile neutrino, the mixing matrix has to be extended to a 4×4 matrix. More generally, for the case of n neutrino flavors and n massive neutrinos, the mixing matrix (2.8) hast to be extended to a $n \times n$ matrix, with $n\,(n-1)\,/2$ mixing angles and $(n-1)\,(n-2)\,/2$ Dirac CP-phases or $(n-1)$ Majorana CP-phases [Ber12].

Theory of Neutrino oscillations

With the now given relation between the stationary mass eigenstates $|\nu_i\rangle$ and the weak eigenstates $|\nu_\alpha\rangle$ (2.8) it is possible to investigate the time evolution of a neutrino state. In one dimension, the propagation is described by the time-dependent Schrödinger equation

$$H\,|\nu_i(x,t)\rangle = \mathrm{i}\hbar\frac{\partial}{\partial t}\,|\nu_i(x,t)\rangle\,, \tag{2.9}$$

which has plane wave solutions:

$$|\nu_i(x,t)\rangle = \mathrm{e}^{-\frac{\mathrm{i}}{\hbar}(E_i t - p_i x)}\,|\nu_i\rangle \tag{2.10}$$

This time dependency of the mass eigenstates can now be used to find the time dependency of the flavor eigenstates:

$$\begin{aligned} |\nu_\alpha(x,t)\rangle &\overset{(2.7)}{=} \sum_i U^*_{\alpha i}\,|\nu_i(x,t)\rangle \overset{(2.10)}{=} \sum_i U^*_{\alpha i}\mathrm{e}^{-\frac{\mathrm{i}}{\hbar}(E_i t - p_i x)}\,|\nu_i\rangle \\ &\overset{(2.7)}{=} \sum_{i,\beta} U^*_{\alpha i}\mathrm{e}^{-\frac{\mathrm{i}}{\hbar}(E_i t - p_i x)}U_{\beta i}\,\big|\nu_\beta\big\rangle \end{aligned} \tag{2.11}$$

[1] The PMNS matrix is named after Pontecorvo, Maki, Nakagawa and Sakata who worked out the formalism for the neutrino oscillations

This shows that the pure neutrino flavor $|\nu_\alpha\rangle$ evolves into a superposition of flavor states $|\nu_\beta\rangle$ at times $t > 0$. The amplitude for this transition is

$$A_{\nu_\alpha \to \nu_\beta}(x,t) = \langle \nu_\beta \,|\, \nu_\alpha(x,t) \rangle \overset{(2.11)}{=} \sum_i U^*_{\alpha i} U_{\beta i} \mathrm{e}^{-\frac{\mathrm{i}}{\hbar}(E_i t - p_i x)} \,, \tag{2.12}$$

leading to a time- and spatial dependent probability for this transition of

$$\begin{aligned} P_{\nu_\alpha \to \nu_\beta}(x,t) &= \left| A_{\nu_\alpha \to \nu_\beta}(x,t) \right|^2 \\ &\overset{(2.12)}{=} \sum_{i,j} U^*_{\alpha i} U_{\beta i} U_{\beta j} U^*_{\beta j} \mathrm{e}^{-\frac{\mathrm{i}}{\hbar}(E_i t - p_i x)} \mathrm{e}^{\frac{\mathrm{i}}{\hbar}\left(E_j t - p_j x\right)}. \end{aligned} \tag{2.13}$$

All currently observed neutrinos can be treated in the ultra-relativistic limit, since their energies are at least in the MeV range and their masses less than 2 eV (see section 2.3.1), which leads to a Lorentz factor larger than 10^6 for all combinations. In the ultra-relativistic limit, neutrinos travel at the speed of light, $v \approx c$, and thus

$$m_i c^2 \ll p_i c \approx E. \tag{2.14}$$

This justifies performing a Taylor expansion around 0:

$$\begin{aligned} E_i = \sqrt{m_i^2 c^4 + p_i^2 c^2} = p_i c \sqrt{\frac{m_i^2 c^4}{p_i^2 c^2} + 1} \qquad \Bigg| \text{ using } \ \frac{m_i^2 c^4}{p_i^2 c^2} \to 0 \\ \approx p_i c \cdot \left(1 + \frac{1}{2} \frac{m_i^2 c^4}{p_i^2 c^2} \right) \overset{(2.14)}{=} p_i c + \frac{m_i^2 c^4}{2E}. \end{aligned} \tag{2.15}$$

With this approximation for the energy and traveled distance of the neutrinos

$$x = L = v \cdot t \approx c \cdot t, \tag{2.16}$$

the exponent of the plane wave solutions eq. (2.10) is writable as

$$E_i t - p_i x \overset{(2.15)}{\overset{(2.16)}{=}} \left(p_i c + \frac{m_i^2 c^4}{2E} \right) \cdot t - p_i L \overset{(2.16)}{=} \frac{m_i^2 c^4}{2E} \cdot t \overset{(2.16)}{=} \frac{m_i^2 c^3}{2} \frac{L}{E}. \tag{2.17}$$

This leads to a more convenient expression for the transition probability eq. (2.13) :

$$P_{\nu_\alpha \to \nu_\beta}(x,t) \overset{(2.17)}{=} \sum_{i,j} U^*_{\alpha i} U_{\beta i} U_{\beta j} U^*_{\beta j} \mathrm{e}^{-\frac{\mathrm{i}}{\hbar} \frac{\Delta m_{ij}^2 c^3}{2} \frac{L}{E}} \tag{2.18}$$

$$\begin{aligned} &= \delta_{\alpha\beta} - 4 \sum_{i>j} \mathrm{Re}\left(U^*_{\alpha i} U_{\beta i} U_{\beta j} U^*_{\beta j} \right) \sin^2 \left(\frac{\Delta m_{ij}^2 c^3}{4\hbar} \frac{L}{E} \right) \\ &\qquad + 2 \sum_{i>j} \mathrm{Im}\left(U^*_{\alpha i} U_{\beta i} U_{\beta j} U^*_{\beta j} \right) \sin \left(\frac{\Delta m_{ij}^2 c^3}{2\hbar} \frac{L}{E} \right) \end{aligned} \tag{2.19}$$

$$= P_{\nu_\alpha \to \nu_\beta}(L,E) \tag{2.20}$$

with $\Delta m_{ij}^2 = m_i^2 - m_j^2$. For a system with two flavors, this formula eq. (2.19) simplifies to

$$P_{\nu_\alpha \to \nu_\beta}(L,E) = \sin^2(2\theta) \sin^2 \left(\frac{\Delta m^2 c^3}{4\hbar} \frac{L}{E} \right) \tag{2.21}$$

Table 2.1.: **Experimental results of the neutrino oscillation parameters** - Values obtained through three neutrino mixing scheme using results of several experiments [Oli14]. The values for $\sin^2(2\theta_{23})$ and Δm^2_{32} are the ones from assuming normal neutrino mass hierarchy.

parameter	value	source
$\sin^2(2\theta_{12})$	0.846 ± 0.021	sun, reactor, accelerator
Δm^2_{21}	$(7.53 \pm 0.18) \cdot 10^{-5}\,\mathrm{eV}^2$	sun, reactor, accelerator
$\sin^2(2\theta_{23})$	$0.999^{+0.001}_{-0.018}$	atmosphere, accelerator
$\lvert\Delta m^2_{32}\rvert$	$(2.44 \pm 0.06) \cdot 10^{-3}\,\mathrm{eV}^2$	atmosphere, accelerator
$\sin^2(2\theta_{13})$	$(9.3 \pm 0.8) \cdot 10^{-2}$	reactor

with the mixing angle θ and the mixing matrix

$$U = \begin{bmatrix} \cos\theta & \sin\theta \\ -\sin\theta & \cos\theta \end{bmatrix}. \tag{2.22}$$

With this new form of the transition probability eq. (2.21), the oscillation mechanism can be understood intuitively: The heavier mass eigenstates travel at lower speed than the lighter ones, and since the mass eigenstates are superpositions of flavor eigenstates, there will be interference between the corresponding flavor components of each mass eigenstate. This makes it possible to detect a neutrino created in a flavor state α as neutrino of flavor β with the probability given in equations eq. (2.19) and (2.21) respectively. The probability of detecting the same neutrino flavor is then simply

$$P_{\nu_\alpha \to \nu_\alpha}(L, E) = 1 - P_{\nu_\alpha \to \nu_\beta}(L, E). \tag{2.23}$$

The amplitude of the oscillation is defined by the mixing angle θ_{ij}, while the frequency is defined by the mass difference Δm^2_{ij} of the mass eigenstates. The characteristic oscillation length, describing the distance for one full oscillation cycle, is then (in the two flavor case):

$$L_{\mathrm{osc}} = \frac{4\pi\hbar\, E}{\Delta m^2 c^3} \tag{2.24}$$

Knowing the traveled distance L and the energy of the neutrinos E makes it possible to determine the mixing parameters, so oscillation experiments make use of a neutrino beam with a known energy and a fixed distance between detector and source.

Experimental results

An overview of the current status of the oscillation parameters is given in tab. 2.1. Nowadays, direct measurements of θ_{13} make use of reactor $\bar{\nu}_e$ disappearance at short base lines of $L \approx 1\,\mathrm{km}$, corresponding to the squared mass difference Δm^2_{32}. The value for $\sin^2(2\theta_{13})$ given in tab. 2.1 roughly matches $\theta_{13} \approx 10°$, which is the smallest

of the mixing angles.
θ_{12} and Δm^2_{21} are traditionally associated with solar neutrinos and therefore called solar neutrino mixing parameters, whereas θ_{23} and Δm^2_{32} were mainly determined by atmospheric neutrino experiments and therefore called atmospheric neutrino mixing parameters.
The solar neutrino experiments mainly use the Cherenkov detection technique and found a large, but not maximal mixing angle of $\theta_{12} \approx 33°$ and a small squared mass difference Δm^2_{21} of the order $10^{-5}\,\mathrm{eV}^2$. The results were confirmed and slightly improved to the values given in tab. 2.1 by reactor and accelerator disappearance experiments.
First atmospheric neutrino mixing results came from experiments also working with the Cherenkov detection technique and were later on constrained further by accelerator disappearance experiments. Compared to the solar neutrino mixing parameters, the atmospheric ones both are larger: θ_{23} is close to maximum mixing and the largest of the mixing angles, the value given in tab. 2.1 corresponds to $\theta_{23} \approx 44°$. The squared mass difference is also larger than the solar neutrino one, namely two orders of magnitude ($\left|\Delta m^2_{23}\right|$ is of the order $10^{-3}\,\mathrm{eV}^2$). But up to now, the sign of this mass difference relative to Δm^2_{21} as well as the absolute mass scale of the neutrinos are not fixed. Using $\Delta m^2_{21} > 0$ and $\Delta m^2_{21} \ll \left|\Delta m^2_{23}\right|$ allows for three cases of neutrino mass ordering:

- **Normal hierarchy**: $m_1 < m_2 \ll m_3$
- **Inverted hierarchy**: $m_3 \ll m_1 < m_2$
- **Quasi-degenerated**: $m_1 \approx m_2 \approx m_3 \approx m_0$

Two of these cases are shown in fig. 2.2, the quasi-degenerated case is not shown. The vertical axes of fig. 2.2 are interrupted, because neither in the normal hierarchical case nor the inverted hierarchical case oscillation experiments can address the absolute value of the neutrino mass. For measuring the absolute neutrino mass scale, a different approach is needed (see sec. 2.4).

2.3.2. Neutrino mass generation

Before turning into neutrino mass determination, let us first consider some aspects of how theoretical models describe the neutrino mass generation. In the Standard Model of particle physics (SM), massive particles get their mass by coupling to the Higgs field ϕ. The Higgs field is a four-component scalar field, forming a complex doublet of weak isospin symmetry (SU(2)):

$$\phi = \frac{1}{\sqrt{2}} \begin{pmatrix} \phi^1 + \mathrm{i}\phi^2 \\ \phi^0 + \mathrm{i}\phi^3 \end{pmatrix}. \tag{2.25}$$

This field has several ground states, related to each other by SU(2) gauge transformations. Choosing now a gauge such that $\phi^1 = \phi^2 = \phi^3 = 0$ yields only one ground state, which equals the vacuum expectation value of ϕ^0

$$\langle \phi^0 \rangle = v \tag{2.26}$$

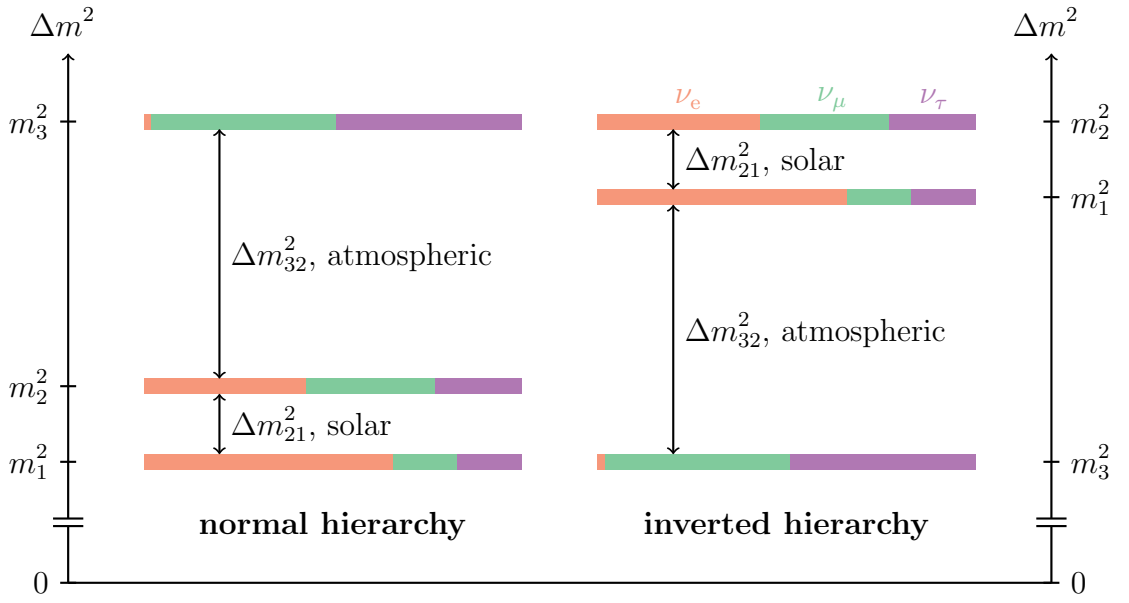

Figure 2.2.: **Neutrino mass hierarchy** - On the left, the normal hierarchy is shown and on the right the inverted hierarchy; the quasi-degenerated case is not shown. The squared mass differences are not true to scale; in this scheme, the solar squared mass difference Δm^2_{21} is comparatively large. The different colors mark the neutrino mixing: Orange for electron flavor, green for muon flavor and purple for tau flavor. Note that the electron flavor part for the third mass eigenstate m_3^2 is very small but not zero.

and has units of mass (so it is the only free parameter in the SM that is not dimensionless). The coupling of the Higgs field is now a Yukawa coupling:

$$\mathcal{L}_{\text{Yukawa}} = -G_\psi \bar{\psi} \phi \psi. \tag{2.27}$$

With this form of coupling, the Lagrangian for a fermion coupling to the Higgs field becomes

$$\mathcal{L}_{\text{Fermion}}(\phi, A, \psi) = \bar{\psi} \gamma^\mu D_\mu \psi + G_\psi \bar{\psi} \phi \psi, \tag{2.28}$$

with D_μ being the gauge covariant derivative. The equation of motion is now given by the Euler-Lagrange mechanism:

$$\frac{\partial \mathcal{L}}{\partial(\partial_\mu \psi)} - \frac{\partial \mathcal{L}}{\partial \psi} = 0. \tag{2.29}$$

Applying eq. (2.29) to the Fermion-Higgs Lagrangian eq. (2.28), using left- and right-handed currents ($\psi = \psi_\text{L} + \psi_\text{R}$) and the right-handed projection operator $\frac{1+\gamma^5}{2}$ leads to the equation of motion for a fermion, coupling to the Higgs field:

$$\mathrm{i}\partial\!\!\!/ \psi_\text{L} - \frac{G_\psi}{\sqrt{2}} \begin{pmatrix} 0 \\ v \end{pmatrix} \psi_\text{R} = 0. \tag{2.30}$$

To now identify the mass term, one needs to compare this equation of motion to the Dirac equation, which describes fermions:

$$(\mathrm{i}\partial\!\!\!/ - m)\, \psi = 0. \tag{2.31}$$

Repeating the steps above makes the comparison easier and results in a slightly different form of the Dirac equation:

$$\mathrm{i}\partial\!\!\!/\psi_\mathrm{L} - m\psi_\mathrm{R} = 0. \tag{2.32}$$

Now it is easy to identify the mass term: it is the term containing the right-handed spinor. Because of the maximum parity violation of the weak interaction, only left-handed neutrinos and right-handed anti-neutrinos exist (see section 2.2). So the spinors of the first lepton generation consist of $\psi_\mathrm{L} = \begin{pmatrix} \nu_\mathrm{e} \\ \mathrm{e}^- \end{pmatrix}_\mathrm{L}$ and $\psi_\mathrm{R} = \begin{pmatrix} 0 \\ \mathrm{e}^- \end{pmatrix}_\mathrm{R}$. Comparing eq. (2.30) and eq. (2.32) now shows that neutrinos have no mass in the SM, a property directly related to the non-existence of right handed neutrinos in the SM.

However, in the previous section it was shown that neutrinos are required to have a non-zero mass (see sec. 2.3.1). A simple way of adding a neutrino mass would be the introduction of a right-handed neutrino field ν_R, which does not take part in the weak interaction and would need an additional Yukawa coupling strength, accommodating for the smallness of the neutrino mass. This mechanism would give neutrinos mass in the same way the charged leptons get their mass and is therefore called the Dirac mass. But since neutrinos are uncharged particles, there exists another possibility: the Majorana mass. Majorana constructed a mass term by decomposing the Dirac Lagrangian into its chiral components, yielding two Dirac equations

$$\mathrm{i}\partial\!\!\!/\nu_\mathrm{L/R} - m\nu_\mathrm{R/L} = 0 \tag{2.33}$$

which are coupled by the mass. This is only possible if the neutrino is its own anti-particle, because then the right-handed field can be written as $\nu_\mathrm{R} = \mathrm{C}\bar{\nu}_\mathrm{L}^\mathrm{T}$, leading to $\nu = \nu_\mathrm{L} + \nu_\mathrm{L}^\mathrm{C}$ and automatically removing the independence of ν_L and ν_R. The Majorana mass in the Lagrangian would take the following form:

$$\mathcal{L}_\mathrm{L/R}^\mathrm{M} = -\frac{1}{2} m_\mathrm{L/R}\, \bar{\nu}_\mathrm{L/R}^\mathrm{C}\, \nu_\mathrm{L/R}. \tag{2.34}$$

Combining the Dirac mass term $\mathcal{L} = -m_\mathrm{D}\bar{\nu}\nu$ (with $\nu = \nu_\mathrm{L} + \nu_\mathrm{R}$) and the two Majorana mass terms eq. (2.34) results in $\mathcal{L}^\mathrm{D+M} = \mathcal{L} + \mathcal{L}_\mathrm{L}^\mathrm{M} + \mathcal{L}_\mathrm{R}^\mathrm{M}$. This would be a long expression, but it can be shortened by writing the left-handed fields in a matrix:

$$\mathcal{L}^\mathrm{D+M} = -\frac{1}{2} N_\mathrm{L}^\mathrm{T} M N_\mathrm{L} \qquad \text{with } N_\mathrm{L} = \begin{pmatrix} \nu_\mathrm{L} \\ \nu_\mathrm{R}^\mathrm{C} \end{pmatrix} \text{ and } M = \begin{pmatrix} m_\mathrm{L} & m_\mathrm{D} \\ m_\mathrm{D} & m_\mathrm{R} \end{pmatrix}. \tag{2.35}$$

To now find the masses of the fields ν_L and ν_R, the matrix M has to be diagonalized. Since the active neutrino mass is very small, and sterile neutrinos have not been observed yet, one needs to introduce a mechanism which leads to a small active neutrino mass and a small mixing angle between the left- and right-handed neutrinos. This is achieved by the so-called See-Saw mechanism, which assumes $m_\mathrm{L} = 0$ and $m_\mathrm{D} \ll m_\mathrm{R}$, leading to the following masses:

$$m_1 \approx \frac{m_\mathrm{D}^2}{m_\mathrm{R}} \text{ and } m_2 \approx m_\mathrm{R}. \tag{2.36}$$

This results in a small neutrino mass m_1, according to the smallness of the neutrino mass, and a small mixing angle $\tan 2\theta = 2m_\mathrm{D}/m_\mathrm{R}$, meaning that the light state ν_1 would mainly consist of the active ν_L and the heavy state ν_2 mainly of the sterile ν_R.

2.4. Determination of the neutrino mass

As stated before, oscillation experiments can not access the absolute scale of the neutrino mass. But there exist several different approaches to constrain this important parameter; some of them depend on the underlying theoretical model (sec. 2.4.1) to be sensitive to the neutrino mass, while the model-independent experiments only rely on the conservation of energy and momentum (sec. 2.4.2).

2.4.1. Model-dependent measurements

In principle there exist two ways of determining the neutrino mass: underlying a theoretical model like a cosmological model or the neutrino-less double beta decay and trying to confirm this theory experimentally – equal to a model-dependent measurement (sec. 2.4.1) – or relying on basic physical principles like energy and momentum conservation and therefore measure the neutrino mass model-independent (sec. 2.4.2).

Neutrino mass determination from cosmology

The limits on the neutrino mass from cosmology depend strongly on the cosmological model employed as a framework for the interpretation of astrophysical data. Most of the experiments dealing with cosmology are working with the Cosmic Microwave Background (CMB), the latest one is the Planck satellite. First results of the Planck collaboration [Ade14] are in good agreement with the standard spatially-flat six parameter ΛCDM cosmological model. Among other parameters, Ade et al. find a rather low value of the Hubble constant of $H_0 = (67.3 \pm 1.2)\,\mathrm{kms}^{-1}\mathrm{Mpc}^{-1}$ and a somewhat high value of the matter density of $\Omega_\mathrm{m} = 0.315 \pm 0.017$. For deriving limits on the neutrino properties, the Planck collaboration combines their data with the WMAP[2] and additional earth-based CMB data, data from baryon acoustic oscillation (BAO) surveys and uses the upper end of the multipole range. They find the number of neutrino-like relativistic particles to be consistent with the existing three neutrino families, namely $N_\mathrm{eff} = 3.30^{+0.54}_{-0.51}$ at 95 % C.L.
Massive neutrinos leave a fingerprint in the CMB spectrum via the Integrated Sachs Wolfe (ISW) effect: The transition of the neutrinos from a relativistic to a non-relativistic state affects the evolution of the gravitational potentials and therefore the structure formation. The characteristic parameter is the neutrino free-streaming length λ_FS

$$\lambda_\mathrm{FS} = \frac{8\,(1+z)}{\sqrt{\Omega_\Lambda + \Omega_\mathrm{m}\,(1+z)^3}} \frac{1\,\mathrm{eV}}{m_\nu} h^{-1}\,\mathrm{Mpc}, \tag{2.37}$$

which equals the scale on which neutrinos are non-relativistic and therefore wash out all density fluctuations on smaller scales. Regarding the small mass of neutrinos, massive neutrinos will reduce the growth of matter density perturbations and suppress the matter power spectrum on small scales. With this method, the Planck collaboration states a value of 0.23 eV (95 % C.L.) as upper limit for the sum of neutrino masses which represents a very strong constraint on the neutrino mass.
Despite the good agreement of the Planck parameter constraints with previous experiments (especially N_eff), it has to be noted that these constraints depend strongly

[2] **W**ilkinson **M**icrowave **A**nisotropy **P**robe

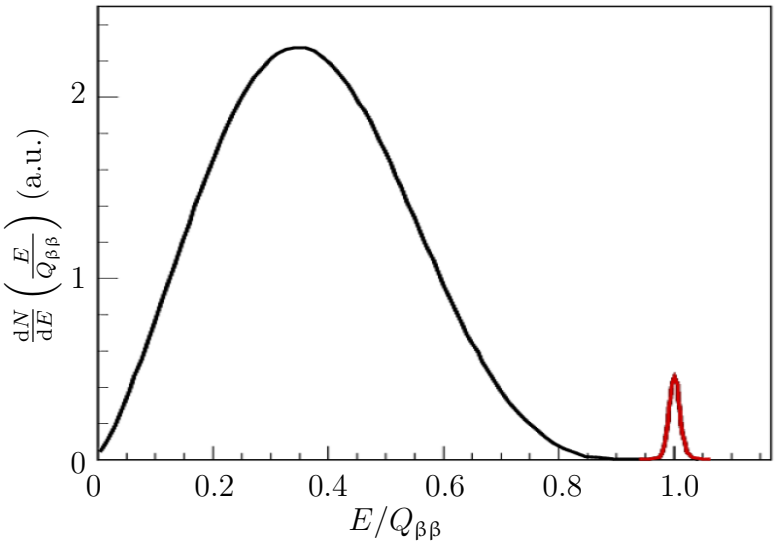

Figure 2.3.: **Double beta decay spectrum** - The ββ-decay spectrum is shown as continuum (black) while the 0νββ-decay spectrum is shown as red peak at the end of the spectrum. Figure adapted from [WS12].

on the used data set; the Planck collaboration itself lists several possible values for the sum of neutrino masses for different data sets, resulting in values between 0.23 eV and 1.31 eV. Another point is that all cosmological parameter constraints suffer strongly from uncertainties and rely very much on assumptions and priors for other parameters.
A model-independent measurement of the neutrino mass would reduce the number of free parameters and therefore also allow setting stronger constraints on other parameters.

Neutrino mass determination from neutrino-less double β-decay

The ββ-decay can be thought of as two single β-decays. To allow for a (double) β-decay, the final nucleus must have a larger binding energy than the original one. The binding energy, here described by the Bethe-Weizsäcker formula, simplifies to a parabola in the case of a fixed nucleon number A. For an even number of nucleons there exist two parabolas, one for nuclei with an even-even number of neutrons and protons and one with an odd-odd composition.
For some nuclei – for example ^{76}Ge – single β-decay is forbidden because the nucleus one atomic number higher (here: ^{76}As) has a smaller binding energy. However, the nucleus two atomic numbers higher (in this case ^{76}Se) has a larger binding energy, so ββ-decay is allowed. But it has to be noted that the ββ-decay is a weak process of second order and therefore it has a low probability to occur and a half life of the order 10^{20} yr or larger.

The 2νββ-decay in the SM has the following form:

$$ {}^{A}_{Z}N \rightarrow {}^{A}_{Z+2}N' + 2e^- + 2\bar{\nu}_e \qquad \text{and} \qquad {}^{A}_{Z}N \rightarrow {}^{A}_{Z-2}N' + 2e^+ + 2\nu_e \tag{2.38} $$

Eq. 2.38 results in a continuous energy spectrum for the electrons (positrons), because the anti-neutrinos (neutrinos) can also carry a part of the decay energy (Q-value) (see fig. 2.3). The process is fully included in the SM, because in this case

neutrinos are not required to have mass and the lepton number is conserved.
But one can also think of a $\beta\beta$-decay without the emission of neutrinos, the $0\nu\beta\beta$-decay. Since the postulation in 1939 [Fur39], this process caused many discussions. In contrast to the $2\nu\beta\beta$-decay, there are no neutrinos emitted in the $0\nu\beta\beta$-decay:

$$ {}^{A}_{Z}N \rightarrow {}^{A}_{Z+2}N' + 2e^- \qquad \text{and} \qquad {}^{A}_{Z}N \rightarrow {}^{A}_{Z-2}N' + 2e^+ \tag{2.39} $$

The energy of the electrons is no more a continuous spectrum (see fig. 2.3) but a sharp line at the Q-value, because there are no neutrinos emitted which might carry a part of the decay energy.
For $0\nu\beta\beta$-decay to be possible, neutrinos must be Majorana particles: the (virtual and massive) neutrino emitted and absorbed within the nucleus must be the same particle and the lepton number is violated by two units. Furthermore, maximum parity violation of the weak interaction requires the exchanged neutrinos to be massive: the weak interaction only couples to right handed antiparticles (positive helicity) and left handed particles (negative helicity). For massless particles chirality and helicity are the same, but in order to absorb a neutrino with a different helicity, the neutrinos must have mass to enable a Lorentz transformation resulting in a reversed helicity.
The observable in $0\nu\beta\beta$-decay experiments is the half life, but the effective Majorana neutrino mass can be determined by

$$ \langle m_{\beta\beta} \rangle^2 = \left| \sum_{i=1}^{3} U_{ei}^2 m_i \right|^2 = \frac{m_e^2}{G^{0\nu\beta\beta} \cdot \left| M^{0\nu\beta\beta} \right|^2 \cdot T_{1/2}^{0\nu\beta\beta}}. \tag{2.40} $$

Here $G^{0\nu\beta\beta}$ is the phase space factor, $M^{0\nu\beta\beta}$ is the combination of the Gamow-Teller and Fermi nuclear matrix elements and $T_{1/2}^{0\nu\beta\beta}$ is the half life of the corresponding $0\nu\beta\beta$-decay.
One of the latest results for the $0\nu\beta\beta$-decay half life comes from the Exo-200 experiment, working with ^{136}Xe [The14]: they find no statistically significant evidence for a $0\nu\beta\beta$-decay but set a half life limit of $1.1 \cdot 10^{25}$ yr at 90 % C.L. This value fits the results from GERDA (investigating the decay of ^{76}Ge) [Ago13], corresponding to a limit on the neutrino mass of $0.2 - 0.4$ eV.

Neutrino mass determination from time-of-flight measurements of Supernova neutrinos

Supernovae produce large amounts of neutrinos in the MeV range. The prime example is SN1987A: the light of this Type II supernova reached the detectors on Earth on 23rd of february 1987. It was a typical core collapse supernova, where the collapse happens due to self-gravitational forces of a star of several solar masses exceeding the radiation pressure and the degeneracy pressure of electrons. During the collapse, electrons and protons form neutrons and neutrinos

$$ p + e^- \rightarrow n + \nu_e \tag{2.41} $$

$$ e^+ + e^- \rightarrow \nu_\alpha + \bar{\nu}_\alpha \qquad (\alpha = e, \mu, \tau) \tag{2.42} $$

until the core collapse is stopped by neutron degeneracy, causing the implosion to bounce outward. The result of a supernova of Type II is either a neutron star or a

black hole, depending on the mass of the initial star. The emitted neutrinos carry away about 99% of the released energy during a neutrino burst which lasts several seconds. To estimate the mass of the emitted neutrinos, the time-of-flight method uses the temporal delay Δt between neutrino events observed at the corresponding detector:

$$\Delta t = t_2 - t_1 = \Delta t_0 + \frac{Lc^3 m^2}{2}\left(\frac{1}{E_2^2} - \frac{1}{E_1^2}\right). \tag{2.43}$$

Eq. (2.43) shows that neutrinos of the same type are needed to measure the absolute value of the neutrino mass. The traveled distance of the neutrinos L can be estimated; since neutrinos are barely deflected on their way through the universe, it is simply the distance from Earth to the supernova. The energies $E_{1,2}$ can be measured and particle discrimination methods ensure to only use neutrinos of the same type for the analysis. This leaves Δt_0 (time between emission of the two neutrinos from the supernova) as the largest uncertainty (apart from the large, but assessable energy uncertainties reported in [BBB$^+$87, HKK$^+$88]), because it depends strongly on the used model for the supernova collapse and the neutrino burst duration.
The neutrino burst of SN1987A lead to the detection of 8 neutrinos (time range of 6 s, energies of 20 – 40 MeV) in the IMB [BBB$^+$87] detector and 12 neutrinos (time range of 13 s, energies of 5 – 35 MeV) in Kamiokande-II [HKK$^+$88].
This was an outstanding moment for neutrino astronomy because it represented the first direct observation in neutrino astronomy. A detailed analysis performed by Loredo and Lamb in 2002 [LL02] yields an upper limit on the electron anti-neutrino mass of 5.7 eV at 95 % C.L.

2.4.2. Model-independent measurements

All model-independent approaches to measure the absolute value of the neutrino mass make use of the relativistic energy momentum relation $E^2 = p^2 + m_0^2$. Two examples are the decay of the π and τ, but both types of experiments give rather large upper bounds on the absolute neutrino mass scale. The challenge for this kind of measurement is to extract a very small value (neutrino mass) out of a difference of comparatively large values (mass and momentum of muon/pion), which is shown in the following.

Assuming a π-decay ($\pi^+ \to \mu + \nu_\mu$) at rest enables the determination of the muon neutrino mass as the missing energy, given that the momentum of the muon p_{μ^+} can be measured very accurately. p_{μ^+} is the only parameter to be determined because the rest mass of the pion and the rest mass of the muon are well-known. With this method, an upper limit for the muon neutrino mass was derived in 1996 [ABD$^+$96]:

$$m_{\nu_\mu} \leq 0.17\,\text{MeV} \qquad (90\,\%\ \text{C.L.}) \tag{2.44}$$

The analysis for the τ-decay can be performed similarly.

$$\tau^- \to 2\pi^- + \pi^+ + \nu_\tau \qquad \text{and} \qquad \tau^- \to 3\pi^- + 2\pi^+ \left(+\pi^0\right) + \nu_\tau \tag{2.45}$$

The τ decay in flight, so measuring all visible energy in the detector and knowing the original energy of the τ^- yields the mass of the tau neutrino as missing energy. The most stringent limit with this method is [B$^+$98]

$$m_{\nu_\tau} < 18.2\,\text{MeV} \qquad (95\,\%\ \text{C.L.}). \tag{2.46}$$

Because of this still comparably unconstraining upper limits, these kinds of experiments have little chance to reach the needed sub-eV sensitivity to determine the absolute value of the neutrino mass. A different approach is today much more promising, namely investigations of the single β-decay.

Neutrino mass determination from single β-decay solely relies on kinematics and therefore on relativistic energy momentum relation. In contrast to the neutrino mass determination from $0\nu\beta\beta$, no guess whether neutrinos are Majorana or Dirac particles has to be made. The principle is comparable to other model-independent neutrino mass measurement approaches, namely missing energy. In this case the neutrino mass is the missing kinetic energy of the β-decay electron from the decay

$$ {}^{A}_{Z}N \rightarrow {}^{A}_{Z+1}N' + \mathrm{e}^- + \bar{\nu}_\mathrm{e}. \tag{2.47} $$

The differential β-decay spectrum can be derived according to Fermi's Golden Rule

$$ \frac{\mathrm{d}N}{\mathrm{d}E} = \frac{G_F^2 \cos\theta_C \left|M\right|^2}{2\pi^3} \cdot F(Z+1,E) \cdot p \cdot (E+m_\mathrm{e}) \cdot (E_0 - E) \cdot \sqrt{(E_0-E)^2 - m_{\bar{\nu}_\mathrm{e}}^2} \cdot \Theta(E_0 - E - m_{\bar{\nu}_\mathrm{e}}) \tag{2.48} $$

with

- G_F: Fermi constant
- θ_C: Cabibbo angle
- M: transition matrix element
- $F(Z+1,E)$: Fermi function, accounting for Coulomb interaction between daughter nucleus and electron
- E: kinetic energy of the electron
- p: momentum of the electron
- m_e: mass of the electron
- $E_0 = Q - m_\mathrm{e}$: endpoint energy of the β-spectrum
- Q: decay energy.

If the neutrino has no mass, the maximum energy the electron can reach is the endpoint energy E_0, otherwise the endpoint energy E_0 minus the neutrino mass (see fig. 2.4), neglecting the recoil energy of the daughter nucleus and neglecting the final states distribution of the daughter molecule. Considering neutrino mixing as shown in sec. 2.3 and the fact that the squared neutrino mass differences are very small (see tab. 2.1), it is very likely to favor the quasi-degenerate neutrino mass model. In this case the only distortion of the spectrum that can be seen is equivalent to the case of a $\bar{\nu}_e$ with a definite mass and no mixing, so the squared neutrino mass can be written as an incoherent sum:

$$ m_{\bar{\nu}_\mathrm{e}}^2 = \sum_{i=1}^{3} \left|U_{\mathrm{e}i}\right|^2 \cdot m_i^2. \tag{2.49} $$

Since the event rate of the β-electrons close to the endpoint drops with E_0^{-3}, β-sources with low endpoints are required to achieve the necessary statistics.

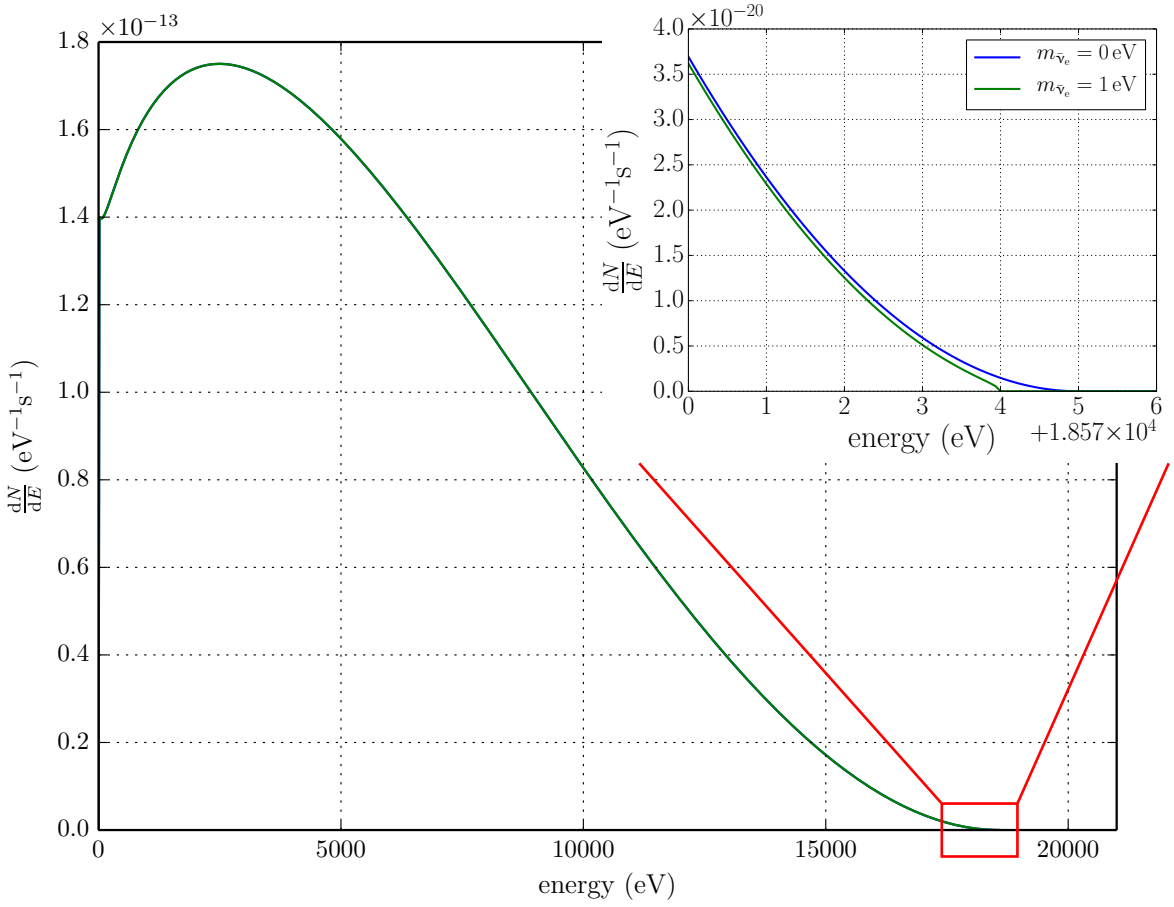

Figure 2.4.: **Example β-decay spectrum** - Shown is the differential β-decay spectrum of tritium with endpoint $E_0 = 18575\,\mathrm{eV}$ together with a zoom to the endpoint region. In this zoom, the signature of the nonzero neutrino mass is clarified: the green line stops at $E_0 - m_{\bar{\nu}_e}$ revealing the maximum kinetic energy of the β-decay electrons.

Rhenium as β-source

With its Q-value of 2.47 keV [SAB+04], ^{187}Re has the lowest endpoint of all known β^--emitters, which makes it a promising candidate for measuring the absolute neutrino mass from the kinematics of β-decay. On the downside, its half life of $T_{1/2} = 4.32 \cdot 10^{10}\,\mathrm{yr}$ is extremely long [SAB+04], requiring a large amount of ^{187}Re to reach an adequate source activity. The reason for the long half life is that the β-decay of ^{187}Re is – in contrast to tritium, the isotope with the second lowest endpoint – not a super-allowed transition, which dramatically reduces the transition probability and therewith the decay probability. To be able to handle the proper amount of rhenium, most of these experiments are designed as cryogenic bolometers, being source and detector at the same time. The released decay energy causes a small temperature rise which can be measured by sensitive thermometers. Currently the best limit on the neutrino mass is set by the Milano experiment [SAB+04] to

$$m_{\bar{\nu}_e} < 15\,\mathrm{eV} \qquad (90\,\%\ \mathrm{C.L.}). \tag{2.50}$$

The subsequent MARE[3] project aims to improve the sensitivity to the sub-eV range [GGP+06] which is necessary to set stronger constraints on the neutrino mass.

Tritium as β-source

The most stringent limits on the neutrino mass obtained by model-independent measurement come from investigations of tritium ^{3}H β-decay:

$$^3\mathrm{H} \rightarrow {}^3\mathrm{He}^+ + \mathrm{e}^- + \bar{\nu}_\mathrm{e}. \tag{2.51}$$

A big advantage of ^{3}H is its compensation of the second lowest decay energy by its super-allowed decay which enables an attractive half life, resulting in a relative rate of $2 \cdot 10^{-13}$ of all β-decays in the last 1 eV below the endpoint E_0. Some more of the advantages of ^{3}H as β-emitter are listed in the following:

- ^{3}H has the second lowest endpoint energy of $E_0 = 18.6\,\mathrm{keV}$
- the ^{3}H-decay is a super-allowed nuclear transition, so no corrections from nuclear transition matrix elements are needed
- the previous fact is also the reason for the quite short half life of $T_{1/2} = 12.3\,\mathrm{yr}$
- ^{3}H and ^{3}He$^+$ have both low Z values (nuclear charge):
  - results in simple electron shell configurations which enables a simple calculation of corrections due to interactions between β-electron and the source or atomic corrections for the decaying atom/molecule
  - results in small inelastic scattering probabilities of the outgoing β-electrons within the source

The combination of all these advantages strongly favors tritium as β-emitter for neutrino mass investigations. There is one drawback though: it is yet not possible to use atomic tritium but only molecular tritium:

$$^3\mathrm{H}_2 \rightarrow {}^3\mathrm{He}^3\mathrm{H}^+ + \mathrm{e}^- + \bar{\nu}_\mathrm{e}. \tag{2.52}$$

Therefore, the distribution of the final states has to be considered [KAT05], which contains not only the electronic excited states but also the molecular excitations. Nevertheless, previous tritium experiments in Troitsk and Mainz derived the yet best model-independent upper limits for the neutrino mass. A combined analysis of both experiments yields [Oli14]

$$m_{\bar{\nu}_e} < 2.0\,\mathrm{eV} \qquad (95\,\%\ \mathrm{C.L.}). \tag{2.53}$$

[3] MARE - **M**icrocalorimeter **A**rrays for a **R**henium **E**xperiment

CHAPTER 3

THE KARLSRUHE TRITIUM NEUTRINO EXPERIMENT

The KArlsruhe TRItium Neutrino (KATRIN) Experiment is dedicated to measuring the neutrino mass with an unprecedented sensitivity of 200 meV at 90 % C.L. (350 meV at 95 % C.L.). Compared to previous similar experiments at Mainz and Troitsk, this is a sensitivity gain of a factor of 10. Since the observable is the neutrino mass square, this requires an overall improve of a factor 100. To achieve this ambitious goal, KATRIN will perform high precision tritium β-decay spectroscopy close to the endpoint at 18.6 keV.
This chapter is devoted to the description of the setup of the KATRIN experiment. The description of the measurement principle of KATRIN (sec. 3.1) is followed by an overview of the components given in sec. 3.2 before closing with the monitoring and impact of tritium source parameters (sec. 3.3).

3.1. Neutrino Mass from tritium beta-decay

KATRIN investigates the tritium β-decay introduced in sec. 2.4.2:

$$^3\mathrm{H} \rightarrow\ ^3\mathrm{He}^+ + \mathrm{e}^- + \bar{\nu}_\mathrm{e}. \tag{3.1}$$

The differential spectrum of this decay can be derived using Fermi's Golden Rule:

$$\left(\frac{\mathrm{d}N}{\mathrm{d}E}(E)\right)_\beta = \frac{G_\mathrm{F}^2 \cos\theta_\mathrm{C} |M|^2}{2\pi^3} F(Z,E)\, p\,(E+m_\mathrm{e}) \sum_\mathrm{fs} P_\mathrm{fs}\, f_\mathrm{rad}(E-E_\mathrm{fs})\, \varepsilon_\mathrm{fs} \sqrt{\varepsilon_\mathrm{fs}^2 - m_{\bar{\nu}_\mathrm{e}}^2}\, \Theta(\varepsilon_\mathrm{fs} - m_{\bar{\nu}_\mathrm{e}}) \tag{3.2}$$

with the electron energy E, the endpoint energy E_0 and the final state energy E_fs resulting in a reduced endpoint energy $\varepsilon_\mathrm{fs} = E_0 - E_\mathrm{fs} - E$. The electron anti-neutrino mass is the incoherent sum of the mass eigenstates (see eq. (2.49)). KATRIN is using an electrostatic high-pass filter to analyze this spectrum. The (effective) neutrino mass is then extracted as a distortion to the spectrum in the endpoint region. In

fact, KATRIN is measuring an integral spectrum with the spectrometers acting as high-pass filters:

$$N_{\mathrm{S}}(qU) \propto \int_{qU}^{\infty} \frac{\mathrm{d}N}{\mathrm{d}E}(E)\, R(E, qU)\, \mathrm{d}E. \tag{3.3}$$

The response function $R(E, qU)$ will be discussed in more detail in the spectrometer section (sec. 3.2.3).

3.2. Components of the KATRIN experiment

An overview of the experimental setup of KATRIN is displayed in fig. 3.1. The 70 m long setup can be divided into four main sections: the source section (sec. 3.2.1), the transport section (sec. 3.2.2), the spectrometer section (sec. 3.2.3) and the detector section (sec. 3.2.4). The Rear Section as left end of the KATRIN experiment contains several essential source monitoring tools (sec. 3.2.5). To reach the aimed sensitivity on the neutrino mass of 200 meV, each component has to fulfill its requirements; a brief introduction to each component is given in the following.

3.2.1. Source section – WGTS

The source section of KATRIN contains the windowless gaseous tritium source (WGTS) being a high luminosity source for β-decay electrons.
Basically it consists of a tube of 10 m length and 90 mm diameter, kept at a constant temperature of 30 K by the surrounding cryostat. In the middle of the tube, molecular tritium with greater than 95 % isotopic purity is injected with a pressure of 10^{-3} mbar. This equals an injection rate of $5 \cdot 10^{9}$ tritium molecules per second. At the same time, tritium is pumped out by turbo-molecular pumps (TMPs) attached to the pump ports at each end of the WGTS tube, resulting in a decrease of the tritium density towards both ends. The pumped out tritium is processed in the "inner loop" system to guarantee a stable tritium flow and composition. With the KATRIN design parameters, a stable column density in the WGTS of $5 \cdot 10^{17}$ tritium molecules per cm^2 shall be achieved. This column density ρd corresponds to a number of tritium molecules of

$$n(\mathrm{T}_2) = \epsilon_{\mathrm{T}} \cdot \rho d \cdot A_{\mathrm{S}} = 2.53 \cdot 10^{19}, \tag{3.4}$$

with the tritium purity $\epsilon_{\mathrm{T}} = 95\,\%$ and the source area $A_{\mathrm{S}} = 53.33\,\mathrm{cm}^2$. As we will see in sec. 3.2.3, not all of these tritium molecules are by design visible to the detector. Only a fraction $\Omega/4\pi$ (solid angle) is visible to the detector, resulting in

$$n_{\mathrm{eff}}(\mathrm{T}_2) = \epsilon_{\mathrm{T}} \cdot \rho d \cdot A_{\mathrm{S}} \cdot \frac{\Omega}{4\pi}. \tag{3.5}$$

For the standard configuration of the magnetic fields, Ω is limited by the largest transmissible angle of $\theta_{\mathrm{max}} = 51°$ (see eq. (3.12)) to $\Omega = 2\pi \cdot (1 - \cos\theta_{\mathrm{max}})$. This results in an effective amount of tritium molecules in the source of $n_{\mathrm{eff}}(\mathrm{T}_2) = 4.66 \cdot 10^{18}$ or an effective tritium mass of $m_{\mathrm{eff}} = 46.6\,\mu\mathrm{g}$. The resulting isotropically emitted β-decay electrons are guided by an up to 3.6 T strong magnetic field to both ends of the WGTS tube. Note that possible scattering of the signal electrons has not been taken into account yet, this will be done via the response function (see eq. (3.15)).
In section sec. 3.3 follows a discussion about the parameters with the largest impact on the investigations of this thesis.

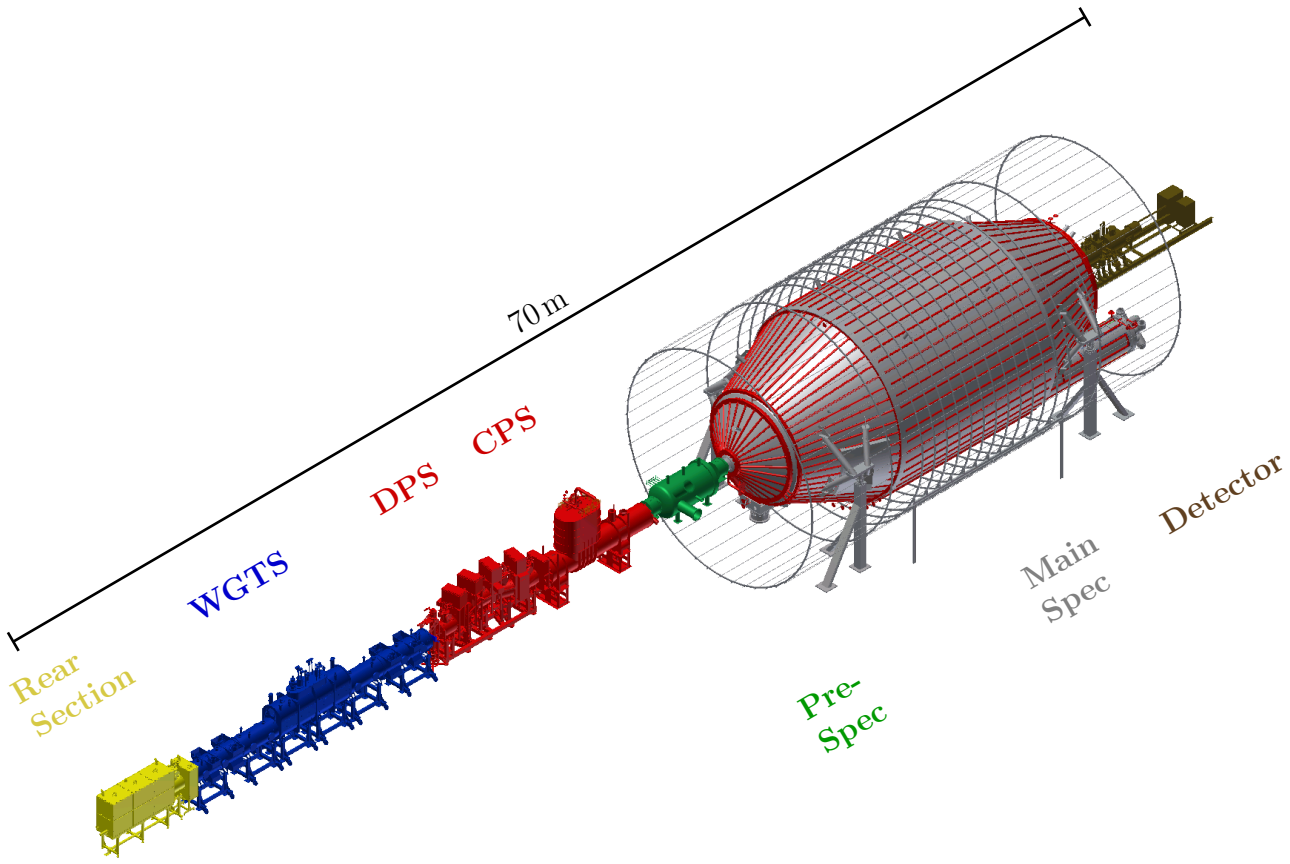

Figure 3.1.: **Overview of the KATRIN experiment** - consisting of

- Rear Section – monitoring of the source and calibration
- WGTS – windowless gaseous tritium source
- DPS – differential pumping section, tritium removal
- CPS – cryogenic pumping section, tritium removal
- Pre-Spec – pre-spectrometer, removal of low-energy β-decay electrons
- Main Spec – main spectrometer, high-resolution β-decay spectroscopy at the tritium endpoint region
- Detector – counting of transmitted electrons

3.2.2. Transport section – DPS and CPS

The task of the transport section is to reduce the tritium flow rate by 14 orders of magnitude to prevent tritium from migrating into the spectrometer section. This reduction is achieved by the differential pumping section (DPS) and the cryogenic pumping section (CPS).

Differential pumping section – DPS

The tritium reduction in the DPS is based on four TMPs with large pumping speed (overall more than $2000\,\mathrm{l\,s^{-1}}$) to reduce the tritium flow rate by a factor of 10^7.
The beam tubes between the TMPs are tilted against each other to prevent a direct line of sight from the source to the spectrometer section. Due to their electric charge, the β-decay electrons follow the magnetic flux tube through the DPS (provided by five superconducting magnets) while the neutral tritium molecules have a certain probability to straightly enter the pump ports. The tritium flow rate is reduced from 1 mbarl/s at the inlet to 10^{-7} mbarl/s at the exit of the DPS. Furthermore, the DPS also reduces the amount of positively charged ions, which would also follow the magnetic field lines towards the spectrometer section: a small electrostatic barrier keeps them in the DPS, where an electric dipole field helps removing the ions from the sensitive flux tube by virtue of the $\vec{E} \times \vec{B}$ drift.

Cryogenic pumping section – CPS

The tritium reduction in the CPS is in based on cryosorption. The inner wall of the CPS is cooled to 4.5 K by means of liquid helium. At such low temperatures, the probability for gas molecules to get adsorbed on the walls is greatly enhanced. To adsorb tritium, the inner wall of the CPS is cooled down by liquid helium to 4.5 K, resulting in a high probability for gas molecules to stick to the wall. This effect is increased further by freezing argon onto the wall surface. The argon snow needs to be regenerated every few weeks between KATRIN runs to ensure that the cryogenic pump maintains the required pumping efficiency.
The CPS reduces the tritium flow by another seven orders of magnitude to roughly 10^{-14} mbarl/s at the entrance of the spectrometer section.

3.2.3. Spectrometer section – pre- and main spectrometer

The transport section is followed by the section for high precision β-decay spectroscopy, which consists of a tandem system formed by the pre- and main spectrometer.

Pre-spectrometer

The task of the pre-spectrometer is to filter all low-energy electrons in order to enable high-precision β-spectroscopy around the endpoint with the main spectrometer. Therefore, a potential barrier up to 18.3 keV can be applied to the spectrometer. Applying this potential barrier reduces the β-decay electron flux by up to seven orders of magnitude and therefore minimizes background caused by residual gas ionization. Both spectrometers work with the MAC-E filter principle [LS85, PBB+92] (magnetic adiabatic collimation with superimposed electrostatic retarding potential), which is in the following explained in detail at the example of the main spectrometer.

Main spectrometer

The task of the main spectrometer is to perform the high precision energy analysis of the β-decay electrons created in the WGTS.
The combination of electrostatic retardation and magnetic collimation (parallelization of momenta) characteristic of the MAC-E filter (see fig. 3.2) allows to achieve the required superior energy resolution, as will be outlined in the following.

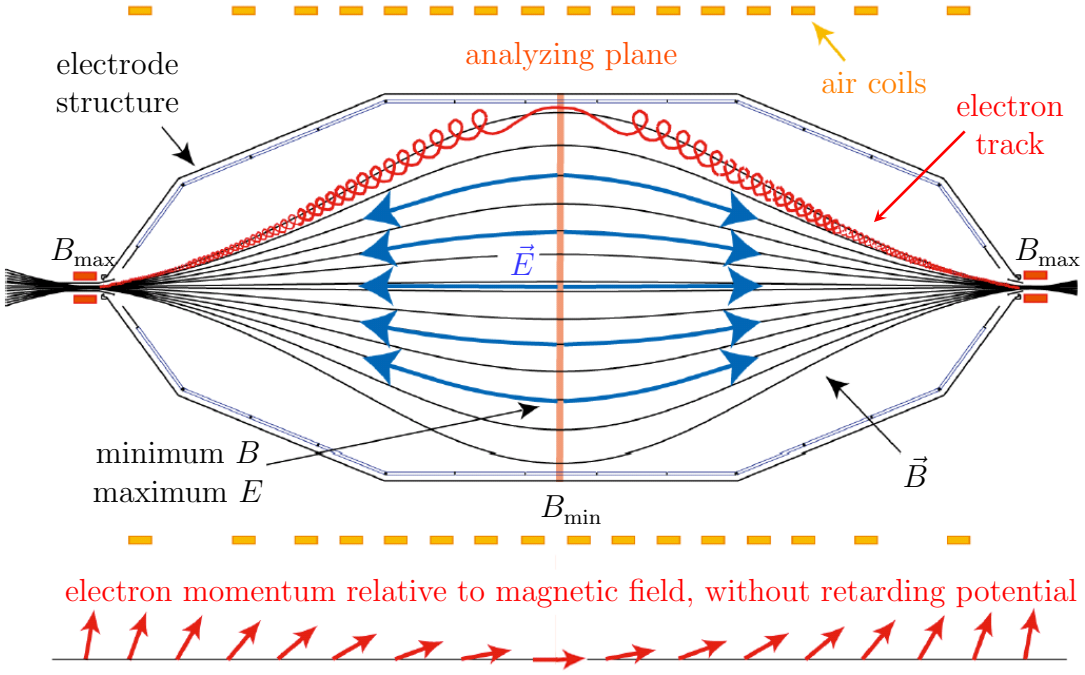

Figure 3.2.: **MAC-E filter principle** - The momentum vectors of the electrons following cyclotron paths become adiabatically aligned along the magnetic field lines. This enables precise energy filtering with the retarding potential. Figure adapted from [Hug08].

Magnetic adiabatic collimation

The β-decay electrons gyrate around the magnetic field lines at every point of their path through the KATRIN experiment due to the Lorentz force. Their kinetic energy can be split up into a longitudinal and a transversal component relative to the magnetic field:

$$E_{\text{kin}} = E_{\parallel} + E_{\perp}. \tag{3.6}$$

To preserve the properties of the electrons, such as the polar angle with respect to magnetic field, the electron transport has to be fully adiabatic. For 18.6 keV energy electrons at the endpoint of the tritium spectrum this leads to the following requirements on characteristics of the main spectrometer:

- **Adiabatic guiding of the electrons:** the electron motion is adiabatic if the cyclotron step length is larger than the magnetic field gradient $\Delta B/B$. If this holds, the product of relativistic Lorentz factor and magnetic moment is constant [Jac62]: $\gamma\mu = \text{const}$. In the non-relativistic treatment (electrons from tritium β-decay up to $\gamma = 1.04$), this leads to:

$$\mu = \frac{E_{\perp}}{B} = \text{const}. \tag{3.7}$$

  Since only the longitudinal part $E_{\parallel}$ of the kinetic energy can be analyzed, the transversal part $E_{\perp}$ needs to be reduced to a minimum. This is done by reducing the magnetic field towards the center of the main spectrometer.

According to eq. (3.7), the transversal energy thereby is reduced by the same suppression ratio to satisfy the conservation of μ. The magnetic field is smallest in the analyzing plane in the center of the main spectrometer, enabling the energy analysis by applying an electrostatic potential. However, the transversal energy can never reach zero since the magnetic field needs to be larger than zero to guide the electrons towards the detector.

- **Magnetic flux conservation**: Due to the conservation of magnetic flux:

$$\Phi = \int_A \vec{B}\,\mathrm{d}\vec{A} = \text{const.}, \tag{3.8}$$

the decrease of the magnetic field in the spectrometer implies an increase of the flux tube area A. Together with the requirement to image the source diameter A_S onto the detector, this leads to the large central diameter of the main spectrometer of 9.8 m.

- **Energy resolution:** the energy resolution ΔE of the KATRIN experiment is limited by the ratio of minimum B_min to maximum B_max magnetic field:

$$\frac{\Delta E}{E} = \frac{B_\mathrm{min}}{B_\mathrm{max}}. \tag{3.9}$$

For electrons with energies around the endpoint, $E \approx 18.6\,\mathrm{keV}$, this results in an energy resolution of $\Delta E \approx 0.93\,\mathrm{eV}$:

$$\Delta E \approx \frac{0.3\,\mathrm{mT}}{6\,\mathrm{T}}\,18.6\,\mathrm{keV} = \frac{1}{20000}\,18.6\,\mathrm{keV} = 0.93\,\mathrm{eV}. \tag{3.10}$$

- **Magnetic mirror:** if electrons are guided adiabatically, there is a fixed relation between polar angle and magnetic field. For two arbitrary points on the electron path with different magnetic field strength, the dependency is given as follows:

$$\frac{\sin^2\theta_1}{\sin^2\theta_2} = \frac{B_1}{B_2}. \tag{3.11}$$

The maximum magnetic field at the KATRIN experiment is achieved at the downstream ends of the main spectrometer (see fig. 3.2) with 6 T. If the polar angle of the electrons is larger than 90° at this point, they will be reflected due to the magnetic mirror effect. This means a maximum transmissible pitch angle of 51° for electrons starting in the WGTS (at 3.6 T), calculated with eq. (3.11):

$$\theta_{\mathrm{max,\ WGTS}} = \arcsin\sqrt{\frac{3.6\,\mathrm{T}}{6\,\mathrm{T}}} \approx 51°. \tag{3.12}$$

Electrostatic filtering

After the adiabatic collimation, the electron energy is analyzed by the application of a (negative) retarding potential in the analyzing plane (compare fig. 3.2). Only electrons with longitudinal energy larger than the applied retarding potential can pass the analyzing plane and reach the detector. Since the retarding potential just provides a lower limit for the energy of the electrons, the MAC-E filter acts as a high pass filter. This results in the measurement of an integral β-decay spectrum as given in eq. (3.3).

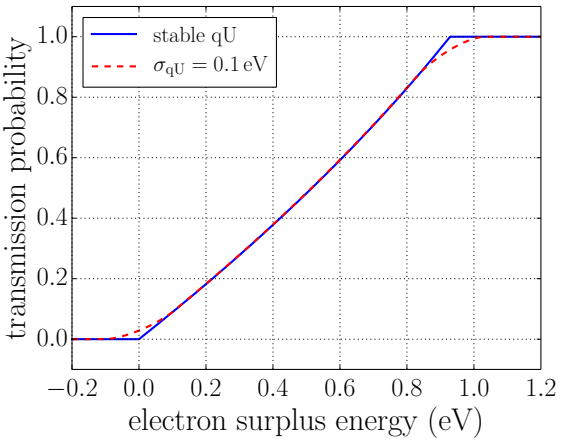

Figure 3.3.: **Transmission function** - Shown is the analytical transmission function for stable high voltage (blue, solid) and for sinusoidal high voltage fluctuations (red, dashed). The retarding potential is set to −18572 V.

Transmission function

Combining the abovementioned effects of magnetic adiabatic collimation and electrostatic filtering leads to the transmission probability for electrons passing the main spectrometer of the KATRIN experiment. This specific property of the MAC-E filter can be analytically described by the transmission function $T(E, qU)$:

$$T(E,qU) = \begin{cases} 0 & \text{for } E < qU \\ \dfrac{1-\sqrt{1-\frac{E-qU}{E}\frac{B_S}{B_{min}}}}{1-\sqrt{1-\frac{B_S}{B_{max}}}} & \text{for } qU \leq E \leq qU + \Delta E \\ 1 & \text{for } E > qU + \Delta E \end{cases} \tag{3.13}$$

with B_S being the magnetic field at the WGTS. The transmission function of electrons for a retarding potential of $U = -18572\,\text{eV}$, $B_S = 3.6\,\text{T}$, $B_{min} = 0.3\,\text{mT}$ and $B_{max} = 6\,\text{T}$ is visualized in fig. 3.3. In addition to the sharp, analytical transmission function, also the smearing caused by sinusoidal high voltage fluctuations of the order 0.1 V is shown. Sinusoidal high voltage fluctuations with amplitude A can be expressed as follows:

$$T_{sine}(E,qU) = \frac{1}{\pi}\int_{-\pi}^{+\pi} T(E, qU + A\sin t)\mathrm{d}t. \tag{3.14}$$

This kind of fluctuations is investigated for its effect on possible relic neutrino overdensities in sec. 5.4.3.
Scattering of the electrons, for example in the WGTS, further lowers the electron rate at the detector. Therefore, another function is defined, describing the probability of an electron emitted in the WGTS to reach the detector: the response function $R(E, qU)$.

Response function

The response function accounts for energy loss of the signal electrons due to scattering or synchrotron radiation. Most important are the inelastic scattering effects, since the inelastic cross-section for scattering of 18.6 keV electrons on tritium

molecules is 12 times larger than the elastic cross-section [KAT05]. Synchrotron energy losses are most relevant for electrons emitted at the rear end of the WGTS with the maximum transmissible polar angle of 51° [Gro15].
$f(\varepsilon)$ describes the probability for an electron do loose a specific amount ε of energy during scattering. The so called "response function" $R(E, qU)$ combines the transmission function $T(E, qU)$ with the energy loss function $f(\varepsilon)$:

$$R(E, qU) = \int_0^E T(E - \varepsilon, qU) \cdot (P_0\,\delta(\varepsilon) + P_1\,f(\varepsilon) + P_2\,(f \otimes f) + \dots)\,\mathrm{d}\varepsilon. \quad (3.15)$$

In this representation, the probability P_i accounts for the number of scattering processes i; the energy loss function f has to be convolved with itself $(i-1)$-times to implement multiple scattering.

3.2.4. Detector section

After successfully passing the spectrometer section, the signal electrons are counted by a 9 cm diameter monolithic silicon detector. The detector is divided into 148 pixels, enabling a minimum spatial resolution to account for eventual field inhomogeneities.
Despite its large energy resolution of about 1.5 keV in the tritium endpoint energy range, the detector system can discriminate background by post accelerating the signal electrons coming from the main spectrometer. This shifts the signal electrons into regions of lower background. Additionally, the system is actively and passively shielded against cosmic background and gamma radiation.

3.2.5. Rear Section

The Rear Section is the rear end to enclose the KATRIN experiment in terms of flux tube and vacuum. The main task of the Rear Section is controlling the electric potential of the source gas set by the Rear Wall and monitoring the WGTS parameters like column density of the source gas with an angular selective electron gun (E-gun). The electron beam provided by this E-gun can be steered across the whole flux tube by magnetic dipole coils providing azimuthal and radial coverage.
Since this KATRIN component, especially its electromagnetic design, is a central topic of this thesis, its requirements and properties will be discussed in more detail chapter 4.

3.3. Monitoring and impact of tritium source parameters

One of the central components of the KATRIN experiment is the ultra-luminous tritium source. It will handle an unprecedented amount of tritium resulting in the enormous rate of β-decays of about 10^{11} cps. This large quantity of tritium provides a factor 10 better sensitivity compared to previous neutrino mass experiments.
Furthermore, the unique tritium source opens the door to search for yet undetected particles like the relic neutrinos. Those relic neutrinos originate 1 s after the Big Bang and today form the cosmic neutrino background (CνB), the neutrino equivalent to

the cosmic microwave background (CMB). The non-zero mass of the neutrinos may enable clustering of relic neutrinos, resulting in a local relic neutrino overdensity. A possibility to measure those relic neutrinos is the induced β-decay. As we will see in sec. 5.1.3, the cross-section for the relic neutrino capture is even smaller than current limits on dark matter interaction cross sections. Therefore, the target mass needs to be maximized. The high-luminosity tritium source puts KATRIN in the unique position to constrain the CνB by relic neutrino capture.
The capture rate is of course dependent on the tritium amount, the number of tritium molecules $n(T_2)$ present in the source, which can be expressed as:

$$n(T_2) = \epsilon_T \cdot \rho d \cdot A_S. \tag{3.16}$$

Here, ϵ_T is the tritium purity of T_2, ρd the tritium column density and A_S the source cross-section area. The tritium purity will be very precisely monitored by LAser induced RAman spectroscopy (LARA) [Fis14]. The source cross-section area A_S remains always fixed by design. This leaves the column density left as most critical parameter for monitoring $n(T_2)$. Changes in ρd can be measured by the Rear Section electron gun (E-gun), which provides a beam of electrons with well-defined properties to check the scattering probabilities in the WGTS. This E-gun beam is used to scan the whole flux tube of the WGTS and the detector counts the respective electrons. This method requires precise control of the E-gun beam parameters, more specifically demanding for minimum spread of polar angle and energy. Minimizing those spreads requires detailed electromagnetic design (EMD) simulations of the Rear Section. Therefore, the Rear Section is implemented into the most recent version of the KATRIN particle tracking simulation software Kassiopeia.
In the following chapter 4 the most important simulations and optimizations for the Rearsection E-gun are described. Hereafter in chapter 5 the relic neutrino discovery potential with regard to the tritium source properties are investigated.

CHAPTER 4

ELECTROMAGNETIC DESIGN FOR THE REAR SECTION OF THE KATRIN EXPERIMENT

The Rear Section is an important part of the calibration and monitoring systems (CMS) of KATRIN. One of the tasks of the Rear Section is to provide a beam of electrons with properties emulating the tritium β-decay electrons. These properties (e.g. electron energy) need to be precisely controllable to enable different calibration procedures for the rest of the KATRIN experiment. Therefore, one goal of this thesis was to implement the Rear Section in the most recent version of the KATRIN simulation package Kassiopeia [Fur15, Gro15, FG$^+$15]. By this, full 3D simulations of the Rear Section and verification of previous simplified simulations are possible. This chapter begins with a summary of the design requirements for the Rear Section. To pass these demands, a sophisticated electromagnetic design (EMD) has been developed [Bab14] which is currently constructed and tested at the UCSB[1]. Metrologically the Rear Section EMD contains two essential parts: the "electron gun (E-Gun)" for generation and acceleration of the electrons and a transport section for guiding and optimizing the E-gun beam. In the following, the different electromagnetic components are first described, then the implementation into Kassiopeia is shown and finally this chapter concludes with simulations showing that the Rear Section will meet its requirements in terms of E-gun beam characteristics.

4.1. Requirements for the electromagnetic design of the Rear Section

As stated in the introduction of this chapter, the Rear Section is a calibration and monitoring system for KATRIN fulfilling its requirements featuring a versatile photoelectron source. The requirements are written down in detail in the "KATRIN Rear Section Conceptual Design Document" [B$^+$13]. Hence in this section just a short summary of the requirements regarding the EMD of the Rear Section is given. One of the main tasks of the Rear Section is to measure the tritium column density in the WGTS with the E-gun beam within a relative precision of better than 0.1 %.

[1] University of California, Santa Barbara

Table 4.1.: **Requirements for the Rear Section of the KATRIN experiment** - Visualized are the requirements for the three important E-gun electron beam characteristics: the polar angle of the momentum of the electrons with respect to the z-axis (θ), the kinetic energy of the electrons and the electron rate of the E-gun. Those requirements for the Rear Section and its versatile photo-electron source demand detailed EMD simulations.

beam characteristic	requirement
pitch angle range	up to largest transmissible pitch angle:
	51° in WGTS or 90° at the pinch magnet
pitch angle spread	$\leq 4°$ at largest transmissible pitch angle in the WGTS
energy range	up to 25 keV
energy spread	≤ 0.2 eV
rate stability	$\Delta R/R < 10^{-3}$ over 3 min at rates $\leq 10^5\,\mathrm{s}^{-1}$

Such a precise determination of the column density is important because it affects the electron scattering within the WGTS, manipulating the shape of the tritium spectrum. The column density can be monitored by measuring the energy loss of the E-gun beam electrons.
Therefore, the Rear Section E-gun must produce electrons with a sufficiently well defined energy, angular and intensity distribution to enable column density measurements with less than 0.1 % uncertainty.

Three other important systematic investigations are the Main Spectrometers work function, transmission function and response function. The KATRIN specifications require the uncertainties on the transmission and response function to be smaller than 1 % and 0.1 % respectively. The transmission function measurement with the Rear Section E-gun beam uses an optimized narrow energy distribution in order to not induce more than 1 % uncertainty on the transmission function.

All official requirements are summarized and visualized in tab. 4.1, which clarifies the importance of detailed simulations of the E-gun and therefore the EMD of the Rear Section of the KATRIN experiment.

4.2. Electromagnetic components

The Rear Section can be used as a reference for KATRIN electromagnetic design simulations, because it features all types of electromagnetic components represented in KATRIN: on the magnet side, there are typical solenoids which are providing the magnetic guiding field for the electrons but also a superconducting magnet and even magnetic steering coils, forming a magnetic dipole. On the electrode side, the Rear Section uses acceleration electrodes to give the electrons the needed kinetic energy and electric dipoles to remove trapped electrons.
In the following sections, the electromagnetic working principle of these different parts of the Rear Section is described, divided into magnets and electrodes.

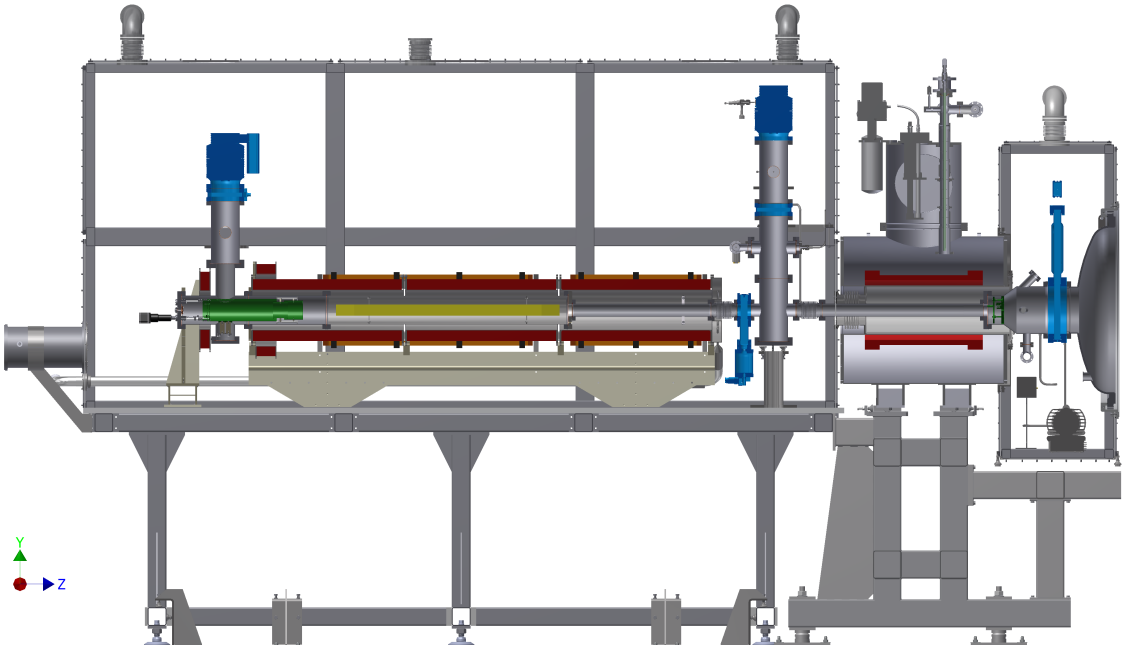

Figure 4.1.: **CAD half cut of the Rear Section** - This side view gives an overview of the position and orientation of the different components described in sec. 4.2. The magnets responsible for the magnetic guiding field are highlighted in red whereas the magnetic dipole coils are shown in orange. E-gun and the post acceleration electrodes are displayed in green in contrast to the electric dipole electrodes in yellow. The blue marked components are relevant for the vacuum system with parts like pumps or flanges. Figure adapted from [Bab14]

4.2.1. Magnets

Basically, there exist two types of magnets in the Rear Section: on the one hand "solenoids" responsible for the magnetic guiding field for the electron beam, and on the other hand magnetic dipoles enabling the steering of the electron beam.

Guiding magnets

The guiding magnets of the Rear Section (see fig. 4.3) are responsible for the z-axis[2] symmetric magnetic guiding field (see fig. 4.4). The axisymmetric field is called guiding field because it forces the electrons (in general all moving, charged particles) onto a cyclotron motion due to the Lorentz-force

$$\vec{F}_L = q\left(\vec{E} + \vec{v} \times \vec{B}\right). \tag{4.1}$$

The magnetic guiding field of the Rear Section must not only guide the electrons of the E-gun forwards to the next part of KATRIN, but also guides the electrons of the tritium decays in the WGTS backwards onto the Rear Wall. For the last purpose, the normally conducting coils with field strengths of the order 50 mT are not sufficient because they could not compress the flux tube of the WGTS in a way that it fits into the Rear Section. Therefore a superconducting re-condenser magnet

[2]The z-axis at the Rear Section is aligned to the one of the KATRIN global coordinate system (pointing from the Rear Section to the detector).

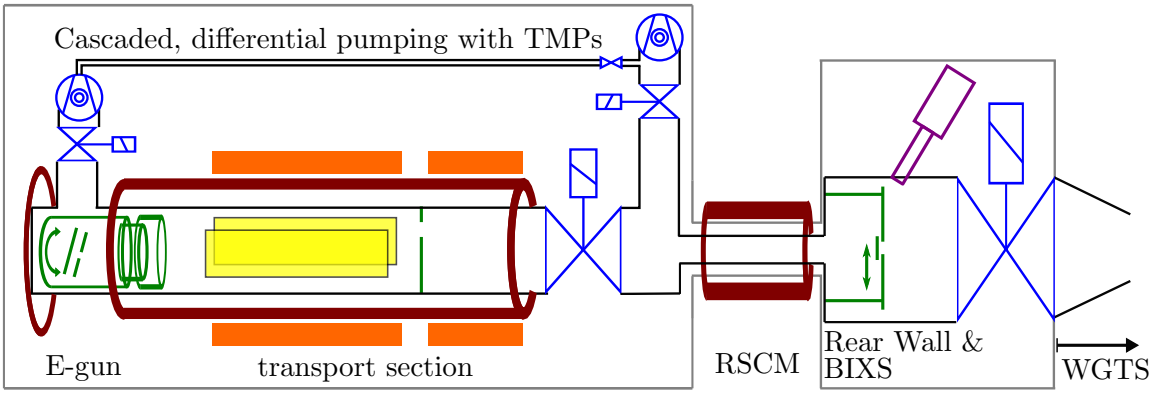

Figure 4.2.: **Half cut schema of the Rear Section** - Like in the CAD fig. 4.1, the magnets responsible for the magnetic guiding field are highlighted in brown whereas the magnetic dipole coils are shown in orange. E-gun and the post acceleration electrodes are displayed in green in contrast to the electric dipole electrodes in yellow. For completeness also the differential pumping at the Rear Section with two turbo-molecular pumps (TMPs) is illustrated as well as further physics and sensor instrumentation. These non-EMD components are not treated in this thesis but rather in [Bab14]. Figure adapted from [Bab14].

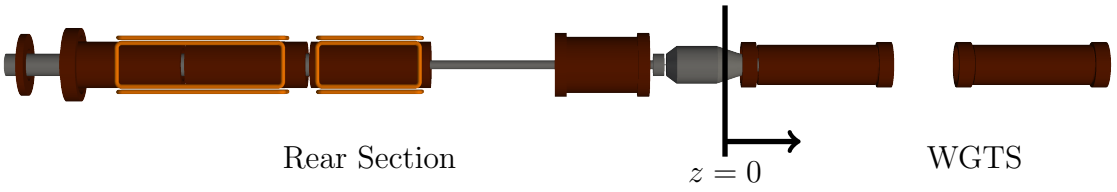

Figure 4.3.: **Rear Section geometry in** KASSIOPEIA - This picture shows the implementation of the Rear Section in KASSIOPEIA. Magnets responsible for the magnetic guiding field of the Rear Section are displayed in brown, the magnetic dipole coils in orange and the beam tube in gray. Additional to the Rear Section magnets on the left, also the first two superconducting magnets of the WGTS are displayed on the right.

(RSCM) is added at the WGTS side of the Rear Section (field strength 4.7 T). Only one superconducting magnet is needed, because the normally conducting magnets just have to guide the electrons of the E-gun into the WGTS and not the other way round.
More important than the superconducting field is the normal conducting field of the three identical solenoids since in this region the E-gun beam characteristics are defined. The field strength of the solenoids is increased and homogenized by two booster coils (see fig. 4.4): one slightly behind the E-gun (called E-gun booster coil) to enable the electron creation in a homogeneous field, and the other one on top of the last solenoid (from left to right, see fig. 4.3) for an adiabatic acceleration of the electrons.

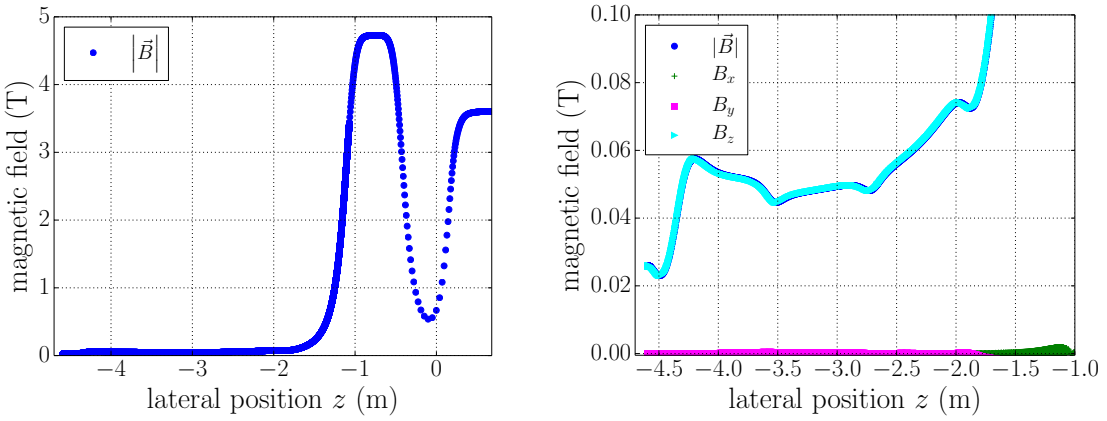

(a) **Absolute magnetic field of the Rear Section**

(b) **Magnetic field components of the Rear Section**

Figure 4.4.: **Magnetic field of the Rear Section** - The large fields of the superconducting RSCM and first DPS magnet dominate the magnetic field (left). A zoom enables the visualization of the magnetic field components (right); the gaps between the normally conducting solenoids are represented by a slight drop in the magnetic guiding field. Although the top and bottom magnetic dipoles are activated, their field is of the order mT, making it hardly visible on this scale.

Magnetic dipole coils

A widely used tool to generally steer beams of charged particles is a magnetic dipole coil. In this case the magnetic dipoles are used to shift the E-gun beam slightly off-axis to prevent a direct line of sight from the E-gun back plate to the WGTS. This direct line of sight would enable uncharged tritium molecules to travel backwards from the WGTS towards the E-gun. However, the amount of tritium close to the E-gun should be minimized to avoid damage of the sensitive E-gun back plate by radiochemical effects or ion-sputtering [Bab14]. This risk of damage is reduced by the implementation of an additional barrier: a diaphragm between the E-gun and the Rear Wall with an aperture offset of 10 mm (see fig. 4.6) blocks the direct line of sight from WGTS to E-gun back plate.

The task of the magnetic dipole coils is now to ensure a shift in y-direction in a way that the E-gun beam fits through the aperture. This is achieved by the superposition of the solenoid guiding field and the perpendicular magnetic field of the dipole coils:

$$\Delta y = \frac{B_y}{B_z} \cdot l_z \tag{4.2}$$

Eq. (4.2) for the shift of a field line in y-direction is estimated for an overlap of the perpendicular fields in z-direction of l_z. Not included are eventual stray fields or inhomogeneities, therefore the simulation of the magnetic dipoles was an important task. It has to be noted that this kind of shift affects the magnetic field lines itself and therefore charged particles coming from either direction continue their movement along the field line.

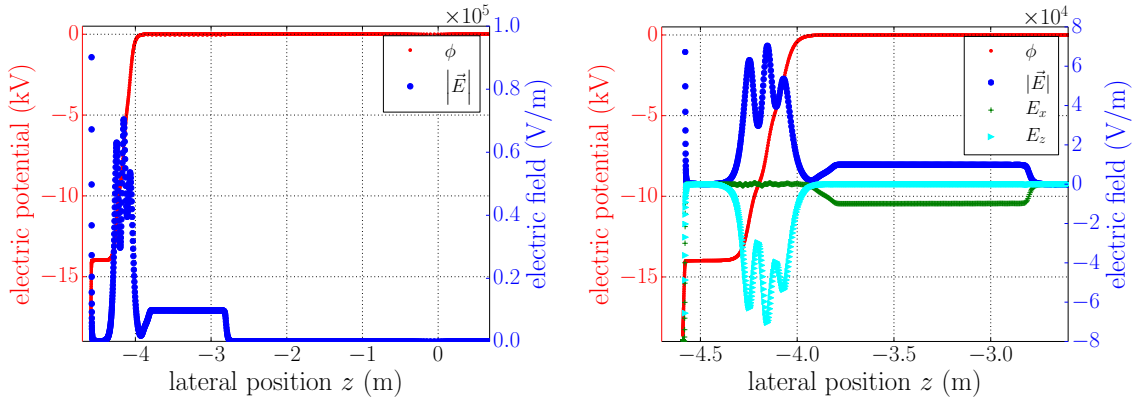

(a) **Electric potential ϕ and absolute electric field of the Rear Section**

(b) **Electric potential ϕ and electric field components of the Rear Section**

Figure 4.5.: **Electric potential and electric field of the Rear Section** - The post acceleration electrodes create a smooth potential and E_z to enable the adiabatic acceleration of the electrons, in contrast to the E-gun where the electric field dominates the motion (left). On the right, the zoom reveals the components of the electric field, enabling the identification of the dipole field (green) and the post acceleration field (cyan).

4.2.2. Electrodes

The electrostatic configuration of the Rear Section consists of the beam tube on ground potential, the acceleration electrodes for defining the kinetic energy of the E-gun electrons and the electric dipoles to remove trapped electrons. The electric potentials and fields by the electrodes are shown in fig. 4.5, and the function of the individual components is described in the following paragraphs.

Electron gun

The working principle of the electron gun (E-gun) used at the Rear Section is based on the production of free electrons by the photoelectric effect and subsequent electrostatic acceleration of the electrons. The photoelectric effect is the explanation for the photon induced electron emission of a metallic surface [Ein05]: if the energy of the exciting photon is larger than the difference between electron binding energy and vacuum level, the photoelectric emission of an electron close to the surface is possible. This difference is called "work function" W_F, defining the minimum photon energy to emit an electron:

$$E_{\text{kin}} = h \cdot f - W_F, \tag{4.3}$$

with Planck's constant h and the frequency f. At the Rear Section, the photoelectric electron emission is implemented by optical fibers glued into the E-gun back plate, which is for this reason in the fiber region gold coated (see fig. 4.13b). The E-gun back plate (cathode) is a thin round plate, forming a rotatable parallel-plate capacitor together with the identically constructed front plate (anode) – compare fig. 4.7. By applying a voltage difference to the two plates, the electrons emitted of the back plate surface are immediately accelerated in direction to the front plate. In a previous

section (sec. 3.2.3), adiabatic guiding of the electrons is defined as conserving the magnetic moment

$$\mu = \frac{E_\perp}{B}. \tag{4.4}$$

Sticking to this convention, the electron acceleration between the E-gun plates is absolutely non-adiabatic because the electric field dominates the motion and causes large changes of the magnetic moment. Such a non-adiabatic acceleration makes it very difficult to reach small angular and energy distribution widths, which is the main reason for the usage of the post acceleration electrodes to accelerate the electrons to the tritium endpoint energy of 18.6 keV.

Post acceleration electrodes

As mentioned in the previous paragraph, the acceleration between the plates of the E-gun is non-adiabatic. To ensure that the E-gun meets the design values for the angular and energy spread listed in tab. 4.1 and to further increase the flexibility to control the electron beam, two more acceleration stages are used. These stages are implemented as cylinders aligned along the z-axis (see fig. 4.7) with equidistant potentials (see fig. 4.5) keeping the adiabaticity violation as small as possible during the post acceleration process [Bab14]. Another advantage of using post acceleration electrodes is the minimization of the risk of an electric breakdown at the E-gun due to large potential differences of the order 20 keV to plates with a distance of 1 cm.

Electric dipole electrodes

Up to now, we have magnetic dipoles steering the electron beam to prevent a direct line of sight from the WGTS to the E-gun back plate. However, charged particles from the WGTS (like tritium ions) can still reach the gold surface of the E-gun back plate, since they follow the magnetic field lines.
Furthermore, electrons from the E-gun can be reflected on their way to the detector, for example due to scattering on gas molecules or magnetic reflection. Either way, those electrons may return on the same field line and be again reflected by the electrostatic potential of the post acceleration and E-gun. The problem with the reflection in general is that it is non-adiabatic and therefore changes the electron angle θ. As a result the angular distribution might become broader.
To prevent both of these effects (ion sputtering on the gold surface of the E-gun back plate and reflection of electrons), the Rear Section uses dipole electrodes which cause an electric field transverse to the magnetic guiding field. They are implemented as a long parallel-plate capacitor with additional, kinked plates at each end (see fig. 4.7). This constellation results in the $\vec{E} \times \vec{B}$ drift with a drift speed of

$$v_D = \frac{\vec{E} \times \vec{B}}{B^2}. \tag{4.5}$$

Similar to the magnetic dipoles, the dipole electrodes are designed in a way to maximize their effect, so they cover a z-axis range of about 1 m. This is enough to safely remove ions coming from the WGTS, because their kinetic energy is of the order 10 meV, which will drift them towards the vacuum vessel wall [Bab14].
The electrons will undergo the $\vec{E} \times \vec{B}$ drift every time they pass the electric dipole,

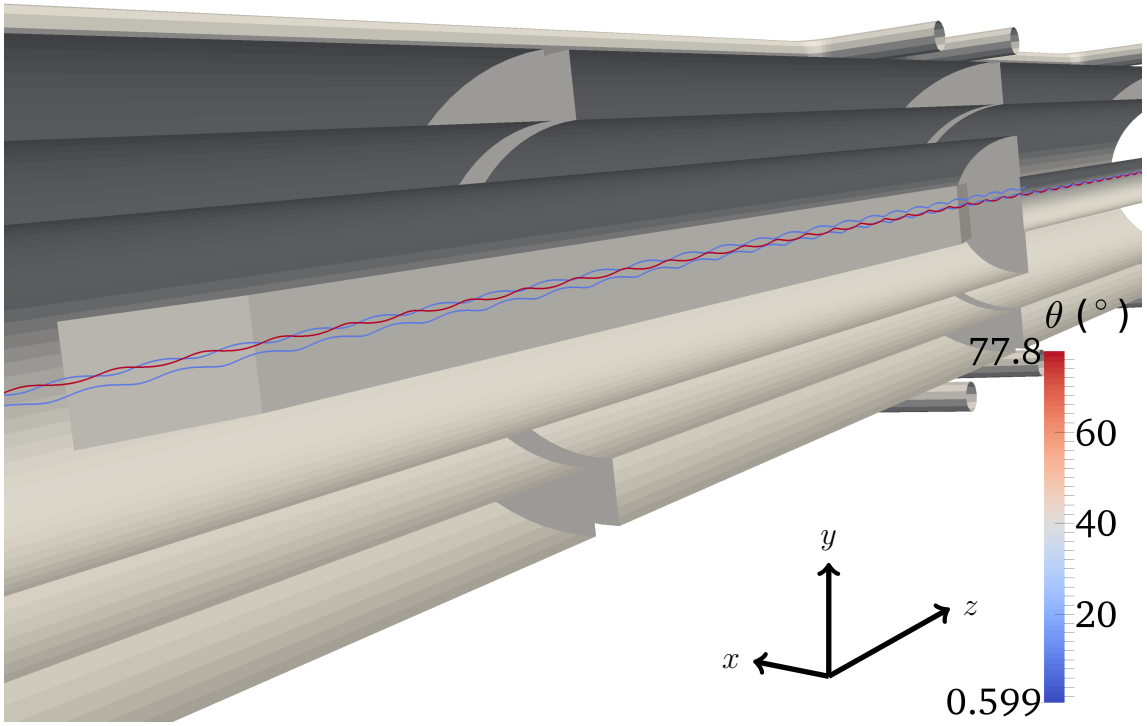

Figure 4.6.: **Trapped electron removal** - This figure illustrates the $\vec{E} \times \vec{B}$ drift to remove trapped electrons. Displayed is a part of the path of an hypothetical electron created in the post acceleration region with parameters leading to magnetic reflection at the RSCM magnet and electrostatic reflection at the post acceleration. The coloring of the electron path is according to its pitch angle with respect to the z-axis, so $\theta < 90°$ means the electron is on its way to the WGTS. After its second reflection (electrostatic), the $\vec{E} \times \vec{B}$ drift leads to the removal, because the path is shifted upwards in y-direction and the electron is stopped at the aperture.

so the drift must be at least twice as large as the diameter of the aperture of the diaphragm. For an adiabatic drift, the potential of the electric dipole must have a smooth transition into its full field, which is achieved via the kinked plates at each end [Bab14]. The removal of electrons which were reflected several times is shown in fig. 4.6. In this figure, an hypothetical electron was created in the post acceleration region with parameters resulting in a too large θ at the RSCM magnet which leads to its first reflection. Additionally, the parameters are set in a way that the electron cannot pass the electric potential of the post acceleration electrodes and is therefore reflected a second time. As shown in fig. 4.6, even electrons with such improbable characteristics would be safely removed by the $\vec{E} \times \vec{B}$ drift and the diaphragm. However, it is very unlikely that electrons coming from the WGTS will reach the E-gun: they first have to pass the diaphragm with its offset and then they have to pass the E-gun front plate aperture after undergoing the $\vec{E} \times \vec{B}$ drift. And finally, they need a kinetic energy more than the potential difference between E-gun back plate and ground electrode (normally 18.6 kV) to reach the E-gun plate.

Figure 4.7.: **Quarter cut of Rear Section geometry in** KASSIOPEIA - This figure shows again the Rear Section geometry implementation into KASSIOPEIA, but this time in a quarter cut view to expose the electrodes. Like in fig. 4.3, the figure is colored accordingly to the CAD (fig. 4.1) and the Rear Section schema (fig. 4.2). E-gun and post acceleration electrodes are visualized in green and the dipole electrodes in yellow; the previously shown magnets (fig. 4.3) are also displayed. Another advantage of the quarter cut view is the visualization of the electron paths in the Rear Section; this picture visualizes the path of the E-gun beam (1000 electrons) in magenta.

39

4.3. Kassiopeia

One major topic of this thesis was to implement the Rear Section in the most recent KATRIN simulation software KASSIOPEIA [Fur15, Gro15, FG+15], in the latest version 3. KASSIOPEIA is a very powerful electromagnetic field calculation and particle tracking software written in C++, developed and maintained by the KATRIN collaboration members mainly at the Karlsruhe Institute of Technology (KIT) and the Massachusetts Institute of Technology (MIT). Together with other modules like KGEBAG [Cor14] for geometry definitions or KEMFIELD [Cor14] for electromagnetic field calculations, KASSIOPEIA is part of the KATRIN software package KASPER, providing all possibilities to simulate particle trajectories or analyze data in the KATRIN experiment. The working principle is based on the tracking of a charged particle through a static geometry defined by configuration files (module KGEBAG) by splitting up the path into several steps and solving the equation of motion for each step to compute the momentum of the particle. The motion is thereby controlled by electromagnetic fields which can be calculated from the discretized geometry with KEMFIELD.

4.3.1. Usage of Kassiopeia

The configuration and control of KASSIOPEIA happens via configuration files written in XML syntax. For the Rear Section, the geometry definitions (see sec. 4.3.2) were split into several files, each for one type of geometry. Those geometry definition files are then loaded in one file and assembled to their relative positions. Now that one has the whole geometry defined, it is possible to define object properties like potentials for the electrostatic components or currents for the magnetic components. This features are defined in an extended geometry file which loads the previous defined geometry.
In the simulation file itself, the extended geometry file is loaded and the geometries assembled before the electromagnetic field calculation methods (see sec. 4.3.3) are specified. Afterwards the particle tracking parameters like particle generator, tracking precision and possible tracking terminators are stated (see sec. 4.3.4). Additionally, the desired output parameters have to be specified to be able to analyze the simulated data.

4.3.2. Geometry definition

The geometries are all defined within the KGEBAG [Cor14] package. This section will just give a short overview of the geometries used for the Rear Section split up into magnets and electrodes, the complete configuration files can be found in appendix A.

Magnets

The magnets responsible for the magnetic guiding field are all defined as cylinder tubes. For this kind of geometry, two z-values give the length of the cylinder and two radii give the thickness of the cylinder tube. Assigning the cylinder tube a current in the extended geometry file results (if loaded in the field calculation) in an axisymmetric magnetic field.

The magnetic dipoles are not as easily defined as the guiding magnets. The geometry of choice were rods with a fixed radius (see fig. 4.3 and fig. 4.7), where the rounded corners are implemented as vertices (for each corner seven vertices create a sufficiently round the corner). The procedure to calculate the magnetic field of the magnetic dipoles is similar to the guiding magnets, so defining a current through the rod is enough.
The meshing of the magnets in general does not have to be too fine, since the magnets are all outside the beam tube and particles do not interact directly with the geometry of the magnets.

Electrodes

All axisymmetric electrodes (which excludes the electric dipole electrodes) are defined as 2D lines and then rotated around the symmetry axis. For the vacuum system as ground electrode, a simplified design (compared to the CAD) was chosen to save computation time without losing precision: since they do not affect the electromagnetic calculation for the Rear Section, the pump ports are not included and the beam tube is assumed to be infinitely thin (see fig. 4.7).
Despite all differences, the definition principle of the E-gun plates and the post acceleration electrodes is the same. In contrast to the beam tube, both are defined with a finite thickness and rounded corners, which is achieved by rotating a closed 2D loop around the symmetry axis (see fig. 4.7). To enable the rotation of the E-gun around the center of the front plate, the E-gun plates are assembled in a separate space. This allows for the proper rotation of the E-gun when combining it with the rest of the Rear Section. The assembling of the E-gun is described by a rotation followed by a translation, which is equal to a coordinate transformation of the form

$$\vec{x}_{\mathrm{RS}} = \begin{pmatrix} \cos\alpha & 0 & \sin\alpha \\ 0 & 1 & 0 \\ -\sin\alpha & 0 & \cos\alpha \end{pmatrix} \vec{x}_{\text{E-gun}} + \begin{pmatrix} 0 \\ 0 \\ -4.58\,\mathrm{m} \end{pmatrix} \tag{4.6}$$

By design, the E-gun rotation angle α is limited to the range from $-15°$ to $+15°$ [Cou14].

For the non-axisymmetric electric dipole electrodes, an extruded line segment was used to simulate the plates, one for the large plates in the middle and one for the kinked plates at each end. These two geometry definitions are then used several times to form the electric dipole by assembling them to a separate space which is then placed in Rear Section geometry (see fig. 4.7).
In contrast to the magnets, the meshing of the electrodes is very important. Non appropriate meshing can cause failure of the field computation or even be the reason for non-convergence of the charge density calculation. To avoid this, the meshing elements (triangles) are designed to have an aspect ratio smaller than 30, see fig. 4.8[3].

4.3.3. Field computation

The field computation in KASSIOPEIA splits up into magnetic field calculation and (static) electric field calculation and is managed by the KEMFIELD package [Cor14]. The static electric field calculation in turn is split into an initial charge density calculation and then calculating the electric field at each step of the particle trajectory.

[3] The aspect ratio is the ratio of the longer side to the shorter side of a meshing element, in this case of a meshing triangle

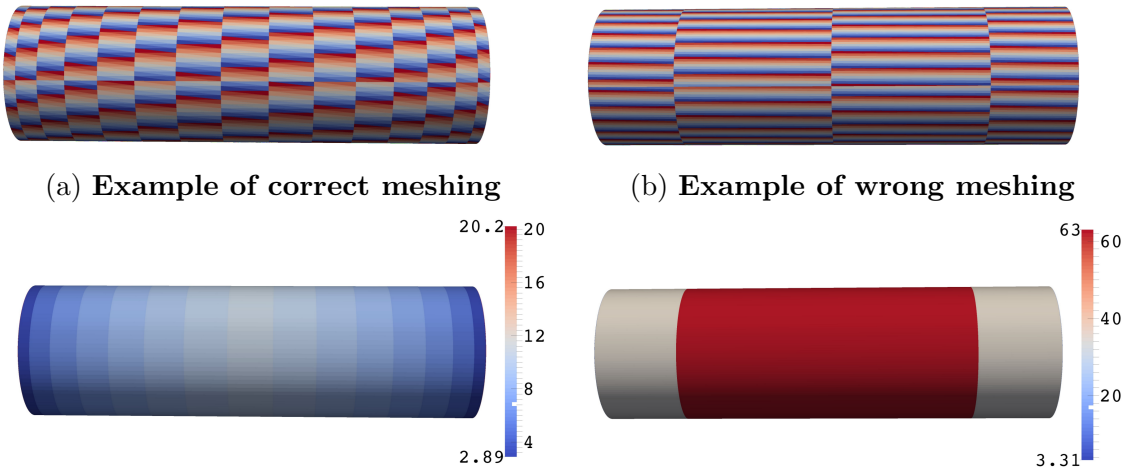

(a) **Example of correct meshing** (b) **Example of wrong meshing**

(c) **Example of correct aspect ratio** (d) **Example of too large aspect ratio**

Figure 4.8.: **Example meshing and aspect ratio** - The meshed element is one of the post acceleration electrodes. Shown are the meshing triangles (top) and the corresponding aspect ratio values (bottom) for a correct meshing (left) and for an arbitrary wrong meshing (right).

Magnetic field calculation

The magnetic field calculation (see fig. 4.4) of the Rear Section in KASSIOPEIA is fully done with the zonal harmonics method [Glü11]. This method makes use of the expansion of the central and remote zonal harmonics by Legendre polynomials to calculate the magnetic field of circular current loops, general axisymmetric coils and magnetic materials. The magnetic fields of the Rear Section are all created by circular current loops, which are defined by the shape of the related geometry.
From an arbitrary point on the symmetry axis (called source point), this algorithm divides the space into three sub-spheres around the source point: the source convergence sphere from the source point to the first source, the remote convergence sphere outside any sources and the region in between. With this kind of partitioning, there is no current (or magnetization) inside the source convergence region or remote convergence region. Inside any source free region, the magnetic scalar potential satisfies the Laplace equation and can be expanded in spherical harmonics. For the case of an axisymmetric source free region, the spherical harmonics simplify to the zonal harmonics. Similar to the magnetic scalar field, the magnetic field components in radial and axial direction can also be expanded in zonal harmonics [Glü11] which enables the calculation of the coefficients of each expansion. Calculating the zonal harmonics expansion at several source points then enables the calculation of the magnetic field at every point.

Electric field calculation

The calculation of the electric field (see fig. 4.5) is more complex as the calculation of the magnetic field. It is split up into two parts: first the charge densities are calculated by a boundary element method solver (BEM solver), and from this calculated charge distribution, the electric field is calculated for every step of the track.
The BEM solver used for the Rear Section is the Robin Hood solver [F$^+$12], which is a matrix inversion method. Once the charge configuration is known, the potential

everywhere in space and not only at the surfaces can be calculated. The matrix inversion uses the Coulomb matrix to solve for the discretized charge densities. Each sub-element i has its own local potential

$$U_i = \sum_{j=1}^{N} I_{ij}\sigma_j \tag{4.7}$$

which is the result of the interaction of all charge densities σ by the Coulomb matrix

$$I_{ij} = \frac{1}{4\pi\epsilon_0}\int_{\Delta S_j} \frac{\mathrm{d}S_j}{\left|\vec{r}_i - \vec{r}_j\right|}. \tag{4.8}$$

For the case of m sub-elements, the Coulomb matrix eq. (4.8) becomes a $m \times m$ matrix to invert. The algorithm performs this matrix inversion step-oriented, starting with picking the two elements whose potential is furthest off the average potential. It then redistributes the discretized charges until the two picked charges are at the same potential which results in a new charge distribution. This process is repeated several times and leads to a quick convergence due to the interaction of the discretized charges. The calculation is terminated when the maximum difference between average potential U_0 and U_i (eq. 4.7) falls below a user-defined precision

$$\varepsilon = \frac{\sqrt{\frac{1}{N}\sum_{i=1}^{N}\left(U_i - U_0\right)^2}}{U_0}. \tag{4.9}$$

For the Rear Section, a precision of 10^{-12} is chosen, which is reached after roughly 14000 iterations for 126944 charge density elements in a specific configuration[4].

Since the Rear Section electrodes are not fully axisymmetric (electric dipole electrodes and the E-gun plates at non-zero angle), the zonal harmonics expansion cannot be used for the electric field calculation. To solve for the electric field of the calculated charge densities, two different field solvers can be chosen: the direct field solver and the FFTM field solver.

The direct field solver evaluates the electric field by using the superposition principle and integrate over all discretized electrode elements. However this direct field evaluation requires a large number of discretizations in order to compute an accurate field for complex electrostatic geometries: the number of function calls to evaluate the electric field increases linearly with the number of discretized charges which increases the computational effort.

An alternative to this solving method is the FFTM field solver [GR87,BG97,CGR99, OLL04]. FFTM here stands for fast Fourier transform of multipoles and is a variant of the very efficient algorithm FMM (fast multipole method). As the name suggests, this algorithm works with multipoles. It replaces a collection of electrode discretizations by an item which has the same effective multipole moment. Thereby the evaluation of the field of a multipole is not dependent on the electrode discretization itself.

[4] GPU usage with OpenCL and enabled matrix element caching

This kind of field evaluation introduces another step in the whole field calculation process: after the charge density calculation, the multipole expansion is executed in order to replace the discretized electrodes by multipoles. During the tracking process, the field solver needs much fewer function calls because it now evaluates the field of a multipole instead of several discretized electrodes. By this the computational effort is reduced and the particle tracking efficiency is increased.

4.3.4. Particle tracking

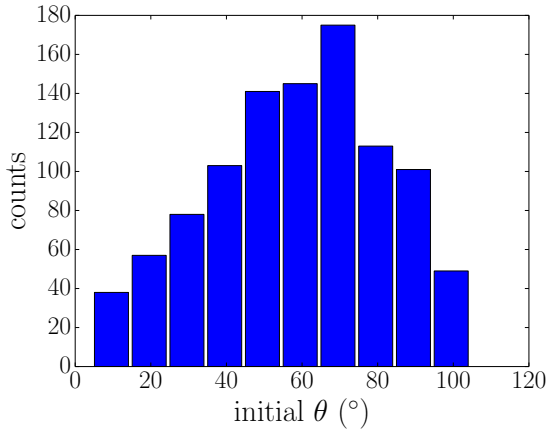

(a) **Initial θ for $\alpha = 15°$ and fiber ID= 3**

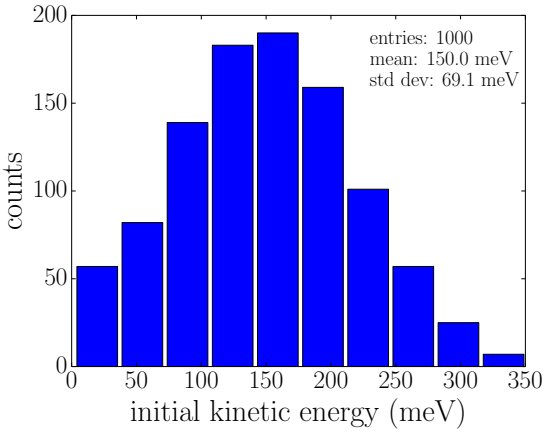

(b) **Initial kinetic energy for $\alpha = 15°$ and fiber ID= 3**

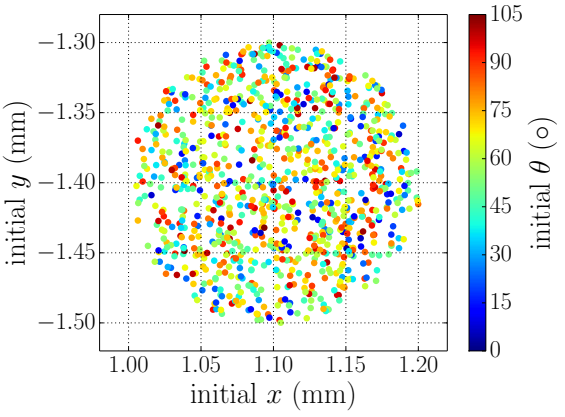

(c) **Initial positions for $\alpha = 15°$ and fiber ID= 3** - The initial positions are distributed isotropically about the fiber surface, as well as the initial directions.

Figure 4.9.: **Monte Carlo distribution of the initial parameters** - Shown are the initial distributions of the particle parameters position, θ and E_{kin} for 1000 electrons, generated by the fiber 3 and an E-gun pitch angle of $\alpha = 15°$. The initial positions in fig. 4.9c are given in the (tilted) E-gun coordinate system to simplify the identification of the fiber position, whereas the initial θ is given in the (non-rotated) Rear Section coordinate system.

The particle tracking starts with the generation of the particles (in this case electrons), setting the initial position, initial direction of the momentum, initial kinetic

energy and initial time. A very useful feature of KASSIOPEIA is the possibility of setting the initial position and initial direction relative to a surface, which simplifies the simulation of the E-gun a lot. The isotropic emission of electrons from an E-gun fiber can be implemented by the Monte Carlo distribution of the initial parameters (see fig. 4.9). The photo-emission of the electrons is defined through a Gaussian distribution of the electrons with a mean kinetic energy of 150 meV and a standard deviation of 75 meV. Those values are used as an estimation of the surplus energy of the electrons due to the photoelectric effect until the energy distribution of the light source is measured experimentally. In fig. 4.9b, the distribution has a slightly smaller standard deviation of 69.1 meV, but this small difference to 75 meV is the result of the random MC generator. Fig. 4.9a shows that there are more electrons created with large θ which is needed in order to satisfy the isotropic generation. Values for θ up to 105° are possible – the usual limit of 90° can be exceeded due to the tilt angle of $\alpha = 15°$ at the E-gun. Combining the isotropic initial position and the isotropic initial θ leads to the plot shown in fig. 4.9c. It nicely confirms the isotropy because there are no local extrema in neither coloring (stands for the polar angle-with respect to the z axis) nor point density (stands for the positions). However one has to take care that the initial x and y are given in the tilted E-gun coordinate system, so one has to translate the E-gun back to the origin and then take the inverted rotation matrix to get the E-gun coordinates:

$$\vec{x}_{\text{E-gun}} = \begin{pmatrix} \cos\alpha & 0 & -\sin\alpha \\ 0 & 1 & 0 \\ \sin\alpha & 0 & \cos\alpha \end{pmatrix} \left(\vec{x}_{\text{RS}} - \begin{pmatrix} 0 \\ 0 \\ -4.58\,\text{m} \end{pmatrix} \right) \tag{4.10}$$

After the creation of the electrons, the particles are tracked through the electromagnetic fields. Depending on the required precision, one can choose between different tracking techniques: the exact tracking calculates the full momentum for each step and is therefore the most exact but also the slowest method. For the case of adiabatic tracking, the calculation makes use of the adiabatic assumption which makes it a very fast method. Especially in strong magnetic fields ($> 3\,\text{T}$) the adiabatic tracking is advantageous because it does not follow the numerous cyclotron motions but only the center of motion. On the other hand, the adiabatic assumption can cause errors in weaker magnetic fields, therfore one has to be careful with its usage. Another form of tracking is the magnetic field line tracking which simply follows the magnetic field line on the place the electron was created. This is a very useful tool for the visualization of the magnetic flux tube and for example showing that the flux tube fits into the geometry.

Endless calculations, for example if the particle is trapped, can by avoided by a terminator which stops the particle tracking upon reaching a maximum number of steps. Another way of stopping the particle tracking is the definition of maximum or minimum z-values to limit the particle tracking to the required region. Recently implemented was a terminator which allows for defining a minimum distance the tracked particle may have to a surface and terminating the track if this threshold is undercut. This terminator superseded a previously used intersection particle stopper. This intersection terminator was insufficient in the reliable detection of particles passing through surfaces. Therefore, the minimum distance terminator is applied to all surfaces except the E-gun cathode. The minimum allowed distance is 50 µm.

The navigation module in KASSIOPEIA loads the previously defined geometry and

for each spaces it is possible to assign tracking methods, step sizes or output configurations separately.
The simulation can be started with various parameters like number of runs or events, the seed for Monte Carlo simulations, the navigation space, electromagnetic fields, generator and the root trajectory are defined. Additionally, the writer is specified which can be any combination of writing to a ROOT[5] file for further analysis or a VTK[6] file for visualization purposes.

4.4. Simulations

Using the fixed parameters of the already advanced electromagnetic design, first simulations were carried out to confirm the working principles of each component. Furthermore those first simulations show that the simplifications used with KGS package are acceptable and the previous results are mainly still valid.
Since the first configuration for tracking electrons through the Rear Section was computationally intensive, the simulation itself needed to be optimized first (sec. 4.4.1) before optimizing the electromagnetic design of the Rear Section. Comparing the speed after the optimizations with the final tracking configuration in KASSIOPEIA to the speed of the KGS package and the first tracking configuration shows an enormous speed-up in terms of computing time (sec. 4.4.2).
After these tracking optimization simulations, the first optimization for the Rear Section is conducted by fixing the E-gun fiber positions due to optimum electron starting positions (sec. 4.4.3). With these fiber positions then the settings are optimized with regard to minimizing the angular spread of the electrons maximum pitch angle in the WGTS. All the configurations found in this optimization process fulfill the requirements for the Rear Section specified in sec. 4.1 and can therefore be directly used for E-gun operations.

4.4.1. Tracking performance optimization

The first thing to optimize was the meshing, since it caused field calculation errors during the particle tracking. After the meshing was revised to meet an aspect ratio smaller than 30 for all elements, the field calculation worked. At the beginning, the tracking method of choice was the exact tracking for the whole Rear Section. But since this method is rather computationally intensive, some effort was put in finding a compromise between tracking speed and precision.

In a first attempt, the adiabatic tracking was used for tracking particles with z-values larger than $-1.6\,\mathrm{m}$, which means a change from exact to adiabatic tracking in a magnetic field of $0.15\,\mathrm{T}$. This position was chosen for starting because at this point the electrons already passed the magnetic dipoles which affect the path of the electrons.
However, the magnetic field seems not to be strong enough at this position to enable adiabatic tracking, because the angular distribution in the WGTS does not match the reference distribution (see fig. 4.10). For this figure, 1000 electrons were simulated, starting at fiber 0 with an E-gun plate potential difference of $3.6\,\mathrm{keV}$ and an E-gun tilt angle of $10°$ and terminated in the mid of the first WGTS magnet. The reference

[5] ROOT data analysis framework http://root.cern.ch
[6] VTK visualization toolkit http://www.vtk.org/

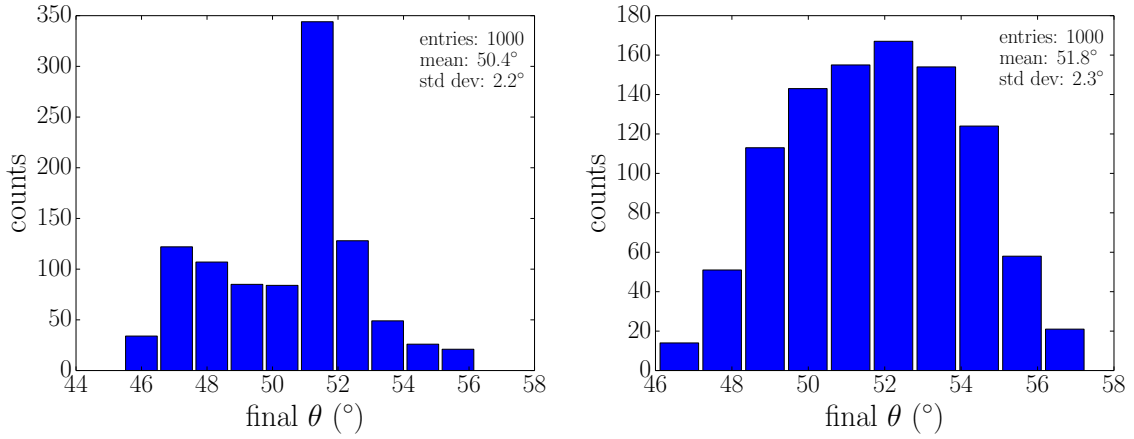

(a) **Polar angle to z in WGTS $\theta_{\mathbf{WGTS}}$ for adiabatic tracking for $z > -1.6\,\mathrm{m}$**

(b) **Polar angle to z in WGTS $\theta_{\mathbf{WGTS}}$ for reference tracking configuration**

Figure 4.10.: **Polar angle to z in WGTS $\theta_{\mathbf{WGTS}}$** - The left figure clearly shows a distribution which does not match the one on the right, so adiabatic tracking cannot be applied for such low z-values.

distribution fig. 4.10b with mean 51.8° and sigma 2.3° is very similar to the Gaussian like found with the KGS package [Bab14] with mean 51.2° and sigma 2.2°. In contrary the distribution generated with the tracking configuration of adiabatic tracking for $z > -1.6\,\mathrm{m}$ has a sharp peak surrounded by a plateau instead of a Gaussian like shape. Therefore, the adiabatic tracking could not be started that early, after looking at the magnetic field strength behavior and some more tests, the adiabatic tracking was chosen to start at $z = -1.1\,\mathrm{m}$ which equals a magnetic field strength of 3 T. The results showed that $z = -1.1\,\mathrm{m}$ is very well suited as adiabatic tracking starting point. Larger z-values would be working equally well, but for the sake of computing time and power savings, adiabatic tracking should be used as early as possible. This configuration has the same angular distribution as the reference tracking method but saves a lot of computing time: with adiabatic tracking starting at $z = -1.1\,\mathrm{m}$, the number of steps and time per track are comparable to the final tracking configuration values displayed in tab. 4.2. But without any adiabatic tracking, the number of steps and time per track increases drastically, from values about 5000 steps in 15 s to 50000 steps in 3 : 30 min for the FFTM field solver and 5000 steps in 3 : 30 min to 50000 steps in 24 min for the direct field solver. This means that the usage of adiabatic tracking in the strong magnetic fields of the superconducting magnets equals a reduction of computing time of one order of magnitude.

Another point to optimize is the step size of the exact tracking method. To enable a lot more precision at very low costs of computing time, the step size in the E-gun space was drastically decreased: from 16 steps per cyclotron turn to 128 steps per cyclotron turn. For estimating the additional computing time one has to consider the size and the characteristics of the E-gun space. The E-gun is placed in a low magnetic field, so that the electrons do not perform as many cyclotron turns as in the stronger magnetic field at the end of the Rear Section. Furthermore, the electrons are very low energetic in this space – their kinetic energy just increases from close to zero (see fig. 4.9b) to values on the low keV scale – hence there are not many steps in this space, even if the E-gun is tilted to the maximum angle. Decreasing

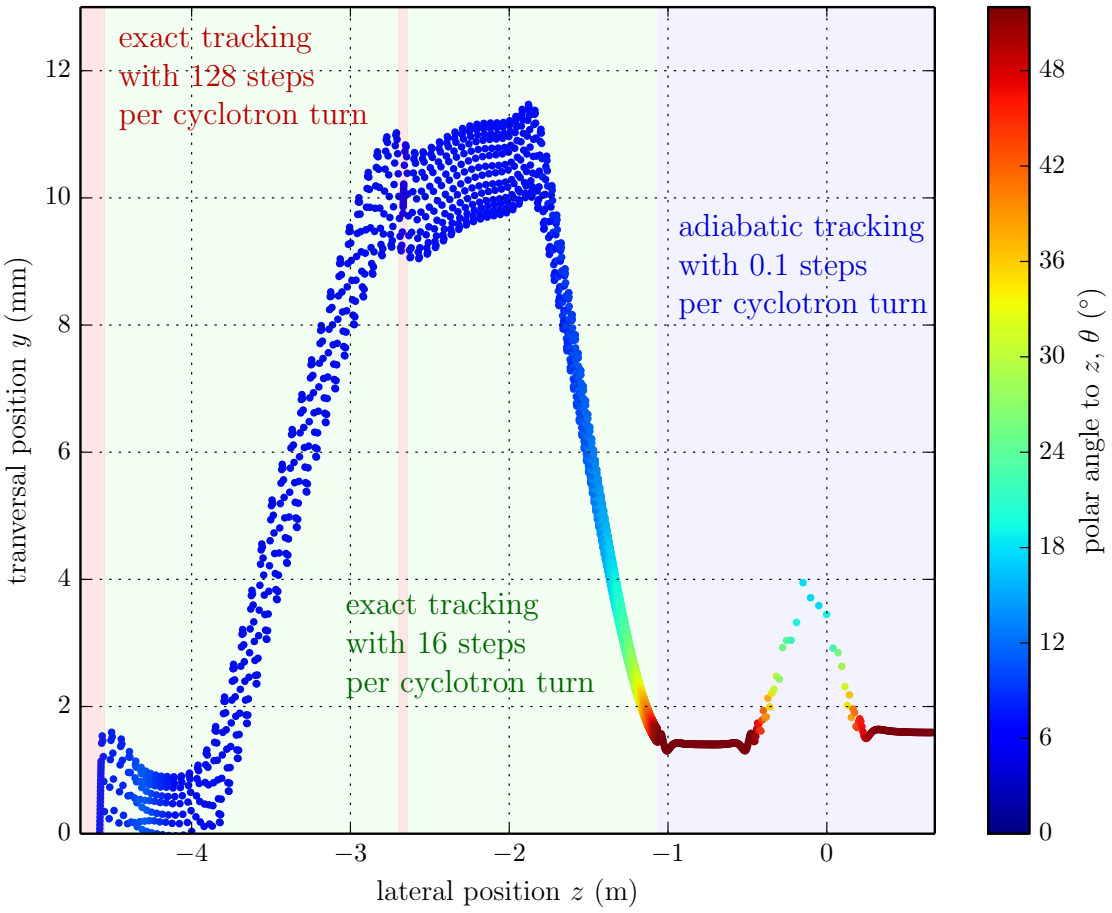

Figure 4.11.: **Tracking configuration** - The regions where the different tracking methods apply are background colored in the appropriate color: red for exact tracking with 128 steps per cyclotron turn, green for exact tracking with 16 steps per cyclotron turn and blue for adiabatic tracking with 0.1 step per cyclotron turn.

the step size from 16 steps per cyclotron turn to 128 steps per cyclotron turn in the E-gun space results in an increase of ≈100 steps in this region which is negligible compared to the total number of steps (≈5000).
Similarly to this finer stepping in the E-gun space, the stepping around the diaphragm at −2.66 m was refined in order to guarantee a correct working of the minimum distance terminator. Likewise, 128 steps per cyclotron turn seem a good choice because all electrons which intersect with the diaphragm are terminated. With a less precise tracking, not all electrons are terminated because there is no step in the critical region. This is the reason why the setting used for creating the reference distribution of θ_{WGTS} fig. 4.10b cannot be used in reality: only exact tracking with 16 steps per cyclotron turn is used, which is not precise enough to terminate particles at the Rear Section diaphragm at $z = -2.66\,\mathrm{m}$. Therefore, in this configuration, electrons reach the WGTS but should be terminated earlier due to physical collision. In the optimized tracking configuration, however, those electrons are terminated correctly.

Combining these optimizations results in the following tracking configuration (see

Table 4.2.: **Results of the Rear Section simulation performance tests** - The usage of GPUs in KASSIOPEIA results in an enormous speed-up especially for the direct field solver. The tracking configuration for the KASSIOPEIA simulations is the one found in sec. 4.4.1 and shown in fig. 4.11. For the calculation of the 126944 discretized charge densities, the previously mentioned (eq. (4.9)) precision of 10^{-12} was taken.

method	time CPU	time GPU
KASSIOPEIA charge density calculation	3.5 d	45 min
KASSIOPEIA direct field solver track	4 h	3 : 30 min
KASSIOPEIA FFTM field solver track	5 min	0 : 15 min
KGS package track	1 h	-

fig. 4.11): inside the E-gun space (between the E-gun plates), the exact tracking method with 128 steps per cyclotron turn is applied (red). This region of very high precision is followed by a region of still precise tracking with 16 steps per cyclotron turn (green) interrupted by the small diaphragm region with again increased precision (red), before for $z > -1.1\,\mathrm{m}$ the region of adiabatic tracking is reached (blue) with only 0.1 steps per cyclotron turn. With this tracking configuration it is now possible to compare two of the electric field solving methods with respect to their performance on CPUs and GPUs and to do a comparison to the outdated KGS package.

4.4.2. Performance tests

The tracking configuration described above enables performance tests of two electric field solvers, namely the direct field solver and the FFTM field solver. The FFTM solver is clearly the recommended one: the results are absolutely the same as the ones from the direct field solver, but the speed of the FFTM solver is a factor of 14 higher for GPU calculations and even a factor 48 higher than the direct field solver for CPU calculations (see tab. 4.2).

The Rear Section charge density calculation and field solving is so time consuming because one cannot make use of any symmetry simplification: the electric dipole electrodes are in no way axisymmetric to the z-axis like the post acceleration and beam tube electrodes. Additionally, the E-gun can be tilted, which for non-zero tilt angles results in extra non-axisymmetric electrodes. This is the reason why one cannot use symmetry simplifications like the zonal harmonics electric field solver.

The largest speed-up by using GPUs instead of CPUs can be achieved for the charge density calculation, because this process can be parallelized well [Cor14]. The usage of an NVIDIA K40c GPU results in a speed-up of a factor of 111 compared to the usage of a Intel Xeon E5649 CPU. This speed-up is not only the outcome of using GPUs but also of the OpenCL[7] implementation: it enables for caching of the matrix elements during inverting the matrix equation eq. (4.8). Because this is done

[7] OpenCL – **Open C**omputing **L**anguage https://www.khronos.org/opencl/

stepwise in the Robin Hood algorithm, the caching helps to reduce the number of necessary iterations: from 19000 for CPU usage down to 14000 for GPU usage.
Regarding the speed-up for the electric field solvers due to the usage of GPUs, the factor is 69 for the direct field solver and 20 for the FFTM field solver. Therefore, the recommended way to simulate the Rear Section is to use the GPUs for the charge density calculation and the FFTM field solver in combination with CPUs for the electron tracking. Though the tracking takes more time using CPUs, one can send several threads with fewer particles to several CPUs, resulting in more simulated particles per hour than using only GPU.

In comparison to the KGS package, KASSIOPEIA provides real 3D simulation which of course consumes more computing power. Still the possibility to use GPUs through the implementation of OpenCL[8] (at least for the charge density calculation) enables a speed-up of the total simulation time from the order of days to the order of hours in combination with the usage of FFTM field solver on CPUs for the particle tracking.

4.4.3. Optimization of electron gun parameters

In order to guarantee that the electron beam provided by the Rear Section meets its requirements specified in sec. 4.1 in terms of angular resolution and energy spread, simulations to set E-gun parameters like optimum starting fiber position were carried out. Optimum starting fiber positions are thereby required to maximize the electron rate at a certain E-gun pitch angle α. Another point is to find the optimum combination of starting fiber, plate potential difference and α to reach the largest transmissible pitch angle in the WGTS (51°).

One of the direct consequences of the simulations of this thesis was the positioning of the optical fiber at the back plate of the E-gun. These positions were determined by minimizing the possibility of electrons hitting the front plate. The optimization parameter for this is to maximize the minimum distance to the front plate surface: the largest possible minimum distance to the front plate surface occurs for an electron passing the front plate exactly in the middle of the aperture leading to a minimum distance of 3 mm (radius of the E-gun front plate aperture). When the electron does not take this central path through the E-gun aperture, its minimum distance value is smaller and the risk of hitting the front plate increases with decreasing minimum distance.
To find the optimum positions of the optical fibers, an over-sized starting electron beam spot on the E-gun back plate of 3 mm radius was assumed. From this spot, 15000 isotropically emitted electrons were tracked through the E-gun with a plate potential difference of 3.6 kV. The tracking configuration was slightly changed compared to sec. 4.4.1 (from 128 steps per cyclotron turn to 256 steps per cyclotron turn) to get even higher precision for the calculation of the minimum distance to the E-gun front plate. Performing this simulation for every possible E-gun pitch angle (from $-15°$ to $+15°$ in $1°$ steps) enables the searching for starting "hotspots": the electrons starting from these "hotspots" have the largest possible minimum distance to the E-gun front plate surface (see fig. 4.12). Comparing all the starting "hotspots" of the different E-gun pitch angles leads to fig. 4.13: there will be several optical fibers distributed point-symmetric to the center of the E-gun back plate.

[8] OpenCL – **Open C**omputing **L**anguage https://www.khronos.org/opencl/

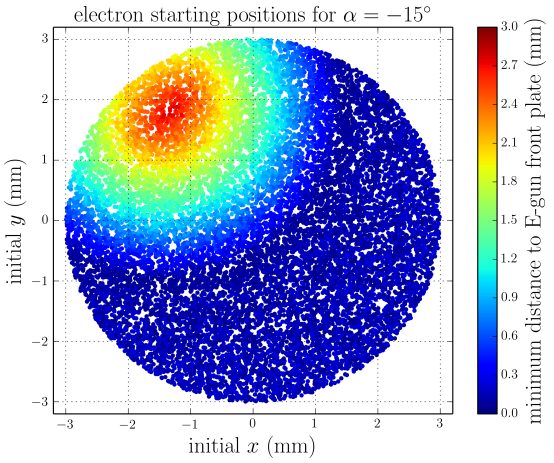

(a) **Optimum starting position for $\alpha = -15°$**

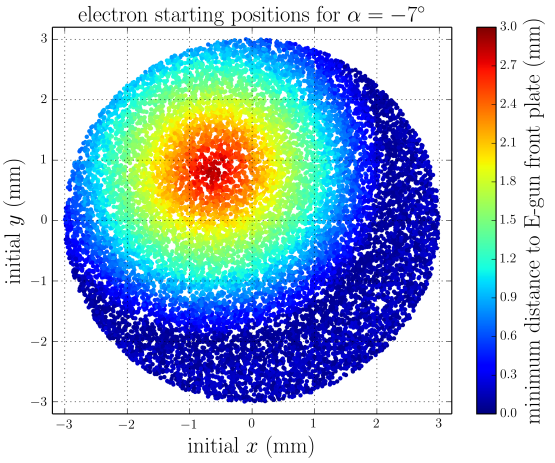

(b) **Optimum starting position for $\alpha = -7°$**

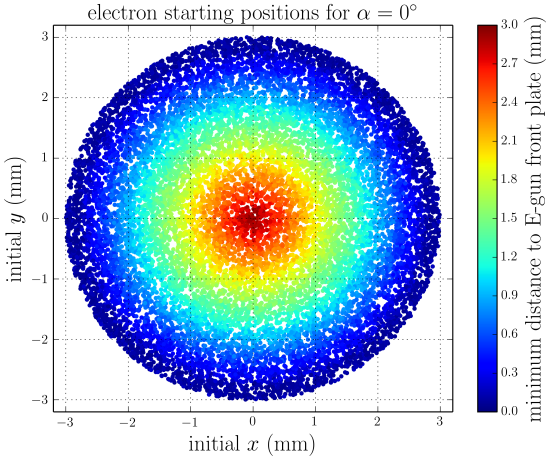

(c) **Optimum starting position for $\alpha = 0°$**

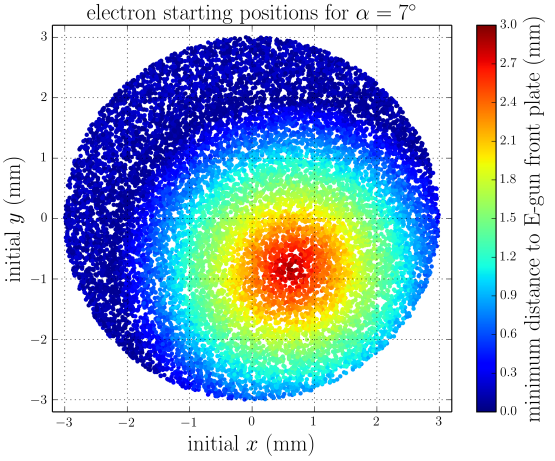

(d) **Optimum starting position for $\alpha = 7°$**

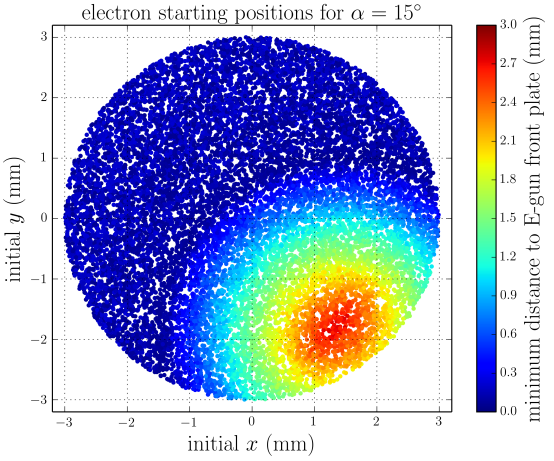

(e) **Optimum starting position for $\alpha = 15°$**

Figure 4.12.: **Optimum starting positions of the electrons for selected E-gun pitch angles** - Shown are the optimum starting positions of the electrons for five roughly equidistant E-gun pitch angles α to indicate the behavior of the optimum starting position for a changing E-gun pitch angle.

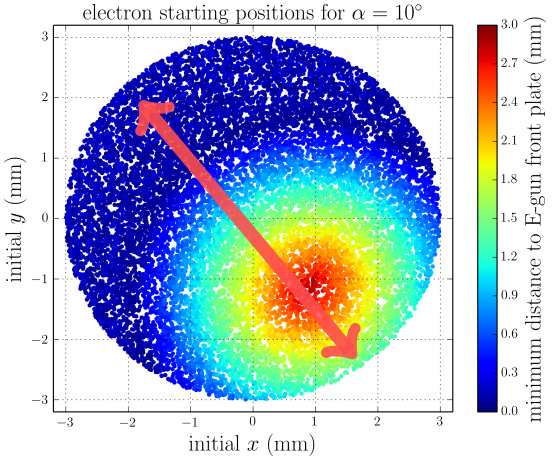

(a) **Optimum starting position for $\alpha = 10°$** - Shown is the optimum starting position for $\alpha = 10°$ and the indication of the optimum starting positions for the other E-gun pitch angles through the red arrow.

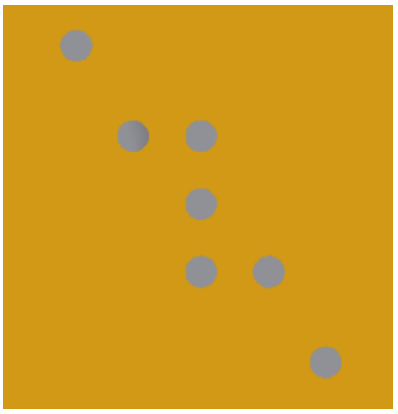

(b) **Optical fiber positions in the CAD** - The positions of the optical fibers are shown in gray, whereas the gold coated E-gun back plate is visualized in gold. The exact values for the optical fiber positions can be found in tab. 4.3.

Figure 4.13.: **Optical fiber positioning due to optimum starting position** - On the left (fig. 4.13a), the optimum starting positions of the electrons (for the different E-gun pitch angles) according to the simulations are displayed. These simulations enabled the positioning of the optical fibers on the E-gun back plate, shown on the right (fig. 4.13b).

To ensure that all electrons pass the E-gun front plate centrally, the minimum electron clearance should not deceed 2.8 mm. By this requirement, the beam spot size and therefore the optical fiber diameter can also be determined.

As an outcome of these simulations, a total of seven 200 µm diameter fibers are required, distributed point-symmetric to the center of the E-gun back plate (see tab. 4.3).

During the simulation process, the effect of changing the E-gun parameters (pitch angle, plate potential difference and starting fiber) on the electron angle θ in the WGTS has been investigated. Enlarging the E-gun pitch angle obviously results in an increase of θ in the WGTS, since the amount of transverse kinetic energy is increased in this case. The same rule applies to the plate potential difference: an increase of the plate potential difference leads for the case of a non-zero E-gun pitch angle also to an increase of θ because the amount of transverse kinetic energy is increased. The effect of using a different starting fiber is not trivial because of the cyclotron motion and the fiber positions. Uncertainties in the starting position of the order of 10^{-4} m and their impact on θ were already investigated [BLM10] and found to be small compared to the impact of other uncertainties. But choosing a different starting fiber is a larger change in the starting position of the order of 10^{-3} m which will have an impact on θ: considering a non-zero E-gun pitch angle and the optical fiber positions from tab. 4.3, one can imagine that different starting positions mean a different starting magnetic field and therefore (see eq. (3.11)) a different θ in the WGTS.

Table 4.3.: **Optical fiber positions and IDs** - Overview of the position of each 200 µm diameter optical fiber and its corresponding ID. The positions are given relative to the center of the E-gun back plate (in mm) in the E-gun coordinate system.

Fiber ID	position (x,y) (mm)
-3	(-1.1, 1.4)
-2	(-0.6, 0.6)
-1	(0.0, 0.6)
0	(0.0, 0.0)
1	(0.0, -0.6)
2	(0.6, -0.6)
3	(1.1, -1.4)

All those impacts on θ are visualized in fig. 4.14, which confirms the above stated assumptions: increasing the potential difference leads to a larger θ_{WGTS} as does increasing α. Choosing a different fiber ID is not trivial because it means a different starting position for the electrons which could also lead to their termination at the diaphragm and therefore reducing the electron rate at the WGTS, symbolized by the marker size of figs. 4.14a, 4.14b and 4.14c.

These simulations show the great flexibility of the Rear Section E-gun, because one can create electrons with $\theta = 51^\circ$ in the WGTS with several configurations. Tab. 4.4 and fig. 4.14d show E-gun settings leading to the desired E-gun pitch angle of $\theta = 51^\circ$ in the WGTS. The first thing to conclude is the fact that all those settings meet the requirements stated in sec. 4.1 in terms of angular resolution, since the largest width of the distributions of θ is a standard deviation of $\sigma_\theta = 2.7^\circ < 4^\circ$. However, the best angular resolution results from choosing the maximum possible E-gun pitch angle $\alpha = 15^\circ$ and choosing the E-gun plate potential difference to be 2.6 kV such that $\theta = 51^\circ$ is fulfilled. This result confirms previous studies to optimize KATRIN E-gun parameters [Leb11] which were based on a simplified analytical approach.

4.5. Summary

The first major task for the Rear Section within this thesis, namely the implementation of the Rear Section in Kassiopeia3, is successfully completed and working. However, there is of course still room for improvements like to further optimize the meshing of the electromagnetic components.

Regarding the total time needed for one track, the optimal solution would be the usage of GPUs. However, GPUs are still rather expensive demanding for a compromise: with the usage of GPUs for the charge density calculation and the usage of CPUs in combination with the FFTM field solver for the electron tracking, the full 3D tracking of electrons in the Rear Section is very fast and exact. With this implementation of the Rear Section, settings for the assembled and built Rear Section

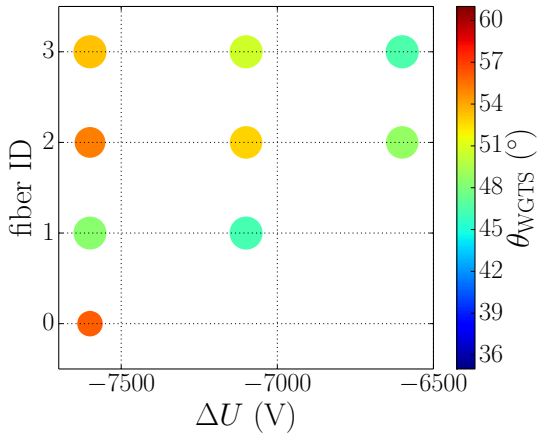

(a) **Resulting $\theta_{\mathbf{WGTS}}$ for settings with $\alpha = 7°$**

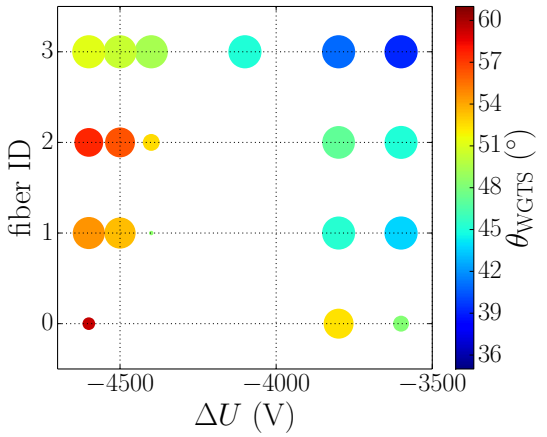

(b) **Resulting $\theta_{\mathbf{WGTS}}$ for settings with $\alpha = 10°$**

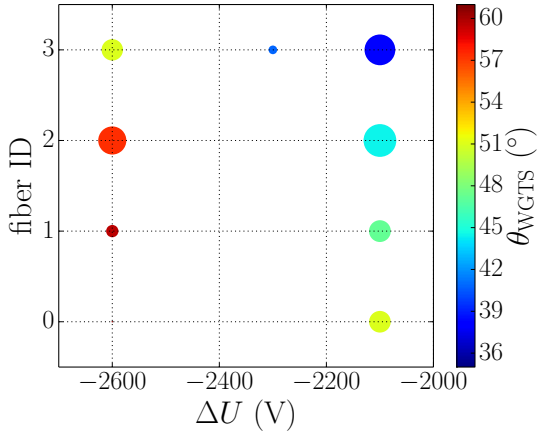

(c) **Resulting $\theta_{\mathbf{WGTS}}$ for settings with $\alpha = 15°$**

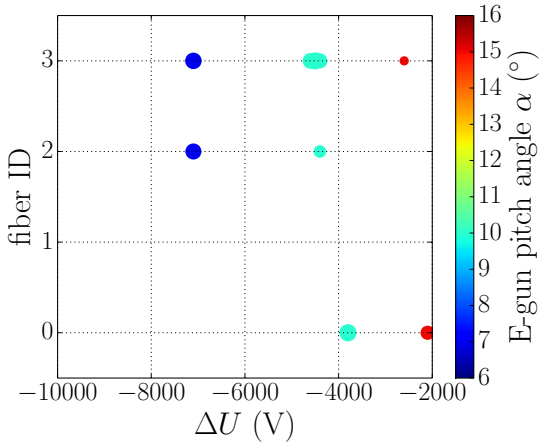

(d) **Configurations resulting in $\theta_{\mathbf{WGTS}} \approx 51°$**

Figure 4.14.: **Visualization of different configurations** - Fig. 4.14a, 4.14b and 4.14c show the resulting electron pitch angle for various settings with marker size proportional to the number of electrons reaching the WGTS. Fig. 4.14d picks the settings which result in $\theta_{\mathrm{WGTS}} \approx 51°$ with marker size proportional to the angular spread of θ_{WGTS}.

can be simulated close to real-time, resulting in very well known characteristics of the E-gun beam.

Previous EMD simulations for the Rear Section using some simplifications are now verified through the full 3D simulations presented here. Furthermore, previous simulations are superseded by the new KASSIOPEIA v3 implementation in regard to realism, output details & visualization and calculation time. The results found during the simulations in this thesis show that the Rear Section in its current CAD design will meet all its requirements in terms of angular resolution and will provide a very narrow electron beam with well understood characteristics. The strategy for minimizing the angular spread of $\theta_{\mathrm{WGTS}} = 51°$ is taking the maximum E-gun tilt angle $\alpha = 15°$ and choosing the fiber position and plate potential difference accordingly such that $\theta_{\mathrm{WGTS}} = 51°$ is reached.

The Rear Section is one of the first components of KATRIN fully implemented in

Table 4.4.: **Rear Section settings to achieve $\theta_{\mathbf{WGTS}} \approx 51^\circ$** - Electrostatic settings of the Rear Section leading to the maximum transmissible pitch angle of the electrons. Simulated are 1000 electrons; if the number of electrons reaching the WGTS is lower than this value, the missing electrons hit the diaphragm. The potential of the E-gun back plate is kept constant at $-18600\,\mathrm{V}$, whereas the front plate potential U_1 is varied to fulfill the plate potential difference. Accordingly, the post acceleration electrodes $U_{2,3}$ are varied to enable equidistant potential differences on the acceleration steps.

α (°)	ΔU (V)	U_1 (V)	U_2 (V)	U_3 (V)	Fiber ID	θ_{WGTS} (°)	$\sigma_{\theta_{\mathrm{WGTS}}}$ (°)	$\bar{\mathrm{e}}_{\mathrm{WGTS}}$
15	2100	-16500	-11500	-5500	0	50.95	1.833	426
15	2600	-16000	-10666	-5333	3	51.03	0.783	417
10	3800	-14800	-9866	-4933	0	52.41	2.691	817
10	4400	-14200	-9466	-4733	2	52.58	1.450	259
10	4400	-14200	-9466	-4733	3	49.34	2.091	1000
10	4500	-14100	-9400	-4700	3	50.34	2.672	1000
10	4600	-14000	-9333	-4666	3	51.18	2.253	1000
7	7100	-11500	-7666	-3833	2	52.82	2.351	963
7	7100	-11500	-7666	-3833	3	50.61	2.472	1000

Kassiopeia3 – which is the final version of the simulation package designed for analysis during the KATRIN runtime. Finally, all components of KATRIN will have their Kassiopeia v3 implemented. The strategy is then to simulate each component by itself and transmit the required characteristics to the next component; in this case providing the Rear Section E-gun beam angle, energy and the respective spread in the WGTS to simulations of the WGTS.

CHAPTER 5

COSMIC NEUTRINO BACKGROUND

"About every neutrino physicist goes through a phase in his or her career and asks 'There's got to be a way to measure the relic neutrino background'"
- Peter Fisher -

The detection of the cosmic neutrino background remains one of the biggest challenges in experimental physics. The measurement would yield information about the universe 1 s after the Big Bang, which is a rather short time compared to the $3.7 \cdot 10^5$ yr at which age the cosmic microwave background originated. A discovery of the cosmic neutrino background would allow testing the existing cosmological models on much earlier timescales.
This chapter starts with an overview of the underlying theory of the cosmic neutrino background (sec. 5.1) before introducing the relic neutrino signal identification at KATRIN (sec. 5.2) and the implementation done in this thesis (sec. 5.3).
Even though the experimental verification of the cosmic neutrino background remains a great challenge, several proposals have been made in the past few years. KATRIN as a next generation neutrino mass experiment should at least be able to set an upper limit on the local overdensity of the relic neutrinos in the Milky Way. While KATRIN is not yet running, studies to improve the sensitivity of KATRIN for measuring the relic neutrinos have been done [FHKŠ14], however none of the studies seems feasible up to now.
In a previous study, the sensitivity KATRIN can achieve with respect to the cosmic neutrino background overdensity was found by Formaggio et al. to be $2{\cdot}10^9$ [KFM10]. In contrast to their ensemble test approach, this thesis will use the profile likelihood method as an alternative approach to evaluate the prospects of constraining the relic neutrino density with KATRIN (sec. 5.4).
Furthermore, the dependency of this sensitivity on parameters like neutrino mass, background rate and measuring time distribution is investigated (sec. 5.4.1) to identify possibilities to increase the sensitivity. Similar to the neutrino mass analysis, the systematic effect of high voltage fluctuations on the relic neutrino overdensity is also estimated (sec. 5.4.3) to get an impression of the underlying overdensity systematics. The results are briefly discussed in sec. 5.4.4 before the chapter concludes with a summary (see sec. 5.5).

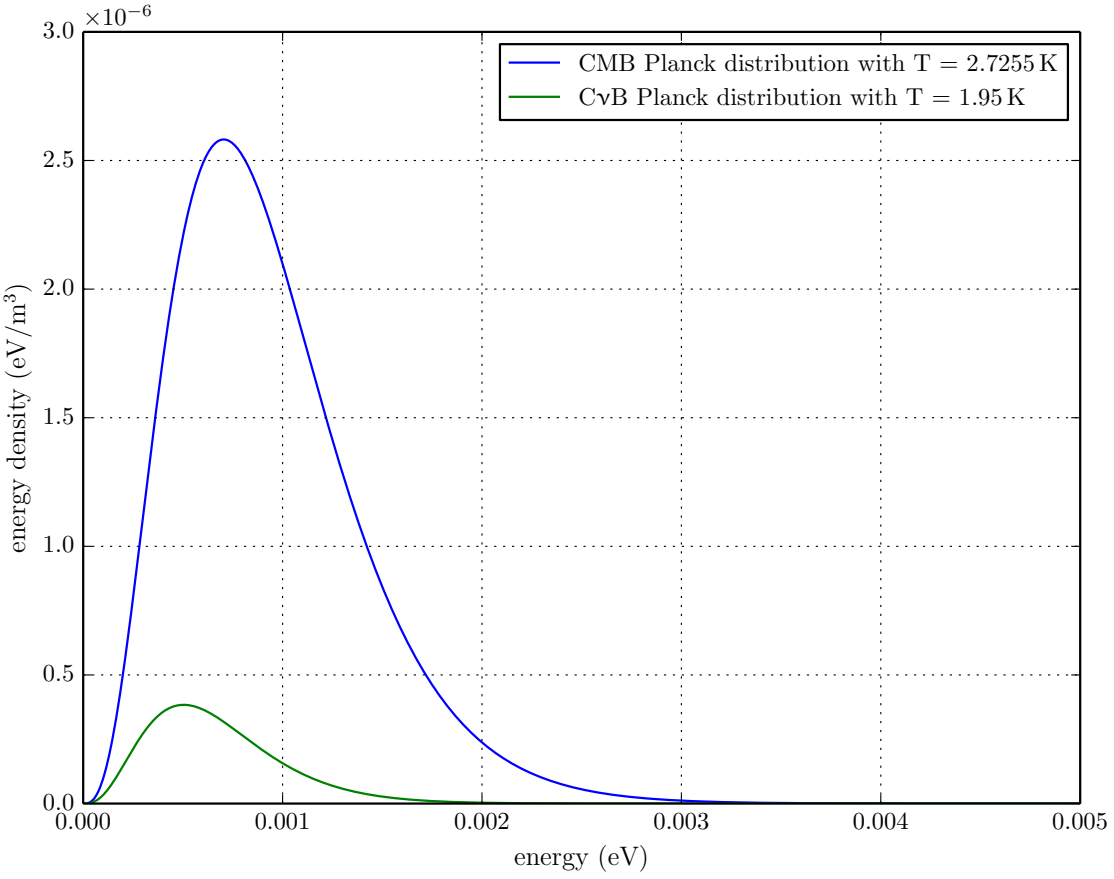

Figure 5.1.: **Energy density distribution of CMB and CνB**

5.1. Theory of the cosmic neutrino background

One of the strongest points in favor of the Big Bang theory is the cosmic microwave background (CMB). The detection of Penzias and Wilson in 1964 [PW65] substantiates the hypothesis of the (thermal) development of the universe. Similar to the CMB consisting of photons, a cosmic neutrino background (CνB) has been proposed to exist, having a slightly lower temperature than the CMB today due to its earlier decoupling. Therefore, a short overview of CMB cosmology is given first (sec. 5.1.1) before turning towards CνB cosmology (sec. 5.1.2). Despite the very low temperature and therefore very low energy of those relic neutrinos today, several proposals to detect these messengers of the early universe have been made; some of them are discussed in the last part of this section (sec. 5.1.3).

5.1.1. Cosmic microwave background cosmology

The cosmic microwave background (CMB) was discovered by Penzias and Wilson in 1964 [PW65], perfectly following Planck's black body radiation law. Its origin traces back to the early universe which temporal development is described by the Friedmann-Lemaître equation

$$H^2 = \left(\frac{\dot{a}}{a}\right)^2 = \frac{8\pi}{3} G\rho_{\text{tot}} - \frac{kc^2}{a^2} \tag{5.1}$$

Table 5.1.: **Cosmological proportionalities** - The different components of the total density have different proportionalities to time t and expansion parameter a.

radiation	matter	vacuum
$\rho_\mathrm{r} \propto a^{-4}$	$\rho_\mathrm{m} \propto a^{-3}$	$\rho_\Lambda = \dfrac{\Lambda}{8\pi G}$
$a_\mathrm{r} \propto t^{1/2}$	$a_\mathrm{m} \propto t^{2/3}$	$a_\Lambda \propto \mathrm{e}^{\beta t}$

with H being the Hubble parameter, $a = a(t)$ the expansion parameter of the universe, G the gravitational constant, ρ_tot the total density and k the curvature parameter. This equation is the solution to Einstein's field equations of general relativity, obtained through applying the cosmological principle by assuming an isotropic and homogeneous distribution of matter and radiation, forming a perfect frictionless fluid, see e. g. [Per09]. The total mass density is built of a radiation, a matter and a vacuum term:

$$\rho_\mathrm{tot} = \rho_\mathrm{r} + \rho_\mathrm{m} + \rho_\Lambda. \tag{5.2}$$

Today, the universe is almost perfectly flat, $k = 0$, and the mass density equals the critical mass density: $\Omega = \rho_\mathrm{tot}/\rho_\mathrm{c} = 1$, with

$$\rho_\mathrm{tot} = \rho_\mathrm{c} \overset{(5.1)}{=} \frac{3H^2}{8\pi G} \approx 10^{-26}\,\mathrm{kg\,m^{-3}}. \tag{5.3}$$

This critical mass density corresponds to a critical energy density of

$$\epsilon_\mathrm{c} = \rho_\mathrm{c} c^2 \approx 5\,\mathrm{GeV\,m^{-3}}. \tag{5.4}$$

At early times, the universe was very compact (see tab. 5.1) and the radiation dominated over the other contributions to the density. Furthermore, the curvature term was also negligible back then. In this radiation dominated era, there was a thermal equilibrium of elementary fermions and bosons which were present in comparable number if $k_\mathrm{B}T \gg Mc^2$ (k_B Boltzmann constant, M mass of the particle (fermion)). Thermal equilibrium demands the time between collisions to be much shorter than the age of the universe to enable the number of collisions necessary to set up a thermal equilibrium. Therefore, particles may fall out of the equilibrium during the expansion and cooling of the universe. The equilibrium reaction for the CMB is the formation and ionization of hydrogen:

$$\mathrm{e}^- + \mathrm{p} \leftrightarrow {}^1\mathrm{H} + \gamma. \tag{5.5}$$

This process forms a plasma of electrons and protons and for thermal equilibrium has a constant ratio of forward to backward reactions, depending on the temperature T. The photons will obviously not decouple (freeze out of the thermal equilibrium reaction eq. (5.5)) until the universe has cooled down to the ionization energy of hydrogen, $k_\mathrm{B}T < 13.6\,\mathrm{eV}$. Because of the Planck distribution of the photons described later, the decoupling does not start immediately when reaching this temperature, since the tail of the Planck distribution contains enough photons to ionize hydrogen

though the average value is below 13.6 eV. The equation describing the temperature dependency of the fraction of ionized hydrogen atoms x is the Saha equation [Per09]:

$$\frac{x^2}{1-x} = \frac{1}{n_{\mathrm{bar}}} \left(\frac{2\pi m_{\mathrm{e}} k_{\mathrm{B}} T}{h^2} \right)^{3/2} \mathrm{e}^{-\frac{13.6\,\mathrm{eV}}{k_{\mathrm{B}} T}} \tag{5.6}$$

with the number of baryons per unit volume n_{bar}, the electron mass m_{e} and the Planck constant h. Inserting typical numbers [Per09] and iteratively varying T in a range of several 1000 K leads to the critical temperature range between 3000 K and 4000 K which equals an energy range of $k_{\mathrm{B}}T$ between 0.25 eV and 0.35 eV. In this range, the fraction of ionized hydrogen atoms x drops drastically, therefore the radiation must decouple in this range [Per09] and the recombination of electrons and protons dominates from now on. Taking $k_{\mathrm{B}}T = 0.3\,\mathrm{eV}$ as stated in [Per09], corresponding to a temperature of $T = 3500\,\mathrm{K}$, results in a decoupling time of the CMB of

$$t \approx 3.7 \cdot 10^5\,\mathrm{yr} \tag{5.7}$$

after the Big Bang. At this point, matter started to become transparent to the CMB and the formation of atoms and molecules began. With this decoupling, the photons formed their own, fully separated system, enabling the description of the CMB with Planck's black body radiation law. The spectral radiance has the typical form of a Bose-Einstein distribution:

$$B_f(f,T) = \frac{2hf^3}{c^2} \frac{1}{\mathrm{e}^{\frac{hf}{k_{\mathrm{B}}T}} - 1} \frac{g_\gamma}{2}, \tag{5.8}$$

leading (with $g_\gamma = 2$ for the number of possible spins of the photons) to a differential energy density of

$$u_f(f,T) = \frac{4\pi}{c} \cdot B_f(f,T) \overset{(5.8)}{=} \frac{8\pi h}{c^3} \frac{f^3}{\mathrm{e}^{\frac{hf}{k_{\mathrm{B}}T}} - 1} \tag{5.9}$$

$$u(E,T) = \frac{8\pi}{c^3 h^2} \frac{E^3}{\mathrm{e}^{\frac{E}{k_{\mathrm{B}}T}} - 1} \tag{5.10}$$

where in the last step the energy relation $E = hf$ for photons was used. The CMB radiation today is measured to be a black body radiation example par excellence with a temperature of $T_\gamma = 2.7255\,\mathrm{K}$ [Oli14], see fig. 5.1. Only in the fourth digit, the temperature becomes direction dependent, revealing the details of the structure of the universe when the CMB decoupled. Integrating the differential energy density eq. (5.10) over all energies yields the total energy density described by the Stefan Boltzmann law:

$$\epsilon_{\mathrm{r}} = \rho_{\mathrm{r}} \cdot c^2 = \frac{4\sigma}{c} T_\gamma^4 = \frac{8\pi^5 k_{\mathrm{B}}^4}{15 c^3 h^3} T_\gamma^4 = 0.26\,\mathrm{MeV\,m^{-3}}. \tag{5.11}$$

This energy density equals a mass density of $\rho_{\mathrm{r}} = 4.65 \cdot 10^{-31}\,\mathrm{kg\,m^{-3}}$, which results in a relative mass density of

$$\Omega_{\mathrm{r}} = \frac{\rho_{\mathrm{r}}}{\rho_{\mathrm{c}}} \overset{(5.3)}{=} 5 \cdot 10^{-5}. \tag{5.12}$$

Comparing this low value with the other contributions to the total mass density reveals the minor role of CMB in the development of the universe today ($\Omega_\mathrm{m} = 0.24$, $\Omega_\Lambda = 0.76$ [Per09]). However, calculating the number density shows that the CMB photons are the by far most abundant particles in the universe despite their low energy density:

$$n_\gamma = \frac{g_\gamma}{2} \int_0^\infty \frac{p^2 \mathrm{d}p}{\pi^2 \hbar^3 \left(\mathrm{e}^{\frac{E}{k_\mathrm{B} T_\gamma}} - 1 \right)} \overset{\left(\substack{E=pc \\ x=pc/k_\mathrm{B}T_\gamma} \right)}{=} \frac{g_\gamma k_\mathrm{B}^3 T_\gamma^3}{2\pi^2 \hbar^3 c^3} \int_0^\infty \frac{x^2 \mathrm{d}x}{\mathrm{e}^x - 1}$$
$$= \frac{1}{\pi^2} \left(\frac{k_\mathrm{B} T_\gamma}{\hbar c} \right)^3 2.404 \approx 411\,\mathrm{cm}^{-3}. \tag{5.13}$$

Though the baryons do have a larger energy density $\epsilon_\mathrm{bar} = 210\,\mathrm{MeV\,m}^{-3}$ than the CMB photons (eq. (5.11)), they are way outnumbered with their number density of only $n_\mathrm{bar} = 0.22\,\mathrm{m}^{-3}$. The only particle species with a number density comparable to the one of the CMB photons are the relic neutrinos, which will be discussed in the next section (sec. 5.1.2).

5.1.2. Cosmic neutrino background cosmology

As described before, particles may decouple from the reactions in the universe and form their own independently developing fireball. Due to the fact that neutrinos only interact weakly, it is expected that neutrinos decouple before the photons of the CMB (cosmic microwave background, see sec. 5.1.1). As the early, radiation dominated universe expands and cools down, the number of relativistic particles forming the radiation decreases. When $k_\mathrm{B}T$ reaches values of few MeV, only photons, electrons, neutrinos and their corresponding antiparticles survive as relativistic particles, forming a thermal equilibrium [Per09]:

$$\gamma\gamma \leftrightarrow \mathrm{e}^+\mathrm{e}^- \leftrightarrow \nu_\alpha \bar{\nu}_\alpha \qquad (\alpha = \mathrm{e}, \mu, \tau). \tag{5.14}$$

The electron-positron annihilation process to neutrinos is a weak process with a collision rate Γ of (v is the relative velocity of electron and positron) [Per09]

$$\Gamma = \langle n_\mathrm{e} \sigma v \rangle. \tag{5.15}$$

Since all the particles in eq. (5.14) are relativistic, the number density n_e of the electrons (or positrons) has the same temperature proportionality as found in eq. (5.13), namely $n_\mathrm{e} \propto T^3$. The annihilation cross section σ is proportional to the square of the center-of-mass energy s of the electron-positron system, $\sigma \propto G_\mathrm{F}^5 s$ (with G_F being Fermi's constant). Therefore, the overall proportionality of the annihilation rate reads as follows:

$$\Gamma \propto sT^3 \propto T^5. \tag{5.16}$$

The neutrinos freeze out of the thermal equilibrium eq. (5.14) when the universal expansion rate described by the Hubble parameter H is larger than the annihilation rate Γ. In the radiation dominated era, the total density and therefore the universal expansion is dominated by radiation, $\rho_\mathrm{tot} = \rho_\mathrm{r}$:

$$H^2 = \frac{8\pi G}{3} \rho_\mathrm{r} = \left(\frac{\dot{a}}{a} \right)^2. \tag{5.17}$$

In order to solve for a temperature dependency of H, either a or ρ_r have to be eliminated. The proportionality between radiation density ρ_r and expansion parameter a is listed in tab. 5.1:

$$\rho_\mathrm{r} \propto a^{-4} \qquad \rightarrow \qquad \dot{\rho}_\mathrm{r} \propto -4a^{-5}\dot{a}. \tag{5.18}$$

This enables the following trick through partial integration:

$$H = \sqrt{\frac{8\pi G\rho_\mathrm{r}}{3}} = \frac{\dot{a}}{a} = \frac{-\dot{\rho}_\mathrm{r}/4a^{-5}}{a} = \frac{-\dot{\rho}_\mathrm{r}}{4\rho_\mathrm{r}} \overset{(\text{partial integration})}{\Rightarrow} \rho_\mathrm{r}(t) = \frac{3}{32\pi G}t^{-2}. \tag{5.19}$$

With this form of the radiation density, the time dependency of H can be found:

$$H \overset{(5.19)}{=} \frac{-\dot{\rho}_\mathrm{r}}{4\rho_\mathrm{r}} = -\frac{(-2)\cdot \mathrm{const}\cdot t^{-3}}{4\cdot \mathrm{const}\cdot t^{-2}} = \frac{1}{2t}. \tag{5.20}$$

What is left now is to connect the temperature and the time, which is done through the comparison of eq. (5.19) with the Stefan Boltzmann radiation law for fermions and bosons

$$\rho_\mathrm{r}\cdot c^2 = \frac{4\sigma}{c}T^4 = \frac{8\pi^5 k_\mathrm{B}^4}{15c^3h^3}T^4\frac{g'}{2}. \tag{5.21}$$

The new number of degrees of freedom g' takes into account that there are now also radiation contributions from fermions, not only bosons as for the CMB. Comparing eq. (5.19) with eq. (5.21) yields the desired connection between time and temperature:

$$t^{-1} = \left(\frac{2\cdot 45c^5h^3}{8\cdot 32\pi^6 G\cdot g'}\right)^{-1/2}(k_\mathrm{B}T)^2\,. \tag{5.22}$$

Using eqs. (5.22) and (5.20) shows the proportionality of H and T:

$$H = \left(\frac{32\pi^6 G\cdot g'}{45c^5h^3}\right)^{1/2}(k_\mathrm{B}T)^2 \propto T^2. \tag{5.23}$$

So when the temperature T drops, the annihilation rate $\Gamma \propto T^5$ (eq. (5.16)) drops faster than the expansion rate $H \propto T^2$ (eq. (5.23)), leading to the freeze-out of neutrinos. Inserting typical numerical values for Γ and H [Per09] yields the critical temperature for this freeze-out of $k_\mathrm{B}T_\mathrm{c} \approx 3\,\mathrm{MeV}$, corresponding to a time of $t_\mathrm{c} \approx 1\,\mathrm{s}$ after the Big Bang. This means that for $t > 1\,\mathrm{s}$, the neutrino fireball expands independently of other particles or radiation, forming the cosmic neutrino background (CνB) today.

To estimate temperature and number density of the CνB, one can use the measured temperature of the CMB (see sec. 5.1.1). But one has to take into account the boost of the CMB photons which they receive after the decoupling of the neutrinos to correctly estimate the temperature of the neutrinos. The boost originates from the annihilation of electrons and positrons to photons, $\mathrm{e}^+\mathrm{e}^- \rightarrow \gamma\gamma$, raising the energy and therefore the temperature of the photons. Since the entropy remains unchanged by the boost, the formula for the temperature of the neutrinos reads as follows:

$$T_1 = \left(\frac{g_2}{g_1}\right)^{1/3}T_2. \tag{5.24}$$

The only thing now hindering the determination of the CνB temperature is the number of relativistic degrees of freedom at neutrino decoupling g_1, because g_2 simply equals the degrees of freedom of photons ($g_2 = 2$). Particles contributing to g_1 are photons, electrons and positrons. The photon contribution is again 2, while the fermion factor is different due to the Fermi-Dirac distribution:

$$u_{\text{fermions}}(E,T) = \frac{8\pi}{c^3 h^2} \frac{E^3}{\mathrm{e}^{\frac{E}{k_\mathrm{B}T}} + 1}. \tag{5.25}$$

Integrating eq. (5.25) yields a factor of 7/8 compared to integrating eq. (5.10). Therefore, the degrees of freedom for a mixture of relativistic bosons and fermions generally take the form

$$g^* = \sum g_{\text{bosons}} + \frac{7}{8} \sum g_{\text{fermions}}, \tag{5.26}$$

resulting in a value for g_1 of

$$g_1 = 2 + \frac{7}{8}(2+2) = \frac{11}{2} \tag{5.27}$$

and allowing the determination of the neutrino temperature

$$T_1 \overset{(5.24)}{=} \left(\frac{2}{11/2}\right)^{1/3} T_2 = \left(\frac{4}{11}\right)^{1/3} T_2. \tag{5.28}$$

Determination of the neutrino number density is then trivial:

$$\begin{aligned} n_\nu &= \frac{g_\nu}{2} \int_0^\infty \frac{p^2 \mathrm{d}p}{\pi^2 \hbar^3 \left(\mathrm{e}^{\frac{E}{k_\mathrm{B}T}} - 1\right)} \overset{\left(\substack{\text{relativistic limit} \\ E=pc,\ x=pc/k_\mathrm{B}T}\right)}{=} \frac{g_\nu}{2} \frac{1}{\pi^2} \left(\frac{k_\mathrm{B}T}{\hbar c}\right)^3 \int_0^\infty \frac{x^2 \mathrm{d}x}{\mathrm{e}^x - 1} \\ &= \frac{g_\nu}{2} \frac{1}{\pi^2} \left(\frac{k_\mathrm{B}T}{\hbar c}\right)^3 \frac{3}{4} \cdot 2.404. \end{aligned} \tag{5.29}$$

The CνB temperature today T_ν is obtained by replacing T_2 in eq. (5.28) by the temperature of the CMB photons today ($T_2 = T_\gamma = 2.7255\,\mathrm{K}$), resulting in $T_\nu = 1.95\,\mathrm{K}$. The resulting CνB energy density together with the CMB energy density is shown in fig. 5.1 (note the factor three, originating from $g_\nu = 6$, taking into account three flavors and the respective antineutrino). Relating the CνB number density eq. (5.13) to the CMB number density eq. (5.29) yields

$$\frac{n_\nu}{n_\gamma} = \frac{g_\nu}{g_\gamma} \left(\frac{T_\nu}{T_\gamma}\right)^3 \frac{3}{4}. \tag{5.30}$$

Now one can either insert all the numerical values or use eq. (5.28) to determine the number density of the CνB today. Choosing the latter and recalling the six degrees of freedom for the neutrinos $g_\nu = 6$ and two for the photons $g_\gamma = 2$ eventually yields

$$n_\nu \overset{(5.28)}{=} \frac{6}{2} \frac{4}{11} \frac{3}{4} n_\gamma \overset{(5.13)}{=} 336\,\mathrm{cm}^{-3}. \tag{5.31}$$

Calculating the total energy density ϵ_ν of the CνB is straightforward. As stated before, the integration of eq. (5.25) yields a factor of 7/8 due to the Fermi-Dirac

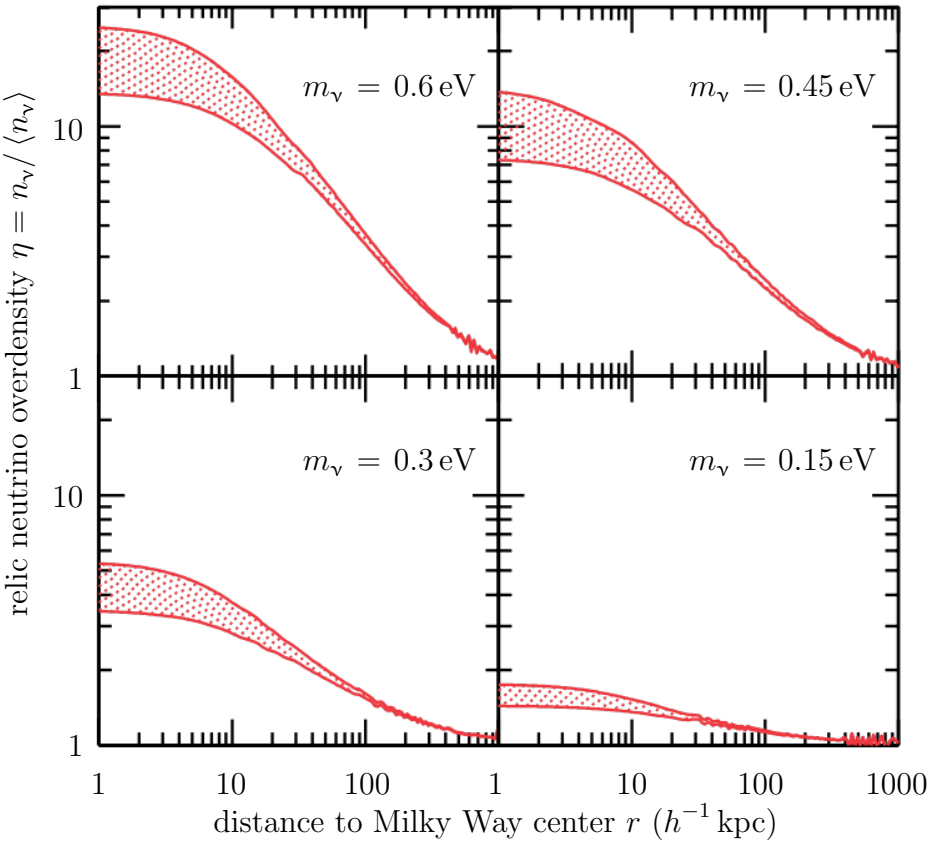

Figure 5.2.: **Relic neutrino overdensity in the Milky Way** - The heavier the neutrinos, the larger the clustering and the overdensity η. The distance to the Milky Way center r is given in h^{-1} kpc with h being of the order 1 (dimensionless factor from Hubble constant $H_0 = h \cdot 100\,\frac{\mathrm{km}}{\mathrm{s \cdot Mpc}}$). Figure adapted from [RW04].

statistic; additionally there are again $g_\nu = 6$ degrees of freedom (with σ Stefan's constant):

$$\epsilon_\nu = \rho_\nu \cdot c^2 = \frac{4\sigma}{c} T_\nu^4 \, 3\,\frac{7}{8} \overset{(5.11)}{=} 3\,\frac{7}{8} \left(\frac{T_\nu}{T_\gamma}\right)^4 \epsilon_\mathrm{r} \overset{(5.28)}{=} 0.68\,\epsilon_\mathrm{r} \overset{(5.11)}{=} 0.18\,\mathrm{MeV\,m^{-3}}. \quad (5.32)$$

The energy density of the CνB is then of the same order as the one of the CMB; the same applies to the relative density Ω_ν, the temperature T_ν and the number density n_ν. So all the comparisons made for the CMB in sec. 5.1.1 still hold, except for the very important fact that the neutrinos have nonzero mass (see sec. 2.3). This makes the CνB today non-relativistic, which is also the reason why the energy density ϵ_ν in eq. (5.32) has no index for radiation. The nonzero mass and low temperature of the CνB today make the clustering of the relic neutrinos on present cold dark matter (CDM) and baryonic matter possible. Ringwald and Wong [RW04] investigate two possible forms of such a neutrino clustering:

- NFW[1] profile (NFWhalo)
- present Milky Way mass profile (MWnow).

[1] Navarro, Frenk and White [NFW96] propose a universal dark matter profile dependent on the two parameters characteristic density and scale radius

Both scenarios result in a local neutrino number density larger than the value of the relativistic Fermi-Dirac distribution of $\bar{n}_\nu = 339\,\mathrm{cm}^{-3}$. Ringwald and Wong argue that the observational mass distribution of the Milky Way is consistent with the theory of baryonic compression and can be reconstructed of halos of originally NFW form, assuming adiabatic contraction [BFFP86]. Therefore, Ringwald and Wong take the NFWhalo clustering of the relic neutrinos as lower bound and the MWnow neutrino overdensity model as upper bound, concluding that the true relic neutrino overdensity $\eta = n_\nu/\bar{n}_\nu$ should lie somewhere in between [RW04]. These lower and upper bounds for the local relic neutrino overdensity are shown in fig. 5.2. The overdensity depends on the neutrino mass since the clustering depends on the velocity and therefore on the mass of the relic neutrinos. The overdensity values at the position of our solar system ($\approx 8\,\mathrm{kpc}$) vary between $\eta = 1.4$ for NFWhalo with $m_\nu = 0.15\,\mathrm{eV}$ and $\eta = 20$ for MWnow with $m_\nu = 0.6\,\mathrm{eV}$ [RW04] (see fig. 5.2).

The estimation of the relic neutrino overdensity by Ringwald and Wong is only one possible explanation. Lazauskas et al. [LVV08] propose that the relic neutrino overdensity scales with the baryon overdensity in galaxy clusters. For a cluster size of 50 Mpc, they estimate an overdensity of the order 10^3 to 10^4. Fässler et al. [FHKŠ13] now combine the result of Ringwald and Wong with the one of Lazauskas et al.: Fässler et al. scale the findings of Lazauskas et al. down to the size of a single galaxy, justified by the result of Ringwald and Wong. With this estimation, Fässler et al. conclude that optimistic overdensities of 10^6 can be expected in the Milky Way.

Hwang and Ma [HM05] list neutrino clustering factors in the range of 10^2 to 10^{14}. They argue that these large overdensities would explain the ultra-high-energy cosmic ray (UHECR) events above the GZK cutoff since such overdensities are needed in order to generate the required "Z-burst" (see sec. 5.1.3) flux. Furthermore, they list weak interaction between neutrinos by the exchange of a very light scalar boson as possible source for neutrino clouds. The conclusion of Hwang and Ma is that even neutrino clustering factors of up to 10^{14} are "by no means nonsense", since such factors are still many orders of magnitude smaller than the baryonic matter clustering factor of $4 \cdot 10^{30}$ [HM05].

5.1.3. Detection of cosmic neutrino background

The solely weak interaction of neutrinos and the particular low energy of the cosmic neutrino background make the detection of the CνB quite a challenge. These difficulties not withstanding, several possibilities to search for the CνB have been proposed in the literature, three of them are mentioned in this thesis; one of them in context to the KATRIN experiment. The first proposal is measuring the CνB by the resonant absorption of ultra-high-energy cosmic ray neutrinos on the low-energy relic neutrinos producing Z bosons [FKR02] which can be detected as a highly boosted "Z burst". Another possibility is "detecting the mechanical force on macroscopic targets due to the 'neutrino wind'" [Hag99]. The last discussed proposed detection method is the induced β-decay, which has no threshold and therefore can be induced by the low-energy CνB neutrinos [FHKŠ11].

Bursts of Z bosons in cosmic rays

The resonant absorption of ultra high energy neutrinos (UHEν) of cosmic rays on low energy relic neutrinos forming Z bosons with mass m_Z would cause dips in the

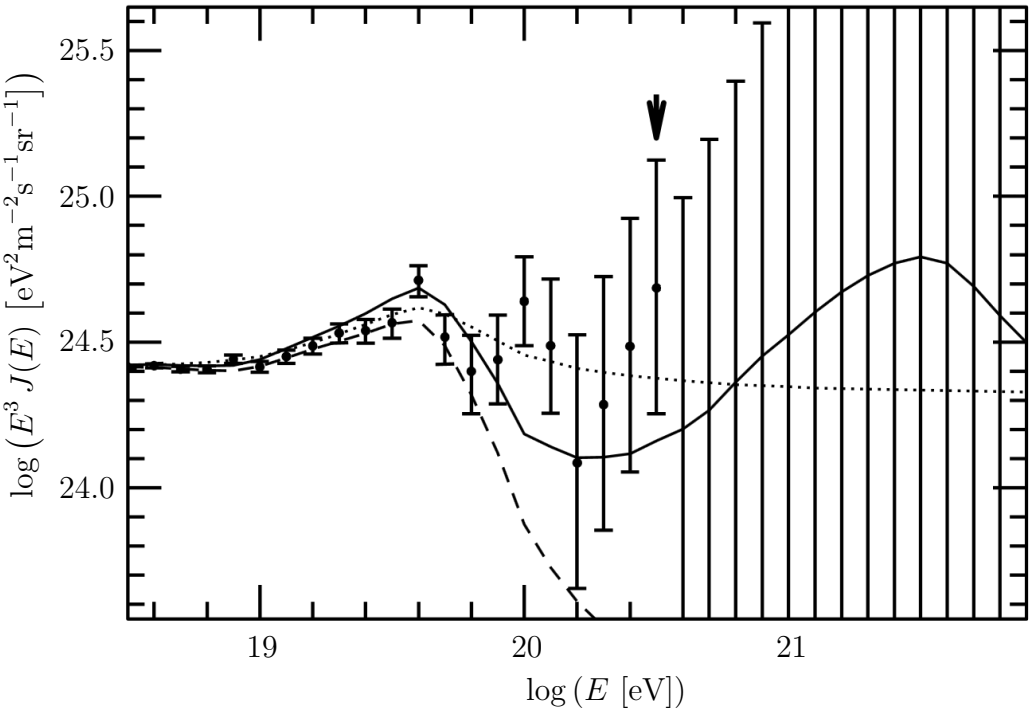

Figure 5.3.: **Effect of Z bursts in UHECR spectra** - UHECR data are shown together with the best fit values for a solely power-law like CR spectrum plus GZK cutoff (dashed), Z bursts originated in the Milky Way halo (dotted) and Z bursts with extragalactic origin (solid). The arrow symbolizes the maximum measured CR energy of $4 \cdot 10^{20}$ eV. Figure adapted from [FKR02].

spectrum of the UHEν around [FKR02]

$$E_\nu^{\mathrm{res}} = m_Z^2/2m_\nu = 4.2 \cdot 10^{21}\,(\mathrm{eV}/m_\nu)\,\mathrm{eV}. \tag{5.33}$$

These highly boosted, decaying Z bosons lead to a so-called "Z burst" scenario which results mainly in ultra high-energy cosmic ray (UHECR) protons increasing the rate of UHECRs as shown in fig. 5.3, being a possible solution to the GZK problem [FKR02][2]. The horizontal part of the spectrum in fig. 5.3 is described well by the classic cosmic ray (CR) power law, whereas the bump at $4 \cdot 10^{19}$ eV is caused by the mentioned "Z burst" protons. A power law like CR spectrum with included GZK cutoff is indicated by the dashed line, whereas the dotted and solid line show best fit curves for two "Z burst" scenarios: the dotted line equals the "halo" scenario with UHECR protons produced in the Milky Way so no GZK effect should be included, while the solid line equals the "EG" scenario. The "EG" scenario assumes the UHECR protons being of extragalactic origin, so it is more realistic to include the GZK effect. In this scenario, the UHECR spectrum features a second bump at $3 \cdot 10^{21}$ eV, caused by "Z burst" remnants. Performing a maximum likelihood analysis for their fits and the measured spectrum, Fodor et al. [FKR02] claim a neutrino mass for the "halo" scenario of $2.75^{+1.28}_{-0.97}$ eV and for the "EG" scenario of $0.26^{+0.2}_{-0.14}$ eV. These results however should be interpreted with a grain of salt, since it is an indi-

[2] resonant scattering of protons on CMB above proton energies of 10^{19} eV should cause a decrease of the rate of UHECRs, which is not confirmed by observations [FKR02]

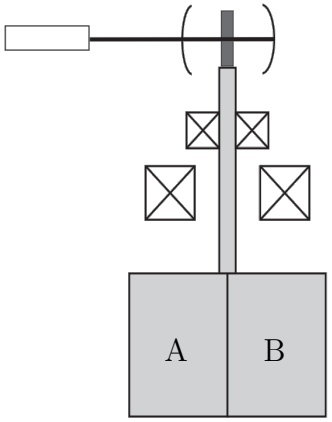

Figure 5.4.: **Torsion oscillator** - The detector to directly measure the CνB would consist of two hemicylindrical masses (A, B) of similar density but different neutrino cross sections which are hooked magnetically. The "neutrino wind" through elastic scattering would cause a torque to the masses. Figure adopted from [Hag99].

rect measurement of the CνB leaving the possibility of other effects to explain the behavior of the UHECR spectrum.

Mechanical detection

A quite optimistic detection method for the relic neutrinos is the one suggested by Hagmann [Hag99]: he proposes a detector which uses the "neutrino wind" caused by the Earth moving through the CνB. A sketch of the detector is shown in fig. 5.4: it consists basically of two hemicylindrical masses with similar densities but different neutrino cross sections [Hag99] which are magnetically hooked. As the Earth travels through the CνB, the "neutrino wind", according to Hagmann, exerts a torque to the masses through elastic scattering. However, Hagmann uses a quite optimistic neutrino mass of 10 eV for his proposal, which is in contradiction to current neutrino mass limits (see sec. 2.4). Nevertheless, this would in principle constitute a direct measurement of the relic neutrinos of the CνB as is the last discussed method, namely the induced β-decay.

Induced β-decay

In the context of this thesis, the most interesting CνB detection method is the induced β-decay since the KATRIN experiment is dealing with β-decaying tritium. The induced β-decay reaction has the advantage of lacking any threshold due to the radioactivity of tritium which is necessary to detect the low-energy CνB. Induced β-decay is a neutrino capture process, first proposed by Weinberg in 1962 [Wei62], of the form

$$ {}^{A}_{Z}N + \nu_e \rightarrow {}^{A}_{Z+1}N' + e^- \qquad \text{and} \qquad {}^{A}_{Z}N + \bar{\nu}_e \rightarrow {}^{A}_{Z-1}N' + e^+. \tag{5.34} $$

The differential capture rate for this process (for the normalization of one incoming neutrino per volume V) is given by [FHKŠ11]:

$$ d\Gamma_\nu = \sum \frac{1}{V} \left|\langle f \,|\, T \,|\, i \rangle\right|^2 2\pi\delta(E_e + E_f - E_i - E_\nu) \frac{d\mathbf{p}_e}{(2\pi)^3}. \tag{5.35} $$

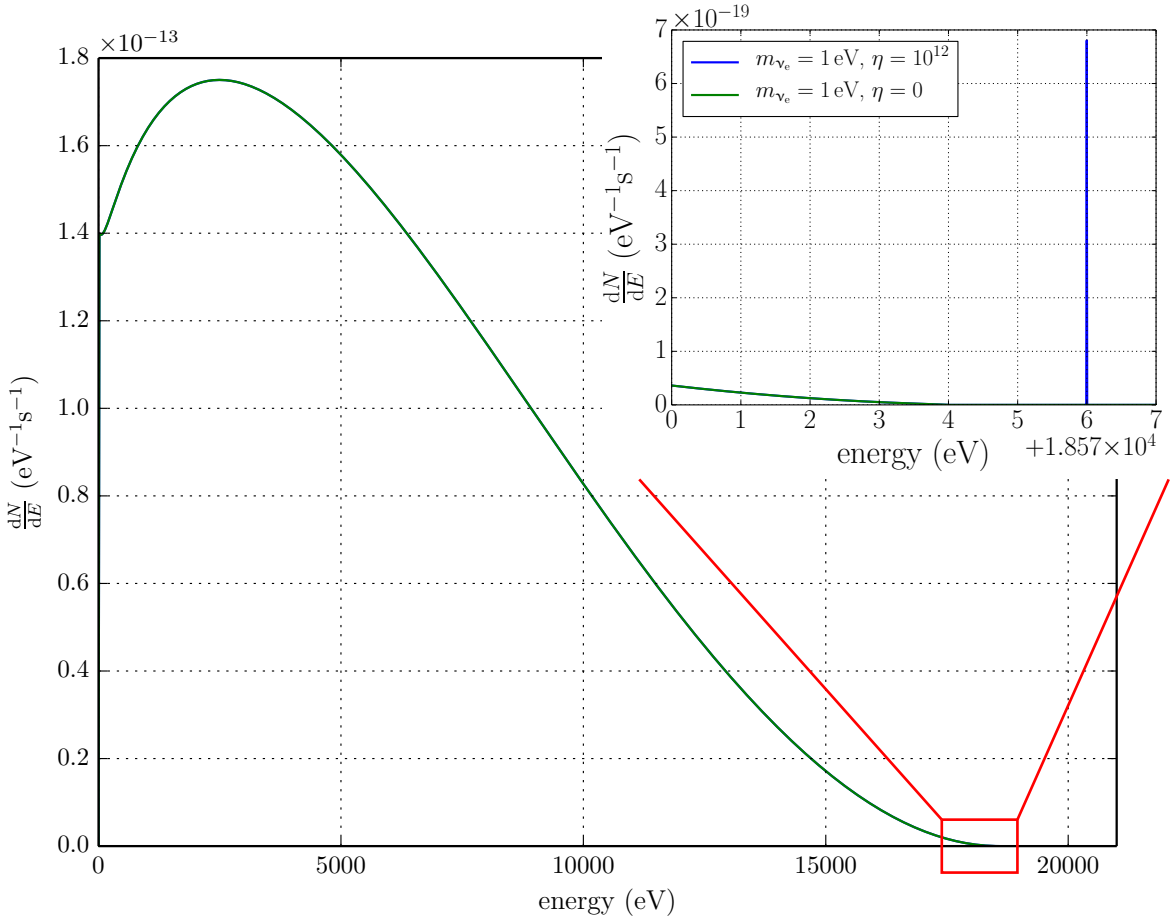

Figure 5.5.: **Example induced β-decay spectrum** - The differential β-decay spectrum of tritium with endpoint $E_0 = 18575\,\mathrm{eV}$ and neutrino mass of $m_{\bar{\nu}_e} \overset{(5.36)}{=} m_{\nu_e} = 1\,\mathrm{eV}$ is shown, together with a zoom to the endpoint region. In this zoom, the signature of the relic neutrino manifests through the sharp line at $E_0 + m_{\nu_e}$ for an optimistic relic neutrino overdensity $\eta = 10^{12}$.

Especially since the neutrino mass was found to be nonzero (see sec. 2.4), this process received new interest because the signal of the neutrino capture is a sharp line located one neutrino mass above the endpoint of the β-decay electron spectrum (see fig. 5.5). Thereby, i and f are the initial and final state, E_i and E_f the initial and final energy respectively and T the transition matrix element.
A detector with sufficient energy resolution finer than $2m_{\nu_e}$ should in principle be able to resolve this relic neutrino signal. In the following, neutrino and antineutrino mass will be treated as one (compare eq. (2.49)), assuming CPT invariance[3]:

$$m_{\bar{\nu}_e} = m_{\nu_e}. \tag{5.36}$$

Calculating the squared transition matrix element T for induced β-decay in eq. (5.35)

[3] if charge parity and time (CPT) invariance is given, particles and their antiparticles have the same mass

is similar to the calculation of the squared matrix element for β-decay; one averages over the projection of angular momentum (magnetic states) of the initial nucleus and sums over the magnetic states of the final nucleus. Additional integration over the electron momenta yields for the relic neutrino capture rate on tritium [FHKŠ11]:

$$\Gamma_\nu(^3\mathrm{H}) = \frac{1}{V}\frac{1}{\pi}(G_\mathrm{F}\cos\vartheta_\mathrm{C})^2 F_0(Z+1, E_\mathrm{e})\left[B_\mathrm{F}(^3\mathrm{H}) + B_\mathrm{GT}(^3\mathrm{H})\right] p_\mathrm{e} E_\mathrm{e} \tag{5.37}$$

with Fermi's constant G_F and the Fermi and Gamow-Teller beta strengths $B_\mathrm{F}(^3\mathrm{H}) = |M_\mathrm{F}|^2$ and $B_\mathrm{GT}(^3\mathrm{H}) = g_\mathrm{A}^2\,|M_\mathrm{GT}|^2$. To account for the possible relic neutrino clustering, resulting in an overall neutrino overdensity η and specifically $\eta_{\bar\nu_\mathrm{e}}$ for the electron antineutrinos, the factor $1/V$ is substituted by $\eta_{\bar\nu_\mathrm{e}}\langle n_{\bar\nu_\mathrm{e}}\rangle$:

$$\Gamma_\nu(^3\mathrm{H}) = \frac{1}{\pi}(G_\mathrm{F}\cos\vartheta_\mathrm{C})^2 F_0(Z+1, E_\mathrm{e})\left[B_\mathrm{F}(^3\mathrm{H}) + B_\mathrm{GT}(^3\mathrm{H})\right] p_\mathrm{e} E_\mathrm{e}\eta_{\bar\nu_\mathrm{e}}\langle n_{\bar\nu_\mathrm{e}}\rangle \tag{5.38}$$

$$= 4.2\cdot 10^{-25}\eta_{\bar\nu_\mathrm{e}}\,\mathrm{yr}^{-1} =: \Gamma'_\nu(^3\mathrm{H})\eta \qquad \text{with } \langle n_{\bar\nu_\mathrm{e}}\rangle = 56\,\mathrm{cm}^{-3} \text{ [FHKŠ11].} \tag{5.39}$$

To remove the uncertainties of the capture rate resulting from matrix element calculations, the measured half-life of tritium $T^\beta_{1/2} = 12.33\,\mathrm{yr}$ was used to pin down a value for the Gamow-Teller strength: $B_\mathrm{F}(^3\mathrm{H}) + B_\mathrm{GT}(^3\mathrm{H}) = |M_\mathrm{F}|^2 + g_\mathrm{A}^2\,|M_\mathrm{GT}|^2 = 5.645$ [FHKŠ11].
In order to assess the low interaction probability of the relic neutrinos, the cross-section can be consulted. In the zero momentum limit ($\mathrm{p}_\nu \to 0$), Cocco et al. [CMM07] find for neutrinos impinging on tritium:

$$\sigma_{\bar\nu_\mathrm{e}}\frac{v}{c}(^3\mathrm{H}) = (7.84 \pm 0.03)\cdot 10^{-45}\,\mathrm{cm}^2. \tag{5.40}$$

This value is even five orders of magnitude lower than current limits on (spin-dependent) elastic scattering of WIMPs[4] on neutrons, which is $\sigma_\mathrm{WIMP} < 3.5\cdot 10^{-40}\,\mathrm{cm}^2$ at a WIMP mass of 45 GeV at 90 % C.L. [AAA+13].
Nevertheless, the cross-section for relic neutrino capture on tritium is still one of the largest, for example the cross-section for relic neutrino capture on rhenium as it is used by MARE (see sec. 2.4.2) is some seven orders of magnitude lower than that on tritium [CMM07]:

$$\sigma_{\bar\nu_\mathrm{e}}\frac{v}{c}(^{187}\mathrm{Re}) = 4.32\cdot 10^{-52}\,\mathrm{cm}^2. \tag{5.41}$$

The isotopes with larger relic neutrino capture cross-sections (about one order of magnitude) than tritium all have at least a factor of 30 larger Q-values[5] [CMM07]. Furthermore, isotopes like ^{15}O are not as readily available as tritium and do have much more complex final state distributions, an effect which is treated in the next sections.

5.2. Signal identification of the cosmic neutrino background at KATRIN

After having discussed the basics of relic neutrino detection, especially relic neutrino capture on β-decaying nuclei, let us now examine the possible imprint of relic

[4] WIMP – **w**eakly **i**nteracting **m**assive **p**article, currently hypothesized to constitute the cold dark matter in the universe [JKG96]

[5] The lower the Q-value, the easier is the energy analysis.

neutrinos in a real experiment, particularly a β-decay experiment. As mentioned before, tritium with its low endpoint of the β-decay spectrum, well known final state distribution and good availability is strongly favored for detecting relic neutrinos, so in the next sections we will deal with the relic neutrino signature at the KATRIN experiment. In the previous section, the signal of relic neutrinos in tritium decay experiments with infinitely good energy resolution was found, which is simply a mono-energetic line located one neutrino mass above the endpoint (see fig. 5.5). However, real experiments do have finite energy resolution, leading to challenges in terms of signal identification. But the energy resolution is not the only challenge to face at KATRIN: for instance, the signal is Doppler broadened by the decaying tritium molecules (sec. 5.2.2) and final state effects of the daughter molecules (sec. 5.2.3), causing broadening or shift of the CνB peak.

5.2.1. Energy resolution

For a MAC-E filter type spectrometer as the one used in KATRIN, the energy resolution ΔE is defined by the ratio between minimum B_{min} and maximum B_{max} magnetic field:

$$\frac{\Delta E}{E} = \frac{B_{\mathrm{min}}}{B_{\mathrm{max}}} = \frac{1}{20000} \qquad \text{with } E = E_0 = 18575\,\mathrm{eV} \;\rightarrow \Delta E = 0.93\,\mathrm{eV}. \tag{5.42}$$

The minimum magnetic field B_{min} is here given by the magnetic field in the analyzing plane (point of maximum electric potential) and the maximum magnetic field B_{max} by the magnetic field of the pinch magnet. For a more detailed explanation of the working principle of KATRIN in general and the energy resolution in particular see chapter 3. The finite energy resolution modifies the measured spectrum through the previously mentioned transmission function $T(E, qU)$, which itself is included in the response function $R(E, qU)$ (see sec. 3.2.3). As KATRIN measures an integral spectrum (see sec. 3.1), the observed signal rate N_{S} at an applied retarding potential U is a convolution of the response function $R(E, qU)$ and the (induced) β-decay spectrum:

$$N_{\mathrm{S}}(qU) = n(\mathrm{T})\,\varepsilon_{\mathrm{det}}\frac{\Omega}{4\pi}\int_{qU}^{E_0+m_{\nu_e}} \frac{\mathrm{d}N}{\mathrm{d}E}(E)\,R(E, qU)\,\mathrm{d}E. \tag{5.43}$$

The prefactor of the integrated spectrum consists of the number of tritium nuclei $n(\mathrm{T}) = 2 \cdot n(\mathrm{T}_2)$ (see eq. (3.4)), the detection efficiency $\varepsilon_{\mathrm{det}}$ and the fraction of the electrons that are emitted with polar angles smaller than the maximum transmissible angle θ_{max}, represented by the solid angle $\Omega = 2\pi \cdot (1 - \cos\theta_{\mathrm{max}})$. In this version of the integrated spectrum eq. (5.43), the upper integration limit is shifted upwards by the neutrino mass to account for the relic neutrino signal located at $E_0 + m_{\nu_e}$. The energy resolution is reflected in the CνB spectrum through the slope of a shoulder (when ignoring final state and Doppler effects), see fig. 5.6b.
Though the energy resolution for KATRIN is in the sub-eV range, this may still not be enough to resolve a potential relic neutrino peak because the neutrino mass may be smaller than the energy resolution.

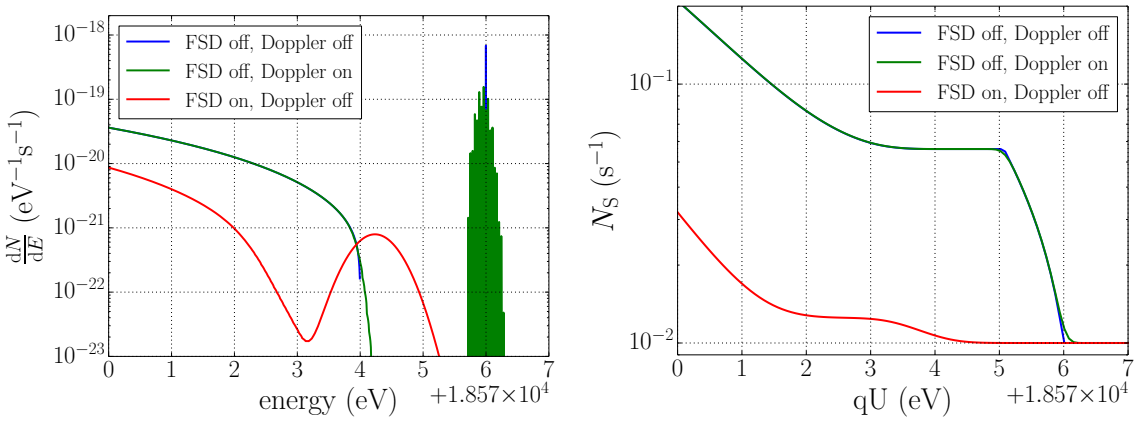

(a) **Differential spectrum** (b) **Integral spectrum**

Figure 5.6.: **Relic neutrino capture spectra with FSD and Doppler effect on/off** - Spectra are created with the convolved FSD implementation, an overdensity of $\eta = 10^{12}$ and a neutrino mass of $m_{\nu_e} = 1\,\text{eV}$.

5.2.2. Doppler effect

Another challenge in relic neutrino signal identification at KATRIN is a property of the gaseous tritium source: due to the finite temperature of the tritium gas, the molecules are not at rest. Due to the Doppler effect, this thermal motion of the decaying molecules induces a broadening of the differential electron spectrum. Mathematically, this can be expressed as a convolution [Kle14]:

$$\left(g \otimes \frac{\mathrm{d}N}{\mathrm{d}E}\right)(E) = \int_{-\infty}^{+\infty} g(E-\varepsilon)\frac{\mathrm{d}N}{\mathrm{d}E}(\varepsilon)\mathrm{d}\varepsilon. \tag{5.44}$$

Thereby, g is the Doppler effect term and E is the electron kinetic energy in the tritium rest frame, whereas ε is the electron energy in the laboratory frame. The Doppler effect term g is given by a Maxwell distribution, but can be written as a Gaussian in the non-relativistic approximation:

$$g(E-\varepsilon) = \frac{1}{\sigma_\mathrm{D}\sqrt{2\pi}}\mathrm{e}^{-\frac{(E-\varepsilon-U_\mathrm{D})^2}{2\sigma_\mathrm{D}^2}}, \tag{5.45}$$

with the mean $U_\mathrm{D} \approx v_\mathrm{u}\sqrt{2Em_\mathrm{e}}$ and standard deviation $\sigma_\mathrm{D} = \sqrt{\frac{2Ek_\mathrm{B}Tm_\mathrm{e}}{M_{\mathrm{T}_2}}}$. U_D depends on bulk velocity of the tritium gas v_u and the electron energy E, while the standard deviation depends on the temperature of the tritium gas and the electron energy. The convolution described in eq. (5.44) results in a broadening and a shift of the CνB-peak. For a temperature of $T = 30\,\text{K}$ and electron energies around the endpoint, the resulting broadening of the CνB signal is of the order 130 meV (compare fig. 5.6).

5.2.3. Final state distribution

The last but arguably most important effect on the CνB spectrum is due to the fact that KATRIN employs molecular tritium: the effect of the excitation spectrum of the tritium daughter molecules. Molecular tritium contains a certain level of

contaminations in the form of the isotopologues T_2, DT and HT decaying to the daughter molecules $(^3HeT)^+$, $(^3HeD)^+$ and $(^3HeH)^+$. After the decay, these daughter molecules of the isotopologues can end up in rotational, vibrational and electronically excited final states (FS). These final state distributions (FSDs) are characterized by an excitation energy E_{fs} and the probability P_{fs} for this particular state to be occupied, and normalized such that $\sum P_{\mathrm{fs}} = 1$ (see sec. 5.3).

Since energy conservation holds, the occupation of a final state of the daughter molecule reduces the energy of the β-decay electron by the energy of the final state. Therefore, the final states need to be accounted for in the spectrum; the effective (induced) β-decay spectrum is a superposition of many single (induced) β-decay branches each having different reduced maximum electron energy, weighted by P_{fs}. This means that the relative abundance of each isotopologue has to be monitored during data-taking to correctly account for the final states in the analysis.

The isotopologue FSDs split up into several sub-distributions, one for each angular momentum J of the parent molecule. Each of these sub-distributions is weighted by their occupation probability through a Boltzmann distribution [Kle14]:

$$P_J(T) = \frac{g_s g_J}{Q} \mathrm{e}^{-\frac{\Delta E_J}{k_{\mathrm{B}} T}}. \tag{5.46}$$

Q is a normalization factor such that $\sum P_J = 1$, ΔE_J is the energy difference of the rotational state to the ground state and T is the temperature of the source gas. The two g factors account fo the spin (g_s) and the rotational (g_J) degeneracy: $g_J = 2J + 1$ and g_s depends on the nuclear configuration of the decaying molecule. For molecules consisting of different nuclei (DT and HT), there is no spin degeneracy because the spins of the different nuclei do not couple: $g_s = 1$. But for molecules built of one type of nuclei (T_2), a spin degeneracy occurs. In the case of molecular tritium, the spin degeneracy is given by the ratio of ortho and para states: in the ortho state, the spins of the nuclei are aligned parallel, forming a triplet with spin 1 and resulting in a degeneracy of 3. On the contrary, in the para state, the spins of the nuclei are aligned anti-parallel, forming a singlet with spin 0 and resulting in no spin degeneracy.

At room temperature (300 K), this spin degeneracy manifests in an ortho-para ratio of $\lambda = 3 : 1 = 0.75$ [Yep14], whereas at low temperatures the para abundance dominates since it is the configuration with lower energy. At KATRIN, the tritium loop causes the source gas to be in thermal equilibrium at 300 K and cools it down only for injection. The molecules pass through a full cycle of cooling, injection and pumping out within a time of only 1.5 s, so hardly any conversion from ortho to para state takes place [Yep14].

The effect of the FSDs of the daughter molecules on the relic neutrino signal is visualized in fig. 5.6 and can be subsumed as a broadening and shift of the sharp line towards lower electron energies. This broadening causes a significant decrease of the signal rate (see fig. 5.6b), making the signal nearly invisible in the integral spectrum for the example overdensity of $\eta = 10^{12}$.

5.3. Signal implementation of the cosmic neutrino background

Before turning to the signal implementation of the CνB into the code in this thesis, let us first consider how previous authors approached this task. A. Kaboth, J. A. Formaggio and B. Monreal in their work [KFM10] as well as A. Kaboth in his PhD thesis [Kab12] used an integral spectrum with a background rate N_b of order 10 mHz (independent of retarding voltage U) of

$$G(qU) = \int_{qU}^{\infty} \frac{\mathrm{d}N}{\mathrm{d}E}\, T(E, qU)\, \mathrm{d}E + N_\mathrm{b}. \tag{5.47}$$

This integral spectrum is the convolution of the transmission function $T(E, qU)$ with the sum of the β-decay and CνB spectrum:

$$\begin{aligned}\frac{\mathrm{d}N}{\mathrm{d}E} = \sum_\mathrm{fs} \Bigg(& N_{\mathrm{T}_2} F(Z,E) p_\mathrm{e} (E + m_\mathrm{e})(E_0 - E)\sqrt{(E_0 - E)^2 - m_\nu^2} \\ & \Theta(E_0 - E(\mathrm{fs}) - m_\nu) + N_\mathrm{C\nu B} \mathrm{e}^{-(E_0 - E(\mathrm{fs}) + m_\nu)^2 / 2\sigma^2} \Bigg) P(\mathrm{fs}).\end{aligned} \tag{5.48}$$

The integral spectrum form eq. (5.47) listed in [KFM10] is slightly different from the one already outlined in this thesis, eq. (5.43). In the following, the latter one will be used in a slightly modified version as it is already implemented in the SSC (source and spectrum calculation, see sec. 5.3.1) code. The integral rate is implemented as:

$$N_\mathrm{S}(qU) = n(\mathrm{T})\, \varepsilon_\mathrm{det} \frac{\Omega}{4\pi} \int_{qU}^{E_0 + m_{\nu_\mathrm{e}}} \frac{\mathrm{d}N}{\mathrm{d}E}(E)\, R(E, qU)\, \mathrm{d}E \; + \; N_\mathrm{bg}. \tag{5.49}$$

The only difference between eq. (5.43) and this form eq. (5.49) is that the latter one takes into account the background rate N_bg which is – as mentioned before – independent of the retarding voltage. As we will see later (see sec. 5.4.1), this background plays an important role for the sensitivity of KATRIN for measuring the CνB.
To implement the CνB signal into SSC, a similar form to eq. (5.48) was chosen, consisting of the differential β-decay spectrum plus a term for the CνB signal:

$$\begin{aligned}\frac{\mathrm{d}N}{\mathrm{d}E} &= \left(\frac{\mathrm{d}N}{\mathrm{d}E}\right)_\beta + \left(\frac{\mathrm{d}N}{\mathrm{d}E}\right)_\mathrm{C\nu B} \\ &= \left(\frac{\mathrm{d}N}{\mathrm{d}E}\right)_\beta + \sum_\mathrm{fs} \Gamma'_\nu(^3\mathrm{H}) \cdot \eta \cdot P_\mathrm{fs} \cdot \frac{\mathrm{e}^{-(E_0 - E - E_\mathrm{fs} + m_{\nu_\mathrm{e}})^2 / 2\sigma^2_\mathrm{C\nu B}}}{\sqrt{2\pi\sigma^2_\mathrm{C\nu B}}}.\end{aligned} \tag{5.50}$$

This implementation represents a normalized Gaussian approximation of the CνB signal with a finite standard deviation $\sigma_\mathrm{C\nu B}$ of the order meV, resulting in a much higher numerical stability of the simulation than the sharp line suggested in [FHKŠ11]. The Gaussian is shifted by one neutrino mass m_ν above the final states (E_fs) corrected endpoint E_0. The prefactor $\Gamma'_\nu(^3\mathrm{H})$ is the relic neutrino capture rate on tritium as calculated in [FHKŠ11] (see eq. (5.39)), but in units of s^{-1} instead of yr^{-1}, and

P_{fs} is the probability of each final state to be occupied
With the CνB signal rate being dependent the relic neutrino overdensity η and the not yet fixed standard deviation $\sigma_{\mathrm{C\nu B}}$ we have added two more parameters to the standard four parameter neutrino mass fit [Kle14]. But as we will see, fixing $\sigma_{\mathrm{C\nu B}}$ in advance simplifies and accelerates the fit procedure a lot. This restriction does not have a big influence on the CνB analysis, since the energy resolution of KATRIN is much larger than the meV range of $\sigma_{\mathrm{C\nu B}}$ (see sec. 5.3.4).
Another simplification for the benefit of numerical stability and time saving is the approximation of the discrete FSDs as a Gaussian. Similarly to the Doppler effect (sec. 5.2.2) this simplification is implemented as a convolution, resulting again in a Gaussian (see sec. 5.3.3).
In contrast to the β-decay electrons, radiative corrections for the CνB signal electrons have not yet been computed. However, they are expected to be of the same order as the ones for the β-decay electrons, which means corrections to the rate $< 1\,\%$ [RW83]. Compared to the other assumptions made in this study, this one is certainly of negligible impact.

5.3.1. SSC and KaFit

The implementation of the CνB signal was carried out within the framework of the source and spectrum calculation (SSC) and the KaFit module. SSC, as the name suggests, deals with the calculation and simulation of the spectrum generated by the WGTS. KaFit on the other hand is a set of statistical methods and fit procedures to analyze the simulated SSC spectra and later on the measured KATRIN spectra to extract information about the nonzero neutrino mass.

SSC

To compute the differential and integral spectrum, SSC [Käf12, Höt12, Kle14] needs to emulate the electromagnetic and gasdynamic characteristics of the source, model the response function of the full KATRIN setup and estimate the electron flux at the detector. In contrast to the previously mentioned Kassiopeia module (see sec. 4.3), SSC does not perform particle tracking. Instead, it calculates the spectrum analytically and integrates it numerically, focusing on the source and spectrometer transmission characteristics. This analytic approach is essential for estimating the influence of different parameters on the spectrum; changing one parameter requires a full re-calculation of the spectrum which would consume too much computation time if using particle tracking methods. But of course SSC relies on extensive particle tracking simulations to verify some of its analytical approximations.
Following the existing code, the CνB signal is implemented similarly to the β-decay spectrum in the SSC module, enabling parameter fits to the calculated spectrum with the KaFit module.

KaFit

In order to analyze the SSC-simulated spectrum, one needs a variety of statistical methods implemented in KaFit [Höt12, Kle14]. Extracting information like the neutrino mass or the relic neutrino overdensity out of the simulated (and later on measured) spectrum requires fit routines and advanced statistical methods like the MINUIT [JR75] minimizer or the profile likelihood method. In the context of this

thesis, the MINUIT minimizer combined with MINOS is used to fit the relic neutrino spectra and to extract information like the sensitivity of KATRIN for measuring the CνB.

5.3.2. Statistical methods

This section briefly reviews the statistical methods which formed a base for the studies carried out in the scope of this work. We refer the interested reader to the PhD thesis of M. Kleesiek [Kle14], where a very clear and extensive explanation of all implemented statistical methods is given.

Sensitivity definition

One main task of this thesis was to estimate the sensitivity of KATRIN for constraining potential overdensities of the cosmic neutrino background. Let us first have a look at how KATRIN's sensitivity on the main physics parameter, the neutrino mass, is evaluated. In the KATRIN design report [KAT05], the neutrino mass sensitivity is given as the total (statistical & systematic) uncertainty of reconstructing a neutrino mass value from the data, evaluated for the hypothetical case of a vanishing neutrino mass. The sensitivity of KATRIN for constraining potential overdensities of the cosmic neutrino background is now defined in the same way.
For Gaussian-distributed quantities, the 90 % confidence level equals a 1.645σ interval. Since for the relic neutrino overdensity there exists no such systematic error budget as for the neutrino mass, σ equals the statistical uncertainty, resulting in a statistical sensitivity:

$$S_\eta(90\,\%\text{ C.L.}) = 1.645\sigma_\eta. \tag{5.51}$$

In a previous work, Formaggio et al. [KFM10] used ensemble tests to estimate the uncertainty, but in the context of this thesis, the profile likelihood method will be used to provide an alternative approach. But before turning to this method, the likelihood function for KATRIN needs to be defined.

Likelihood function

The likelihood function L quantifies the likeliness of a specific outcome of an experiment under the assumption that a certain theoretical model is valid:

$$L(\Theta_{\text{theo}}|X_{\text{obs}}) = P(X_{\text{obs}}|\Theta_{\text{theo}}) = \prod_i p_i(X_{\text{obs},i}|\Theta_{\text{theo}}), \tag{5.52}$$

with the set of observations X_{obs} and the set of model parameters Θ_{theo}. The likelihood $L(\Theta_{\text{theo}}|X_{\text{obs}})$ of the model parameters used to describe the observations is equal to the probability $P(X_{\text{obs}}|\Theta_{\text{theo}})$ of making the observation given those parameters as input.
The likelihood function for a KATRIN measurement contains the model parameters given by β-decay theory, extended with respect to the relic neutrino capture signal, and the description of the experiment. For the case of relic neutrinos, the minimum set of model parameters contains the standard four parameters of the neutrino mass

fit (E_0, $m_{\nu e}$, A_S, N_{bg}) as nuisance parameters. The parameter of interest is introduced as fifth parameter: the relic neutrino overdensity η. With these parameters, the likelihood function takes the following form:

$$L(\eta, E_0, m_\nu, A_S, R_{bg}) = \prod_i p_i \left(X_{obs,i} | X_{theo,i}(qU_i, \eta, E_0, m_{\nu_e}, A_S, N_{bg}) \right), \tag{5.53}$$

the index i reflects the retarding potentials qU_i, at which $X_{obs,i}$ events will be observed.

Log likelihood

In practice, it is numerically often more convenient to minimize the negative log likelihood function LL instead of maximizing the likelihood function L:

$$LL(\Theta_{theo}|X_{obs}) = -\log L(\Theta_{theo}|X_{obs}) = -\sum_i \log p_i(X_{obs,i}|\Theta_{theo}). \tag{5.54}$$

Formaggio et al. [KFM10] used ensemble tests to calculate their confidence intervals for the relic neutrino overdensity. To explore an alternative approach, the profile likelihood method was used in this thesis.

Profile likelihood

Though the nuisance parameters are only of secondary interest for obtaining the relic neutrino overdensity sensitivity, they might affect the estimation of the confidence intervals, requiring them to be variable during the fitting process. Fixing the nuisance parameters, for instance to best fit values, would result in an overestimation of the sensitivity, neglecting all correlations between the parameter of interest and the nuisance parameters. A method respecting potential parameter correlations is the profile likelihood method [RLC05]. Defining a function $\pi(\Theta)$ which minimizes LL (or maximizes L) with respect to the nuisance parameters, the profile likelihood function is given by

$$L_P(\Theta) = L(\Theta|\pi(\Theta)). \tag{5.55}$$

A test parameter $\lambda(\Theta)$ can be defined by using the best fit estimate for the parameters $\widehat{\Theta}$ given by the log likelihood fit:

$$\lambda(\Theta) = \frac{L_P(\Theta)}{L_P(\widehat{\Theta})}. \tag{5.56}$$

According to Wilks' theorem [Wil38], $-2\log\lambda$ converges to a χ^2 variable, enabling the extraction of confidence limits: to find the 1σ confidence intervals of a parameter θ, one determines values of θ where $LL(\lambda) = -\log\lambda = 0.5$.

In KaFit, the well-known profile likelihood implementation MINOS is used together with the versatile minimization implementation MINUIT. Both are part of the software package ROOT [ABB+11] and successfully integrated as statistical methods into KATRIN's software module KaFit.

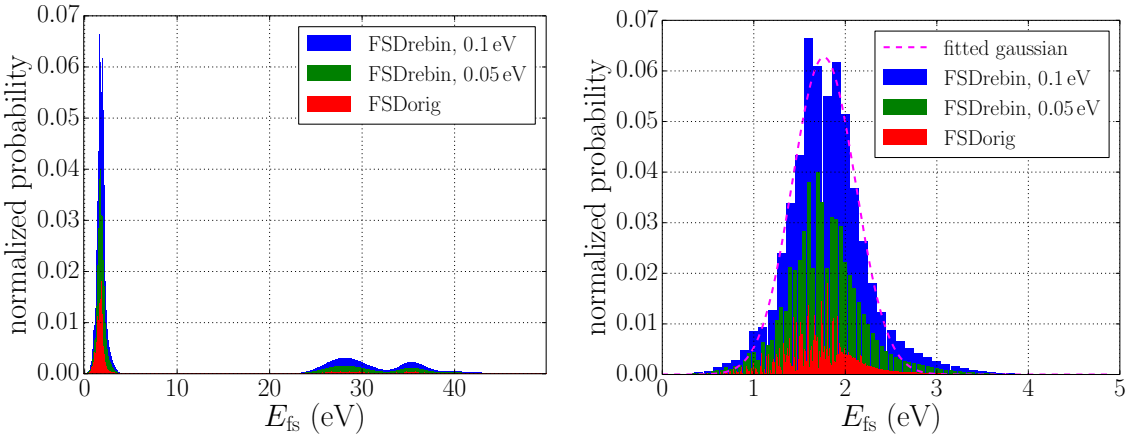

(a) **Full energy range**

(b) **Zoom on the rotational-vibrational excitations of the electronic ground state**

Figure 5.7.: **Final states of the tritium daughter molecules** - Shown is the original distribution (FSDorig) and two rebinned versions (FSDrebin), including the fitted Gaussian.

5.3.3. FSD implementation

As we will see, the implementation of the FSD has a significant influence on the stability and computation time of a fit to a simulated spectrum. Up to now, the only form of the FSD that was introduced is the sum over all final states, weighted by their respective probability. This, in itself, is rather time consuming; furthermore, using the final states in their exact form makes the fitting of such a narrow peak as the CνB signal quite a challenge: in contrast to the continuous β-decay signal, the CνB signal in the differential spectrum is sharp enough to resolve the different final states. This demands a lot of integration steps – since KATRIN measures an integral spectrum – in the region of interest (around the endpoint) to guarantee a minimum numerical stability. Therefore, this procedure is very time consuming.
One possible solution to accelerate the fitting process is using binned FSDs with lower resolution as shown in [Kle14]. In contrast to the original FSDs, the larger bins of this distribution are equally distant, increasing the numeric stability of the fit. As demonstrated in [Kle14], this strategy leads to a large speed-up, namely two orders of magnitude for the reasonable bin width of 100 meV. This width is chosen because it is of the same order as the Doppler broadening (130 meV for $T = 30$ K, see sec. 5.2.2) and therefore does not cause a significant change of the calculated spectrum.

The ultimate optimization, however, is the approximation of the rebinned FSD (bin width 100 meV) through a Gaussian. To do so enables the usage of an analytic function and the implementation of the FSDs through a convolution of this fitted FSD Gaussian (see fig. 5.7b) with the CνB signal, similar to the implementation of

[5] for a simplification of the model, the Gaussian width of the CνB signal is already considered fixed

the Doppler effect:

$$\left(g_{\mathrm{FSD}} \otimes \left(\frac{\mathrm{d}N}{\mathrm{d}E}\right)_{\mathrm{C\nu B}}\right)(E) \propto \int \frac{1}{\sqrt{2\pi\sigma^2_{\mathrm{FSD}}}} \mathrm{e}^{-(E_{\mathrm{fs}}-\mu_{\mathrm{FSD}})^2/2\sigma^2_{\mathrm{FSD}}} \cdot \frac{1}{\sqrt{2\pi\sigma^2_{\mathrm{C\nu B}}}} \mathrm{e}^{-(E+E_{\mathrm{fs}}-(E_0+m_{\nu_{\mathrm{e}}}))^2/2\sigma^2_{\mathrm{C\nu B}}} \,\mathrm{d}E_{\mathrm{fs}} \quad (5.57)$$

with $\mu_{\mathrm{FSD}} = 1.766 \pm 0.009\,\mathrm{eV}$ being the mean excitation energy and $\sigma_{\mathrm{FSD}} = 0.345 \pm 0.023\,\mathrm{eV}$ the standard deviation of the Gaussian used to approximately describe the distribution.
Performing the integration over the final states energy E_{fs} results in a FSD-broadened Gaussian as CνB signal:

$$\left(g_{\mathrm{FSD}} \otimes \left(\frac{\mathrm{d}N}{\mathrm{d}E}\right)_{\mathrm{C\nu B}}\right)(E) = \frac{\Gamma'_{\nu}(^3\mathrm{H})\,\eta\,\xi}{\sqrt{2\pi(\sigma^2_{\mathrm{C\nu B}} + \sigma^2_{\mathrm{FSD}})}} \cdot \mathrm{e}^{(E-(E_0+m_{\nu_{\mathrm{e}}}-\mu_{\mathrm{FSD}}))^2/2(\sigma^2_{\mathrm{C\nu B}}+\sigma^2_{\mathrm{FSD}})^2}, \quad (5.58)$$

with the normalization factor of the Gaussian $\xi = 0.0627 \pm 0.0015$. This implementation of the FSD is crucial for the subsequent analysis (see sec. 5.4), since it enables the usage of the profile likelihood method with MINOS. The MINOS algorithm does not work when using the FSD summation implementation of the CνB signal because this implementation does not provide the necessary numerical stability. Final states with $E_{\mathrm{fs}} > 5\,\mathrm{eV}$ are not considered in the convolved FSD implementation. These final states shift the CνB signal electrons into the β-decay dominated part of the spectrum, equal to a CνB signal loss.

5.3.4. Implementation challenges

During the implementation of the CνB signal into the SSC environment, there were not only the challenges with the FSD. Principal issues like fitting the CνB signal width or simply the form of the CνB signal in the integral spectrum are additional challenges to face.
Treating the CνB signal width $\sigma_{\mathrm{C\nu B}}$ as a free parameter in the fit was found to be unrealistic: the supposed value of $\sigma_{\mathrm{C\nu B}} = 1\,\mathrm{meV}$ (see fig. 5.1, [Fäs14]) is simply not resolvable with the KATRIN energy resolution of 0.93 eV. In fits with variable $\sigma_{\mathrm{C\nu B}}$ (six parameter fits), the reconstructed values for the width were at least one order of magnitude larger than the width used to simulate the measured spectrum (1 meV). This wrong estimation is untouched by using either the rebinned sum FSD implementation or the convolved FSD implementation for the CνB signal. Furthermore, the uncertainties on the CνB signal width estimated by the MINUIT minimization algorithm were always larger than the estimated value itself, which is also an indicator that this parameter simply is not extractable with the present KATRIN setup. The other large issue is the principal effect of the relic neutrino signal on the fit algorithm.
MINUIT calculates the log likelihood for some start values of the parameters, varies the parameters slightly and compares the new LL to the one before. As a result of this comparison, MINUIT tries to estimate new values for the parameters such that the LL decreases. Therefore, the more parameters MINUIT has to deal with, the

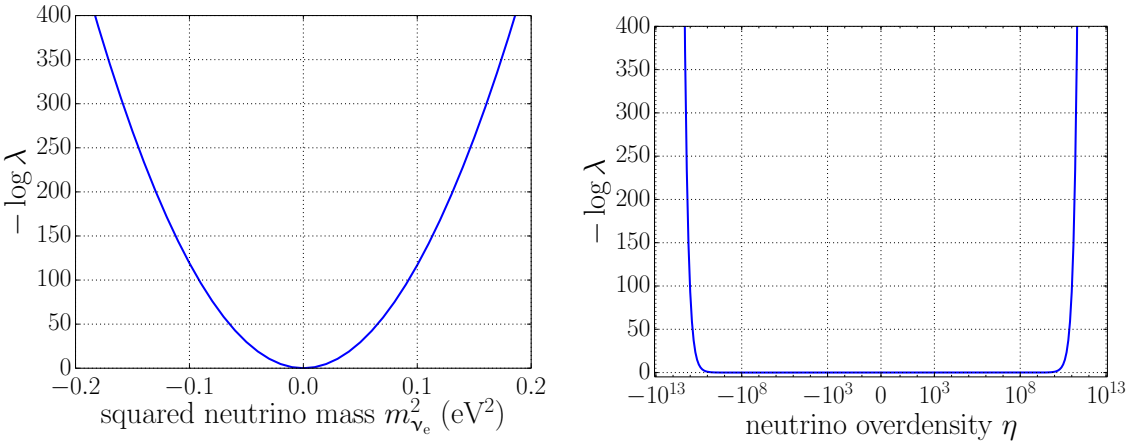

(a) **Log likelihood of neutrino mass**

(b) **Log likelihood of relic neutrino overdensity**

Figure 5.8.: **Log likelihood comparison** - Shown are the log likelihood of $m^2_{\nu_e}$ (left, four parameter fit) and η (right, five parameter fit).

longer the fits take and the more complicated the estimation of the LL minimum becomes. For the standard neutrino mass fit, this is a parameter optimization in four dimensions, while for the CνB overdensity fit there are at least five dimensions (even six dimensions when not fixing $\sigma_{\mathrm{C}\nu\mathrm{B}}$).

Another challenge is the log likelihood (LL) behavior of the overdensity η compared to the log likelihood of the neutrino mass: the neutrino mass LL (fig 5.8a) is a very nice parabola, making it very easy for MINUIT and MINOS to explore the functional shape of the LL around its minimum. In contrary, the overdensity LL (fig. 5.8b) looks like a flat potential well. This complicates the fitting process a lot, because MINUIT has to make small steps for the parameter η around 10^{10} and larger ones towards zero. Thus, for a simulated spectrum with $\eta = 10^{10}$ and a MINUIT start value for η around 0, the first η step better be a large one otherwise it will take a while until MINUIT finds the minimum at 10^{10}. On the other hand, for a simulated spectrum with $\eta = 0$ and a starting parameter value for η of 10^5, MINUIT will take a while until it finds the minimum at 0 because the changes in LL for values lower than 10^{10} are very small, if not negligible. This will become clearer in the next section 5.3.5, when we will see the result of the implementation of the relic neutrino capture signal into SSC: for overdensity values lower than 10^{10} there is simply no signal visible, while for values larger than 10^{11} the signal shows up clearly and visible by eye as the expected shoulder at the end of the β-decay spectrum (see fig. 5.9).

5.3.5. Implementation result

Now that all the challenges are known and solved, it is time to have a look at the hypothetical signal of the relic neutrinos in the KATRIN spectrum. For demonstrating purposes, spectra with different overdensities are simulated and shown in fig. 5.9.
By construction, we expect the relic neutrino capture signal to be broadened by the final states and by the Doppler effect. Since the implementation followed the existing SSC code, the final states are first applied to the CνB signal as a Gaussian convolution (described in sec. 5.3.3) before the FSD-convolved CνB signal is again

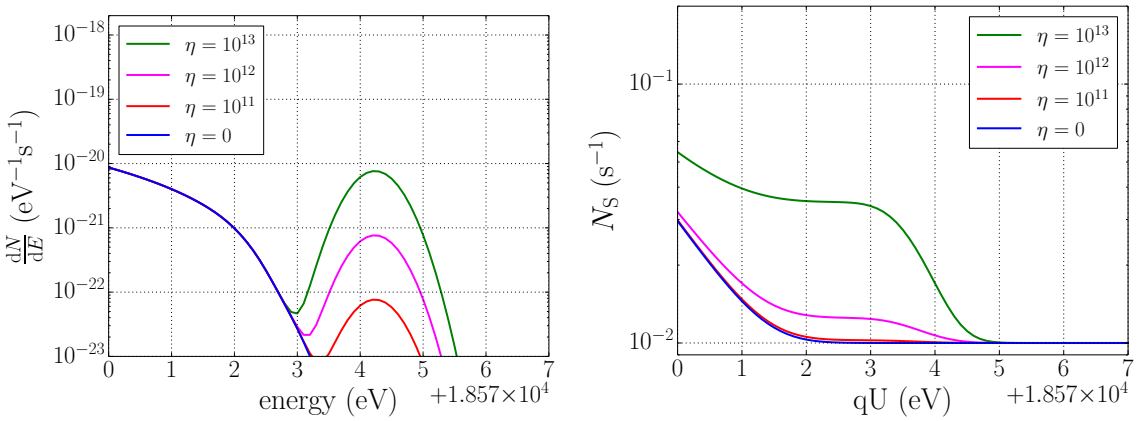

(a) **Differential spectrum** (b) **Integral spectrum**

Figure 5.9.: **Relic neutrino capture spectra on top of the tritium β-decay spectrum** - Spectra are created with the convolved FSD implementation and assuming a neutrino mass of $m_{\nu_e} = 1\,\text{eV}$.

convolved with the Doppler effect function (see sec. 5.2.2). After this convolution process, the broadened CνB signal is integrated in the same way as the β-decay spectrum. Since the differential spectrum contains the CνB signal as a Gaussian like peak, it is obvious to expect the CνB signal to show up as a shoulder in the integral spectrum. Indeed, as can be seen in fig. 5.9, for overdensity values larger than 10^{10}, the integral spectrum contains a distortion at the end of the β-decay spectrum that does look like a shoulder.
Since the width of the relic neutrino capture signal $\sigma_{\text{C}\nu\text{B}}$ is kept fixed at 1 meV from now on, the only parameter left describing the CνB signal is the overdensity η. Taking 1 meV as the width of the relic neutrino capture signal is quite a reasonable choice, supported by the energy distribution of the relic neutrinos shown at the very beginning of this chapter (see fig. 5.1). Consequently, in the following analysis section 5.4, we will be dealing with five parameter optimizations which still are far more complicated to fit than the standard four parameter neutrino mass fit.

5.4. Sensitivity of KATRIN for measuring the cosmic neutrino background

The motivation for implementing the FSD as a Gaussian is the usage of the profile likelihood method to estimate the sensitivity of KATRIN for measuring the CνB: in contrast to Formaggio et al. [KFM10] who use ensemble tests, the estimation of the sensitivity in this thesis is based on the profile likelihood method. The implementation MINOS minimizes η with respect to all other nuisance parameters (neutrino mass, background, amplitude and endpoint energy) and scans the log likelihood for those values of eta where $\Delta LL = 0.5$, in order to construct a confidence interval. To estimate this minimum, MINOS has to calculate the Hesse matrix of the log likelihood. This is where the convolved FSD implementation is needed: the functional shape of the log likelihood using the summed FSD implementation is not smooth enough to perform this kind of analysis.
The sensitivity is estimated as a factor times the upper MINOS error (compare eq. (5.51)), which is the value of η resulting in a log likelihood of 0.5. With this

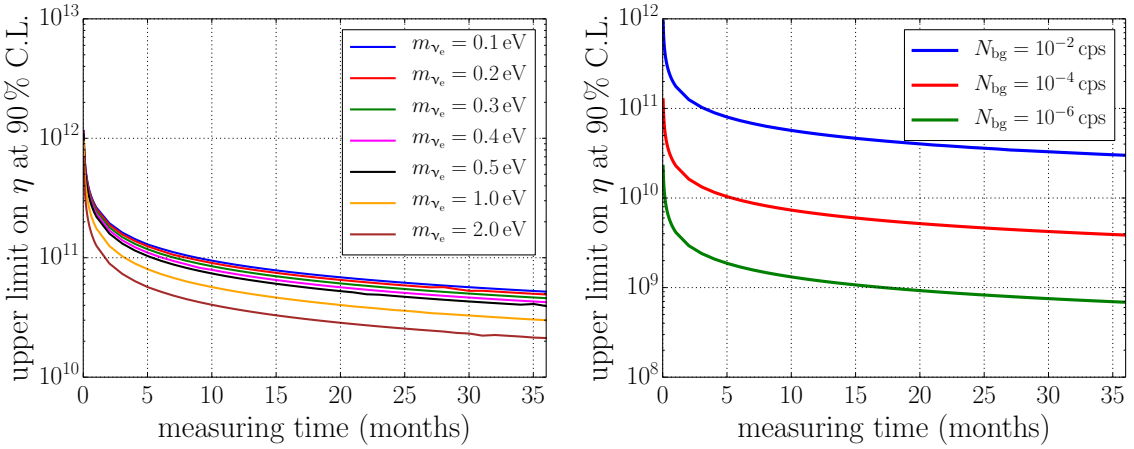

(a) **Neutrino mass dependence** (b) **Background dependence**

Figure 5.10.: **Upper limit on the relic neutrino overdensity depending on background and neutrino mass**

method, several effects on the sensitivity of KATRIN for measuring the CνB are investigated in the next sections. First, the limit on the CνB overdensity is derived for several hypothetical neutrino masses and different background rates (sec. 5.4.1). Then the effect of using measuring time distributions[6] (MTD) different from the ones described in the KATRIN design report [KAT05] and sinusoidal high voltage fluctuations as potential systematic uncertainties for the relic neutrino overdensity are investigated. The section closes with a discussion of the found results in sec. 5.4.4.

5.4.1. Sensitivity for the cosmic neutrino background overdensity

This section shows the limits KATRIN can set on the CνB overdensity after three full years of measurement by using the profile likelihood method. First the effect of different neutrino masses and background rates is studied, before the optimization of the sensitivity by changing the measuring time distribution (MTD) is investigated.

Neutrino mass and background

As stated in sec. 2.4, yet only upper limits (about 2 eV) on the neutrino mass exist. Therefore, the relic neutrino overdensity sensitivity is estimated for several assumed neutrino mass values, in the range from 0.1 eV to 2 eV. The corresponding upper limit KATRIN can set at 90 % C.L. is shown in fig. 5.10a (for the KATRIN design report [KAT05] anticipated background rate of 10^{-2} cps). From the signature of the relic neutrinos in the KATRIN spectrum, one expects stronger limits for larger neutrino masses: the larger the neutrino mass, the longer the shoulder of the relic neutrino signal. This is confirmed in fig. 5.10a: the limit is strongest for the largest neutrino mass of 2 eV, namely $\eta = 2.1 \cdot 10^{10}$ at 90 % C.L. after three years of data taking. Furthermore, the limit gets stronger with measurement time, being the result of increased statistics.
The background rate at KATRIN has the largest investigated impact on the limit

[6] A measuring time distribution is a set of measurement configurations, defining the amount of effective measuring time invested at a specific retarding potential qU.

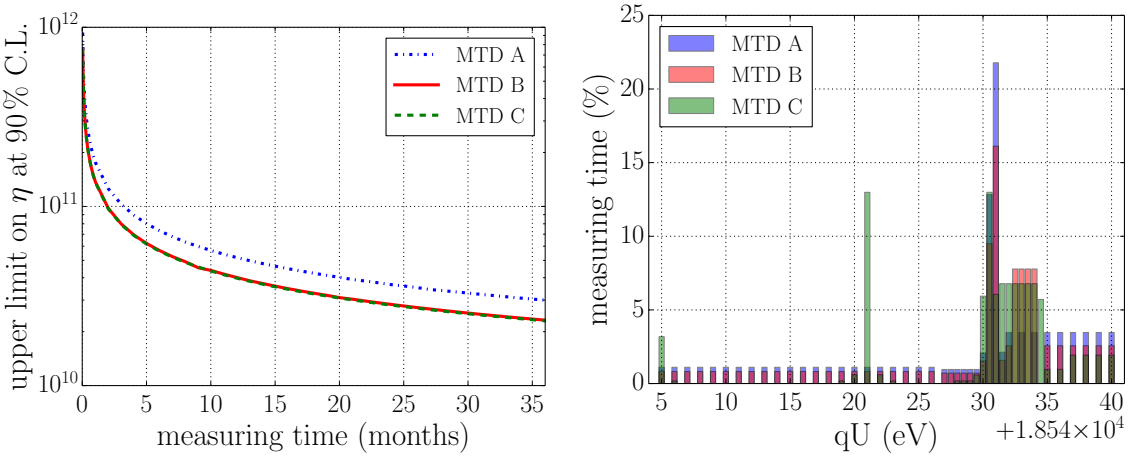

(a) **MTD dependence**

(b) **Used MTD** - MTD A is from [KAT05], MTD B is derived from MTD A and MTD C is derived from [Kle14].

Figure 5.11.: **Sensitivity of KATRIN for the relic neutrino overdensity depending on the used MTD**

on the relic neutrino overdensity. Lowering the background rate from the KATRIN design report value [KAT05] 10^{-2} cps to values of 10^{-4} cps or even 10^{-6} cps improves the limit significantly by two orders of magnitude: from $3.0 \cdot 10^{10}$ to $6.8 \cdot 10^{8}$ at 90 % C.L. In fig. 5.10b, the sensitivity gain with increasing measuring time for the different background rates is shown for a neutrino mass of 1 eV. The strong dependence of the relic neutrino sensitivity on the background rate is easily understood: the lower the background rate, the more prominent is the relic neutrino signal.

Measuring time

When comparing the KATRIN design report MTD (MTD A of fig. 5.11b) to the spectrum created with relic neutrinos (see fig. 5.9), one notes that the measuring time can be optimized to increase the sensitivity for the relic neutrino signal. Therefore, the measuring time in the region between −18572 V and −18574 V is increased and the retarding voltage steps are set to 0.5 V (MTD B of fig. 5.11b). As a third option, the neutrino mass optimized MTD found by M. Kleesiek in [Kle14] was modified to account for the relic neutrino signal by increasing the measuring time similar to MTD B.
Though the MTD modifications are made by hand and represent just a proof-of-principle test, the effect is quite impressive: the limit on the relic neutrino overdensity can be improved from $3.0 \cdot 10^{10}$ to $2.3 \cdot 10^{10}$ at 90 % C.L. (for both, MTD B and C). This improvement is due to the refined measuring time in the relic neutrino signal region, causing more sampling points for the fit algorithm in the region of interest.

5.4.2. Sensitivity for the neutrino mass

Looking at fig. 5.9, one expects that a large relic neutrino overdensity also influences the neutrino mass sensitivity of KATRIN: the relic neutrino shoulder for overdensity values larger than 10^{11} is a very strong distortion to the β-decay spectrum. A CνB overdensity that large would be expected to increase the sensitivity of KATRIN for

Table 5.2.: **Reevaluated neutrino mass sensitivity** - Neutrino mass sensitivity after three years of data taking with large relic neutrino overdensities. Shown are the 90 % C.L. statistical uncertainty and total limits (including systematic uncertainty) on the neutrino mass.

η	90 % C.L. σ_{stat} (eV)	90 % C.L. limit (eV)
10^{14}	0.003	0.167
10^{13}	0.005	0.167
0	0.164	0.197

measuring the neutrino mass. To study this effect, several assumed overdensity values were used to estimate the neutrino mass sensitivity of KATRIN, again with the profile likelihood method.
The KATRIN design report neutrino mass limit [KAT05], based on three years of data, is 0.2 eV at 90 % C.L., while M. Kleesiek proposed [Kle14] that this sensitivity can be slightly improved by using a MCMC[7] optimized MTD. Using the KATRIN design report MTD and overdensity values of $\eta = 10^{13}$ and 10^{14}, the neutrino mass sensitivity of KATRIN was reevaluated; the results are shown in tab. 5.2. The relic neutrino signal thus helps increasing the neutrino mass sensitivity by lowering the statistical uncertainty on the neutrino mass, so the dominating uncertainty becomes the systematic uncertainty. Potential effects of such large relic neutrino overdensities on the neutrino mass systematic uncertainties have not been reevaluated in this thesis; the systematic uncertainty is kept fixed at the design report value of $\sigma_{\mathrm{sys}}(m^2_{\bar{\nu}_e}) = 0.017\,\mathrm{eV}^2$. The total mass sensitivity in tab. 5.2 becomes clearly dominated by the systematic uncertainty since it is the quadratic sum of the statistical and systematic uncertainty (see sec. 5.3.2).

5.4.3. Cosmic neutrino background overdensity systematics

The neutrino mass determination at KATRIN is affected by several systematic effects. Variations of the energy scale in the form of high voltage fluctuations of the retarding potential σ_{qU} can be seen as a very critical systematic uncertainty for the neutrino mass [RK88], as they result in a negative shift of the squared neutrino mass if not detected. The shift is caused by the smearing of the transmission function resulting from the high voltage fluctuations (see fig. 3.3).
To investigate a potential systematic shift of the relic neutrino overdensity due to high voltage fluctuations, again the profile likelihood method was used: indeed, fitting to a spectrum generated with a sinusoidal high voltage fluctuation (given by eq. (3.14)) reveals a shift of η. The long-term monitoring goal for high voltage stability and reproducibility is a monitoring sensitivity of 0.06 V [Thü07]. However, short-term sinusoidal fluctuations may not be detectable. In the following, these sinusoidal high voltage fluctuations are conservatively assumed to exhibit an amplitude of 0.1 V. For a simulated relic neutrino overdensity $\eta = 10^{11}$, high voltage fluctuations of 0.1 V lead to an estimated best fit value of $\widehat{\eta} = 1.014 \cdot 10^{11}$, resulting in a shift of $1.4 \cdot 10^9$. This shift can be seen as a systematic uncertainty because it is

[7] Markov Chain Monte Carlo

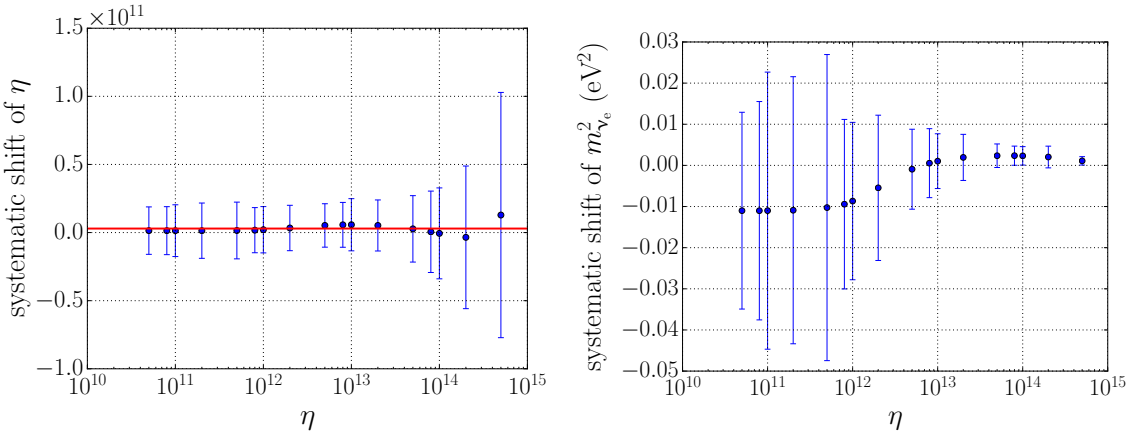

(a) **Systematic shift of the best fit relic neutrino overdensity caused by high voltage fluctuations**

(b) **Systematic shift of the best fit neutrino mass caused by high voltage fluctuations**

Figure 5.12.: **Systematic shifts caused by high voltage fluctuations**

always in the same direction, similar to systematics leading to a negative neutrino mass square.
The relic neutrino signal starts to affect the spectrum significantly for overdensity values between $\eta = 10^{10}$ and $\eta = 10^{12}$. In this range, the estimated systematic shift of the overdensity as well as the negative shift of the neutrino mass is constant, which is totally expected. But for larger overdensities, the relic neutrino shoulder starts to dominate the spectrum around the endpoint, complicating or even hindering the neutrino mass extraction. The neutrino mass extraction in turn affects the relic neutrino overdensity estimation, leading to different overdensity shifts as shown in fig. 5.12. Fig. 5.12b reveals that there is an overdensity value for which the negative neutrino mass squared shift caused by $\sigma_{\mathrm{qU}} = 0.1\,\mathrm{V}$ vanishes (somewhere around $\eta = 7 \cdot 10^{12}$). This means that overdensity values in just this region would make the neutrino mass determination robust against high voltage fluctuations.
Fitting a constant to the systematic shift values of fig. 5.12a leads to the following average relic neutrino overdensity shift:

$$\sigma_\eta = (2.94 \pm 4.87) \cdot 10^9. \tag{5.59}$$

The uncertainty of this mean value is large, predominantly caused by the large numerical errors at $\eta > 10^{14}$.

The investigation of the high voltage fluctuations effect on η shows that the standard neutrino systematics (four parameter fit) are not so easily transferable to the overdensity systematics (five parameter fit).

5.4.4. Discussion of the results

Let us begin with a critical evaluation of the results of this chapter by comparing them to previous work done on this topic. Formaggio et al. [KFM10] also estimated the sensitivity of KATRIN for constraining the CνB. Instead of the profile likelihood method as used in the present thesis, they used ensemble tests and found that KATRIN will be able to set a 90 % C.L. upper limit on the relic neutrino overdensity

of $2 \cdot 10^9$. This value is one order of magnitude below the values obtained in this thesis ($2.1 \cdot 10^{10}$ up to $5.2 \cdot 10^{10}$ at 90 % C.L., for neutrino masses between 0.1 eV and 2 eV). An immediate comparison of the two models, however, does not seem appropriate for the following reasons:

- The amount of tritium on which the estimate by Formaggio et al. is based differs significantly from the one used in this thesis. They state an effective column density, which accounts for the inelastic scattering probability P of the signal electrons in the source, of $\rho d_{\text{eff}} = P \cdot \rho d = 3.58 \cdot 10^{17}\,\text{cm}^{-2}$. From this effective column density they calculate an effective number of tritium molecules seen by the detector of

$$N_{\text{eff}} = A_{\text{S}} \cdot \epsilon_{\text{T}} \cdot \frac{\Omega}{2\pi} \cdot P \cdot \rho d = 6.64 \cdot 10^{18}, \tag{5.60}$$

  with a source area of $A_{\text{S}} = 52.65\,\text{cm}^2$, a tritium purity of $\epsilon_{\text{T}} = 0.95$ and a solid angle Ω. This effective number of tritium molecules is equivalent to an effective tritium mass of $M_{\text{eff}} = 66.5\,\mu\text{g}$. Comparing these values and the respective equations to the ones stated in this thesis in sec. 3.2.1 ($n_{\text{eff}}(\text{T}_2) = 4.66 \cdot 10^{18}$, $m_{\text{eff}} = 46.6\,\mu\text{g}$) reveals a potential origin of the mismatch: in the thesis at hand, the solid angle Ω is normalized to 4π accounting for isotropic emission, whereas Formaggio et al. use a normalization to 2π (corresponding only to the forward section of the tritium source). Scaling $m_{\text{eff}} = 46.6\,\mu\text{g}$ with $P_0 = 41.33\,\%$ yields an effective tritium mass scaled to the fraction of electrons not undergoing inelastic scattering of $m'_{\text{eff}} = 20\,\mu\text{g}$.

- The implementation of the scattering probability of the electrons inside the source is simplified by Formaggio et al.: as stated above, they use an effective column density to account for inelastic electron scattering in the source by a scaling factor. Apart from also taking into account multiple scattering via the response function (see eqs. (3.15),(5.49)), our probability for the electrons exiting the source without undergoing any inelastic scattering process differs from the value of Formaggio et al: we use $P_0 = 41.33\,\%$ while using the design report column density gives $P = \rho d_{\text{eff}}/\rho d = 71.6\,\%$.

- A minor issue is the lack of any detection efficiency in the model of Formaggio et al. We use an efficiency of $\varepsilon = 0.9$ [KAT05] to take into account electron backscattering at the detector surface.

- As discussed in sec. 5.3.4, the width of the CνB signal has major influence. In this thesis, this value was kept fixed at $\sigma_{\text{C}\nu\text{B}} = 1\,\text{meV}$, which seems to be a realistic value comparing with fig. 5.1. By contrast, Formaggio et al. state that they chose the width "to be smaller than any characteristic resolution present in the experiment, but sufficiently large to be reliably integrable by numerical methods" [KFM10], without explicitly stating the value of $\sigma_{\text{C}\nu\text{B}}$.

- For reasons of completeness, it has to be noted, that the final state effect is also treated slightly differently. In this thesis, the FSDs are approximated by a Gaussian with mean 1.766 eV and a standard deviation of 0.345 eV (see sec. 5.3.3), while Formaggio et al state a mean of 1.7 eV with an inherent broadening of 0.36 eV for their distribution.

- This work normalizes the CνB signal as stated in eq. (5.50), while it is not clear which (if any) normalization was employed by [KFM10].

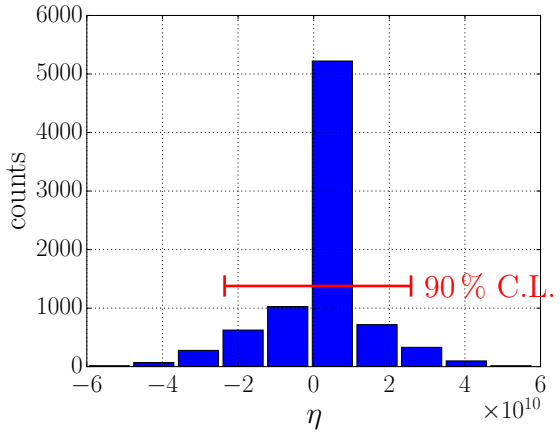

Figure 5.13.: **Ensemble test limit** - 90 % C.L.: $2.1 \cdot 10^{10}$, calculated from the standard deviation of $1.3 \cdot 10^{10}$ and the mean of $5 \cdot 10^{7}$. In total, 8400 fits with an assumed neutrino mass of 1 eV were performed.

- Performing ensemble tests with the model implemented in this thesis supports the already calculated limit from the profile likelihood method. For 8400 fits with an assumed neutrino mass of 1 eV, the 90 % confidence limit as calculated with eq. (5.51) is $2.1 \cdot 10^{10}$ (the mean of $5 \cdot 10^{7}$ can be neglected; compare fig. 5.13). One fit lasted about 700 s in average; this and the similarity of the profile likelihood and the ensemble test method sensitivity is the justification for using the profile likelihood method to calculate the sensitivity in dependence of the MTD.

All of the above items indicate that the two investigations cannot be compared on an equal footing, which is why we refrain from performing a quantitative comparison of the two analyses here.

5.5. Summary

Similar to the CMB, Big Bang theory postulates the existence of a cosmic neutrino background, CνB which decoupled 1 s after the Big Bang and today has an average temperature of 1.95 K and an average particle density of $56\,\mathrm{cm}^{-3}$ per flavor. There is compelling evidence for non-zero neutrino masses from a wealth of neutrino oscillation experiments. These non-vanishing masses would allow neutrinos from the CνB to cluster due to its low present-day temperature, resulting in a local relic neutrino overdensity. There are several proposals for this clustering – one is the clustering on CDM potentials – but since the relic neutrinos remain undetected as yet, none of them can be tested so far.
One of the experiments which can at least set a limit on the relic neutrino overdensity is the KATRIN experiment, which has the goal of measuring the neutrino mass with unprecedented sensitivity by high resolution β-decay spectroscopy. The tritium gas employed by KATRIN as a high-activity β-decay source can also serve as a target for capturing relic neutrinos through induced β-decay, resulting in a sharp line located one neutrino mass above the endpoint of the β-decay spectrum.
In the model of the differential spectrum, the relic neutrino signal is implemented as a Gaussian with a width of 1 meV, located one neutrino mass above the endpoint energy. The CνB signal is broadened and shifted towards lower energies by the

Doppler effect and the final states of the tritium daughter molecule. There are two implementations of the signal combined with the FSD: one as summation over all discrete final states which is rather time consuming, and one as approximation of the final states by a Gaussian, resulting in an analytical convolution. The latter one is an essential prerequisite for the usage of the profile likelihood method (with MINOS), because it can be readily differentiated in MINOS.
Since KATRIN will measure an integral spectrum, the CνB signal results in a shoulder, terminating one neutrino mass above the endpoint and the height reflecting the local relic neutrino overdensity.

Using the profile likelihood method, the sensitivity of KATRIN for constraining the cosmic neutrino background can be estimated. It is found to be dependent on the neutrino mass and strongly dependent on the background rate. A larger neutrino mass results in a better sensitivity, because the shoulder of the relic neutrino signal in the integral KATRIN spectrum is broadened by larger neutrino masses and becomes more pronounced. For the measuring time distribution originally proposed in the KATRIN design report [KAT05] and the targeted background rate of 10^{-2} cps, the upper limit KATRIN can set after three years of measuring time is in the range of $2.1 \cdot 10^{10}$ to $5.2 \cdot 10^{10}$ at 90 % C.L. for neutrino masses between 2 eV and 0.1 eV respectively.

For normal distributed parameters with a parabola-like log likelihood, the profile likelihood converges to χ^2, and profile likelihood and ensemble test should provide equivalent confidence intervals. Using ensemble tests to estimate the sensitivity in dependency of the measuring time – as done in this thesis – would be highly inefficient with regard to computing time. Since the resulting uncertainty on the overdensity limit decreases with increasing statistics, each point would require about 10000 fits to achieve a satisfying accuracy. The challenging likelihood shape of the overdensity is a result of the small CνB signal width (sec. 5.3.4) and its broadening caused by the Doppler effect and final state effects. In the present chapter it was shown that KATRIN can constrain the local relic neutrino overdensity with a sensitivity between $5.2 \cdot 10^{10}$ and $2.1 \cdot 10^{10}$ at 90 % C.L., for neutrino masses between 0.1 eV and 2 eV. This limit is weaker than the one found previously by Formaggio et al. [KFM10] but is not immediately comparable, as discussed in sec. 5.4.4.

The relic neutrino overdensity limit obtainable with KATRIN has the potential to rule out several speculative cosmological models. One of them is the GZK effect[8] on relic neutrinos, which requires CνB overdensities larger than 10^{13} [HM05] to cause a cutoff in the spectra of high-energy protons or nuclei.

Investigating possibilities to increase the CνB sensitivity of KATRIN revealed the strong dependence on the background rate N_{bg}: lowering N_{bg} from the design report value of 10^{-2} cps to 10^{-4} cps or even 10^{-6} cps results in an up to two orders of magnitude better CνB sensitivity. Though achieving such low background rates – even orders of magnitude below the design value – will likely not be possible with KATRIN in the near future, this work might provide a motivation for future relic neutrino dedicated experiments to achieve low background.
Another possibility to achieve better relic neutrino sensitivity is using a different

[8] Greisen-Zatsepin-Kuzmin effect: potential explanation for the cutoff of the cosmic ray spectra around $5 \cdot 10^{19}$ eV

measuring time distribution (MTD) as proposed in [Kle14]. Though this optimization is not fully completed yet, promising initial results have been obtained in the thesis at hand. The optimization of the MTD is done in the CνB signal region in the integral spectrum by increasing the measuring time and using 0.5 V steps instead of 1 V steps. For the original design report MTD and the neutrino mass optimized MTD found by M. Kleesiek [Kle14], this kind of optimization leads to a sensitivity increase from $3.0 \cdot 10^{10}$ to $2.3 \cdot 10^{10}$ at 90 % C.L. This may not be a large improvement, but there is potential for further tightening of the achievable constraint by further optimizing the MTD for the CνB measurement.

On a side node, large CνB overdensity values could lead to an improvement of the neutrino mass sensitivity of KATRIN. Hypothetical values of $\eta = 10^{13}$ and 10^{14} reduce the statistical uncertainty on the neutrino mass determination enormously: down to 0.005 eV for $\eta = 10^{13}$ and 0.003 eV for $\eta = 10^{14}$. However, this large increase in statistical sensitivity is useless if the systematic uncertainty stays untouched at $\sigma_{\mathrm{sys}}(m^2_{\bar{\nu}_e}) = 0.017\,\mathrm{eV}^2$, because the total sensitivity is then dominated by the systematic sensitivity. But since such large overdensity values are rather unlikely, the neutrino mass sensitivity of KATRIN will be likely not be affected by η.

As an example for systematic uncertainties of the relic neutrino overdensity, sinusoidal high voltage fluctuations are considered. High voltage fluctuations of 0.1 V amplitude, when unaccounted for, are found to cause a constant negative neutrino mass shift and a constant positive overdensity shift for overdensities between 10^{10} and 10^{12}. For overdensity values around 10^{13}, the relic neutrino signal seems to coincidentally cancel the negative neutrino mass shift caused by the high voltage fluctuations. Larger overdensities even may lead to difficulties in the neutrino mass estimation due to the relic neutrino signal dominating the tail of the tritium spectrum.

CHAPTER 6

CONCLUSIONS & OUTLOOK

The KArlsruhe TRItium Neutrino (KATRIN) experiment, currently under construction at KIT, aims to determine the absolute value of the neutrino mass with an unprecedented sensitivity of 200 meV. This new level in neutrino mass sensitivity requires due to an ultra-luminous tritium source combined with high-precision β-decay spectroscopy.

With its unique high-luminosity β-decay source, the KATRIN experiment provides not only the possibility to determine the neutrino mass but also search for the yet unmeasured cosmic neutrino background (CνB), the neutrino pendant to the cosmic microwave background (CMB). A crucial quantity for the search for the CνB via induced tritium β-decay is the number of tritium molecules in the source, respectively the tritium column density. Monitoring of this parameter is enabled by the source analysis tool "Rear Section" by providing an electron beam with characteristics emulating the tritium β-decay electrons. Both for the neutrino mass determination as KATRIN's main scientific goal and for constraining the CνB, the systematics of the Rear Section need to be well understood. Therefore, in this work, the Rear Section with its versatile photo-electron source (E-gun) was implemented into the most recent version of the KATRIN particle tracking simulation software Kassiopeia.

One example of a tangible outcome of this thesis is the exact positioning of the optical fibers of the E-gun due to the optimum starting positions of the electrons. With these fiber positions, the Rear Section will exceed its design requirements in terms of angular resolution and energy spread. Monitoring of the column density in the WGTS requires the E-gun to achieve electron pitch angles up to the largest transmissible angle of $\theta = 51^\circ$ in the WGTS. The best angular resolution for θ is obtained when turning the E-gun to the maximum pitch angle of 15°, a plate potential difference of 2600 V and using fiber ID 3: the angular spread with $\sigma_{\theta_{\mathrm{WGTS}}} \approx 0.8^\circ$ is then way below the required 4°. With this high angular resolution, the Rear Section will provide the necessary precision to monitor the tritium column density.

Precise knowledge of the column density is of great importance not only for the neutrino mass determination but also for the search for the CνB. The expected CνB signal was successfully modeled based on the software packages SSC and KaFit via induced tritium β-decay. Implementation of the model introduces at least one

additional parameter, the relic neutrino overdensity: the non-zero mass of neutrinos allows for clustering of relic neutrinos due to their gravitational interaction. Several proposals for the clustering mechanism have been made, one of them the clustering on cold dark matter (CDM) [RW04]. So far these remain speculative and a way to either verify or falsify any of them is still missing. In contrast to previous studies which used ensemble tests, it was decided to concentrate on the profile likelihood method to estimate the sensitivity of KATRIN for measuring CνB. Using the profile likelihood method requires an analytical approach to the final state distribution (FSD) of the tritium daughter molecules. With the profile likelihood method, the upper limit KATRIN can set on the local CνB overdensity was found to be in the range of $2.1 \cdot 10^{10}$ to $5.2 \cdot 10^{10}$ at 90 % C.L. for neutrino masses in the range of 2 eV to 0.1 eV respectively. This limit is weaker than the one found previously by Formaggio et al. [KFM10] but is in fact not immediately comparable, as discussed in sec. 5.4.4.

Furthermore, several possibilities to increase this sensitivity have been investigated. One is optimizing the measuring time distribution (MTD), which was found to be in principle possible but only yielding a marginal effect so far. Much larger sensitivity can be achieved by reducing the background. In contrast to modifying the MTD, a reduction of the background within the very near future by several orders of magnitude does not seem realistic. Large relic neutrino overdensities would lead to an increase of the neutrino mass sensitivity of KATRIN, from 0.197 eV with an already optimized MTD [Kle14] to 0.167 eV for overdensity values of 10^{13} or 10^{14}. For such large overdensity values, the systematics in neutrino mass estimation clearly dominate the statistics. Finally, the systematic uncertainty on the relic neutrino overdensity was exemplarily estimated by high voltage fluctuations and found to be of the order of 10^9.

Though there exist several more radical possibilities to increase the relic neutrino sensitivity of KATRIN-like experiments such that a detection of the CνB comes within reach [FHKŠ13], none of them seems feasible at the moment. Future relic neutrino experiments may not only look for a better energy resolution but also for lower background rates. Furthermore, the usage of atomic instead of molecular gaseous tritium would lead to a sensitivity increase [BBC$^+$13]: weakly binding the tritium atom to a nearly inert chemical substrate would result in much smaller broadening of the relic neutrino signal compared to the final state effects caused by the tritium daughter molecules. The relic neutrino sensitivity directly scales with the amount of tritium; however, increasing the tritium density at KATRIN results in an increased scattering probability for the signal electrons and therefore does not improve the detection efficiency.

The Rear Section's electron gun will be shipped to the Karlsruhe Institute for Technology (KIT) in the near future and installed at KATRIN experiment. The findings of this thesis helped to improve the final electron gun design to ensure it will fulfill its monitoring requirements. Thereby, the Rear Section helps the KATRIN experiment to reach the unprecedented neutrino mass sensitivity of 200 meV to further constrain neutrino parameters.

APPENDIX A

REAR SECTION GEOMETRY DEFINITIONS OF COMPONENTS

A.1. Beam tube geometry definition

```
<!-- XML geometry for the rearsection ground electrode -->
<geometry>
    <!-- shape parameters for the rs_ground electrode geometry -->
    <global_define name="rs_ground_dps1r-flange_reference" value="-4.73"/>
    <define name="rs_ground_electrode_z1" value="0."/>
    <global_define name="rs_ground_electrode_z2" value="2.067"/>
    <define name="rs_ground_electrode_z3" value="4.306"/>
    <define name="rs_ground_electrode_z4" value="4.381"/>
    <define name="rs_ground_electrode_z5" value="4.394"/>
    <define name="rs_ground_electrode_z6" value="4.462"/>
    <define name="rs_ground_electrode_z7" value="4.731"/>
    <define name="rs_ground_electrode_z8" value="{[rs_ground_electrode_z7]+0.24621468}"
        />
    <define name="rs_ground_electrode_z9" value="5.73"/>
    <define name="rs_ground_electrode_r1" value="0.075"/>
    <define name="rs_ground_electrode_r2" value="0.03"/>
    <define name="rs_ground_electrode_r3" value="0.075"/>
    <define name="rs_ground_electrode_r4" value="0.0025"/>
    <define name="rs_ground_electrode_r5" value="0.125"/>
    <define name="rs_ground_electrode_r6" value="0.045"/>

    <!-- global meshing parameters for the rs_ground geometry -->
    <define name="rs_ground_curvature_n" value="5"/>
    <define name="rs_ground_opening_curvature_n" value="9"/>
    <define name="rs_ground_arc_count" value="96"/>
    <define name="rs_ground_mesh_scale" value="5"/>
    <define name="rs_ground_mesh_power" value="1.5"/>

    <!-- ground electrode surface -->
    <!-- reference point is back z value -->
    <tag name="all_tag" name="rs_electrode_tag" name="rs_axial_electrode_tag" name="
        rs_ground_electrode_tag">
        <rotated_poly_line_surface name="rs_ground_electrode_surface" rotated_mesh_count
            ="[rs_ground_arc_count]">
            <poly_line>
```

```
33          <start_point x="{[rs_ground_electrode_z1]+ [rs_ground_dps1r-
                flange_reference]}" y="0."/>
34          <next_line
35              x="{[rs_ground_electrode_z1]+ [rs_ground_dps1r-flange_reference]}"
36              y="{[rs_ground_electrode_r1]}"
37              line_mesh_count="{3*[rs_ground_mesh_scale]}"
38              line_mesh_power="{1}"
39          />
40          <next_line
41              x="{[rs_ground_electrode_z2]+ [rs_ground_dps1r-flange_reference]}"
42              y="{[rs_ground_electrode_r1]}"
43              line_mesh_count="{20*[rs_ground_mesh_scale]}"
44              line_mesh_power="{[rs_ground_mesh_power]}"
45          />
46          <next_line
47              x="{[rs_ground_electrode_z2]+ [rs_ground_dps1r-flange_reference]}"
48              y="{[rs_ground_electrode_r2]}"
49              line_mesh_count="{1*[rs_ground_mesh_scale]}"
50              line_mesh_power="{[rs_ground_mesh_power]}"
51          />
52          <next_line
53              x="{[rs_ground_electrode_z3]+ [rs_ground_dps1r-flange_reference]}"
54              y="{[rs_ground_electrode_r2]}"
55              line_mesh_count="{30*[rs_ground_mesh_scale]}"
56              line_mesh_power="{[rs_ground_mesh_power]}"
57          />
58          <next_line
59              x="{[rs_ground_electrode_z3]+ [rs_ground_dps1r-flange_reference]}"
60              y="{[rs_ground_electrode_r3]}"
61              line_mesh_count="{1*[rs_ground_mesh_scale]}"
62              line_mesh_power="{[rs_ground_mesh_power]}"
63          />
64          <next_line
65              x="{[rs_ground_electrode_z4]+ [rs_ground_dps1r-flange_reference]}"
66              y="{[rs_ground_electrode_r3]}"
67              line_mesh_count="{1*[rs_ground_mesh_scale]}"
68              line_mesh_power="{[rs_ground_mesh_power]}"
69          />
70          <next_line
71              x="{[rs_ground_electrode_z4]+ [rs_ground_dps1r-flange_reference]}"
72              y="{[rs_ground_electrode_r4]}"
73              line_mesh_count="{2*[rs_ground_mesh_scale]}"
74              line_mesh_power="{[rs_ground_mesh_power]}"
75          />
76          <next_line
77              x="{[rs_ground_electrode_z5]+ [rs_ground_dps1r-flange_reference]}"
78              y="{[rs_ground_electrode_r4]}"
79              line_mesh_count="{2*[rs_ground_mesh_scale]}"
80              line_mesh_power="{[rs_ground_mesh_power]}"
81          />
82          <next_line
83              x="{[rs_ground_electrode_z5]+ [rs_ground_dps1r-flange_reference]}"
84              y="{[rs_ground_electrode_r3]}"
85              line_mesh_count="{2*[rs_ground_mesh_scale]}"
86              line_mesh_power="{[rs_ground_mesh_power]}"
87          />
88          <next_line
89              x="{[rs_ground_electrode_z6]+ [rs_ground_dps1r-flange_reference]}"
90              y="{[rs_ground_electrode_r5]}"
```

```
91                  line_mesh_count="{1*[rs_ground_mesh_scale]}"
92                  line_mesh_power="{[rs_ground_mesh_power]}"
93              />
94              <next_line
95                  x="{[rs_ground_electrode_z7]+ [rs_ground_dps1r-flange_reference]}"
96                  y="{[rs_ground_electrode_r5]}"
97                  line_mesh_count="{2*[rs_ground_mesh_scale]}"
98                  line_mesh_power="{[rs_ground_mesh_power]}"
99              />
100             <next_line
101                 x="{[rs_ground_electrode_z8]+ [rs_ground_dps1r-flange_reference]}"
102                 y="{[rs_ground_electrode_r6]}"
103                 line_mesh_count="{2*[rs_ground_mesh_scale]}"
104                 line_mesh_power="{[rs_ground_mesh_power]}"
105             />
106             <next_line
107                 x="{[rs_ground_electrode_z9]+ [rs_ground_dps1r-flange_reference]}"
108                 y="{[rs_ground_electrode_r6]}"
109                 line_mesh_count="{6*[rs_ground_mesh_scale]}"
110                 line_mesh_power="{[rs_ground_mesh_power]}"
111             />
112             <next_line
113                 x="{[rs_ground_electrode_z9]+ [rs_ground_dps1r-flange_reference]}"
114                 y="{0.000001}"
115                 line_mesh_count="{3*[rs_ground_mesh_scale]}"
116                 line_mesh_power="{1}"
117             />
118         </poly_line>
119     </rotated_poly_line_surface>
120 </tag>
121
122 <!-- rearsection diaphragm -->
123 <tag name="all_tag" name="rs_diaphragm_tag" name="rs_diaphragm_annulus_tag">
124     <annulus_surface name="rs_diaphragm_annulus_surface" z="0." r1="0.03" r2="0.075
        "
125     radial_mesh_count="22" radial_mesh_power="1.5" axial_mesh_count="64"/>
126 </tag>
127 <define name="rs_diaphragm_aperture_diameter" value="0.0033"/>
128 <tag name="all_tag" name="rs_diaphragm_tag" name="rs_diaphragm_cylinder_tag">
129     <cylinder_tube_space name="rs_diaphragm_cylinder_tube_space" z1="0." r1="{0.5*[
        rs_diaphragm_aperture_diameter]}" z2="-0.00063" r2="0.05"
130     longitudinal_mesh_count="2" longitudinal_mesh_power="1.5" radial_mesh_count="24
        " radial_mesh_power="1.5" axial_mesh_count="64"/>
131 </tag>
132 <space name="rs_diaphragm_system_assembly">
133     <surface name="rs_diaphragm_annulus_assembly" node="
        rs_diaphragm_annulus_surface">
134         <transformation displacement="0. 0. 0."/>
135     </surface>
136     <space name="rs_diaphragm_cylinder_assembly" tree="
        rs_diaphragm_cylinder_tube_space">
137         <transformation displacement="0. 0.01 0."/>
138     </space>
139 </space>
140 </geometry>
```

A.2. E-gun geometry definition

```
<!-- XML geometry for the rearsection EGun -->
<!-- shape parameters for the EGun geometry -->
<define name="rs_egun_plate_deburring_r" value="{5.e-4}"/>
<define name="rs_egun_plate_inner_t" value="{5.24e-4}"/>
<define name="rs_egun_plate_distance" value="{1.e-2}"/>
<define name="rs_egun_backplate_z" value="0."/>
<define name="rs_egun_backplate_t" value="{[rs_egun_plate_inner_t]+2*[
    rs_egun_plate_deburring_r]}"/>
<define name="rs_egun_backplate_r" value="{5.e-2}"/>
<define name="rs_egun_goldcoating_t" value="{20.e-9}"/>
<define name="rs_egun_goldcoating_r" value="{2.5e-2}"/>
<define name="rs_egun_beamspot_r" value="{100.e-6}"/>
<define name="rs_egun_frontplate_z" value="0."/>
<define name="rs_egun_frontplate_t" value="[rs_egun_backplate_t]"/>
<define name="rs_egun_frontplate_r" value="[rs_egun_backplate_r]"/>
<define name="rs_egun_frontplate_hole_r" value="{3.e-3}"/>

<geometry>
    <!-- global meshing parameters for the EGun geometry -->
    <define name="rs_egun_curvature_n" value="2"/>
    <define name="rs_egun_opening_curvature_n" value="9"/>
    <define name="rs_egun_arc_count" value="96"/>
    <define name="rs_egun_mesh_scale" value="10"/>
    <define name="rs_egun_mesh_power" value="1.5"/>

    <!-- EGun backplate surface -->
    <!-- reference point is front side of backplate-->
    <tag name="rs_electrode_tag" name="rs_egun_tag" name="
        rs_egun_backplate_system_tag" name="rs_egun_backplate_tag">
        <rotated_poly_loop_surface name="rs_egun_backplate_surface" rotated_mesh_count=
            "[rs_egun_arc_count]">
            <poly_loop>
                <start_point x="{[rs_egun_backplate_z]}" y="0."/>
                <next_line
                    x="{[rs_egun_backplate_z]}"
                    y="{[rs_egun_backplate_r]-[rs_egun_plate_deburring_r]}"
                    line_mesh_count="{3*[rs_egun_mesh_scale]}"
                    line_mesh_power="[rs_egun_mesh_power]"
                />
                <next_arc
                    x="{[rs_egun_backplate_z]-[rs_egun_plate_deburring_r]}"
                    y="{[rs_egun_backplate_r]}"
                    radius="[rs_egun_plate_deburring_r]"
                    right="true"
                    short="true"
                    arc_mesh_count="{[rs_egun_curvature_n]}"
                />
                <next_line
                    x="{[rs_egun_backplate_z]-[rs_egun_plate_deburring_r]-[
                        rs_egun_plate_inner_t]}"
                    y="[rs_egun_backplate_r]"
                    line_mesh_count="{0.2*[rs_egun_mesh_scale]}"
                    line_mesh_power="{2/3*[rs_egun_mesh_power]}"
                />
                <next_arc
                    x="{[rs_egun_backplate_z]-[rs_egun_backplate_t]}"
                    y="{[rs_egun_backplate_r]-[rs_egun_plate_deburring_r]}"
                    radius="[rs_egun_plate_deburring_r]"
```

```
55                      right="true"
56                      short="true"
57                      arc_mesh_count="{[rs_egun_curvature_n]}"
58                  />
59                  <next_line
60                      x="{[rs_egun_backplate_z]-[rs_egun_backplate_t]}"
61                      y="{0.0}"
62                      line_mesh_count="{3*[rs_egun_mesh_scale]}"
63                      line_mesh_power="{[rs_egun_mesh_power]}"
64                  />
65                  <last_line
66                      line_mesh_count="{0.2*[rs_egun_mesh_scale]}"
67                      line_mesh_power="{2/3*[rs_egun_mesh_power]}"
68                  />
69              </poly_loop>
70          </rotated_poly_loop_surface>
71      </tag> <!-- rs_egun_backplate_tag -->
72      <tag name="rs_egun_backplate_system_tag" name="rs_egun_goldcoating_tag">
73          <rotated_poly_loop_surface name="rs_egun_goldcoating_surface" rotated_mesh_count
                ="[rs_egun_arc_count]">
74              <poly_loop>
75                  <start_point x="{[rs_egun_backplate_z]}" y="0."/>
76                  <next_line
77                      x="{[rs_egun_backplate_z]}"
78                      y="{[rs_egun_goldcoating_r]}"
79                      line_mesh_count="{0.6*[rs_egun_mesh_scale]}"
80                      line_mesh_power="[rs_egun_mesh_power]"
81                  />
82                  <next_arc
83                      x="{[rs_egun_backplate_z]+[rs_egun_goldcoating_t]}"
84                      y="{[rs_egun_goldcoating_r]-[rs_egun_goldcoating_t]}"
85                      radius="{[rs_egun_goldcoating_t]}"
86                      right="false"
87                      short="true"
88                      arc_mesh_count="{[rs_egun_curvature_n]}"
89                  />
90                  <next_line
91                      x="{[rs_egun_backplate_z]+[rs_egun_goldcoating_t]}"
92                      y="0."
93                      line_mesh_count="{0.5*[rs_egun_mesh_scale]}"
94                      line_mesh_power="{[rs_egun_mesh_power]}"
95                  />
96                  <last_line
97                      line_mesh_count="{0.1*[rs_egun_mesh_scale]}"
98                      line_mesh_power="{[rs_egun_mesh_power]}"
99                  />
100             </poly_loop>
101         </rotated_poly_loop_surface>
102     </tag> <!-- rs_egun_goldcoating_tag -->
103     <tag name="rs_egun_backplate_system_tag" name="rs_egun_beamspot_tag">
104         <rotated_line_segment_surface name="rs_egun_beamspot_surface"
                rotated_mesh_count="[rs_egun_arc_count]">
105             <line_segment
106                 x1="{[rs_egun_backplate_z]}"
107                 y1="{0.}"
108                 x2="{[rs_egun_backplate_z]}"
109                 y2="{[rs_egun_beamspot_r]}"
110                 line_mesh_count="{0.3*[rs_egun_mesh_scale]}"
111                 line_mesh_power="{1.}"
```

```
112             />
113         </rotated_line_segment_surface>
114     </tag> <!-- rs_egun_beamspot_tag -->
115
116     <!-- EGun frontplate surface -->
117         <!-- reference point is back side of frontplate=rs_egun_frontplate_z-->
118     <tag name="all_tag" name="rs_electrode_tag" name="rs_egun_tag" name="
            rs_egun_frontplate_tag">
119         <rotated_poly_loop_surface name="rs_egun_frontplate_surface" rotated_mesh_count
                ="[rs_egun_arc_count]">
120             <poly_loop>
121                 <!--start at left down corner after arc -->
122                 <start_point x="{[rs_egun_frontplate_z]+[rs_egun_plate_deburring_r]}" y="
                        {[rs_egun_frontplate_hole_r]}"/>
123                 <next_line
124                     x="{[rs_egun_frontplate_z]+[rs_egun_plate_inner_t]+[
                            rs_egun_plate_deburring_r]}"
125                     y="{[rs_egun_frontplate_hole_r]}"
126                     line_mesh_count="{0.2*[rs_egun_mesh_scale]}"
127                     line_mesh_power="{2/3*[rs_egun_mesh_power]}"
128                 />
129                 <!-- right down corner arc -->
130                 <next_arc
131                     x="{[rs_egun_frontplate_z]+[rs_egun_frontplate_t]}"
132                     y="{[rs_egun_frontplate_hole_r]+[rs_egun_plate_deburring_r]}"
133                     radius="{[rs_egun_plate_deburring_r]}"
134                     right="true"
135                     short="true"
136                     arc_mesh_count="{[rs_egun_curvature_n]}"
137                 />
138                 <!-- right side -->
139                 <next_line
140                     x="{[rs_egun_frontplate_z]+[rs_egun_frontplate_t]}"
141                     y="{[rs_egun_frontplate_r]-[rs_egun_plate_deburring_r]}"
142                     line_mesh_count="{3*[rs_egun_mesh_scale]}"
143                     line_mesh_power="{[rs_egun_mesh_power]}"
144                 />
145                 <!-- right top corner arc -->
146                 <next_arc
147                     x="{[rs_egun_frontplate_z]+[rs_egun_frontplate_t]-[
                            rs_egun_plate_deburring_r]}"
148                     y="{[rs_egun_frontplate_r]}"
149                     radius="{[rs_egun_plate_deburring_r]}"
150                     right="true"
151                     short="true"
152                     arc_mesh_count="{[rs_egun_curvature_n]}"
153                 />
154                 <!-- top side -->
155                 <next_line
156                     x="{[rs_egun_frontplate_z]+[rs_egun_plate_deburring_r]}"
157                     y="{[rs_egun_frontplate_r]}"
158                     line_mesh_count="{0.2*[rs_egun_mesh_scale]}"
159                     line_mesh_power="{2/3*[rs_egun_mesh_power]}"
160                 />
161                 <!-- left top corner arc -->
162                 <next_arc
163                     x="{[rs_egun_frontplate_z]}"
164                     y="{[rs_egun_frontplate_r]-[rs_egun_plate_deburring_r]}"
165                     radius="{[rs_egun_plate_deburring_r]}"
```

```
                    right="true"
                    short="true"
                    arc_mesh_count="{[rs_egun_curvature_n]}"
                />
                <!-- left side -->
                <next_line
                    x="{[rs_egun_frontplate_z]}"
                    y="{[rs_egun_frontplate_hole_r]+[rs_egun_plate_deburring_r]}"
                    line_mesh_count="{3*[rs_egun_mesh_scale]}"
                    line_mesh_power="{[rs_egun_mesh_power]}"
                />
                <!-- left down corner arc, closing the surface -->
                <last_arc
                    radius="{[rs_egun_plate_deburring_r]}"
                    right="true"
                    short="true"
                    arc_mesh_count="{[rs_egun_curvature_n]}"
                />
            </poly_loop>
        </rotated_poly_loop_surface>
    </tag>
</geometry>
```

A.3. Post acceleration geometry definitions

```
<!-- XML geometry for the rearsection post acceleration electrodes -->
<geometry>
    <!-- shape parameters for the post acceleration electrodes geometry -->
    <define name="rs_postacc_electrode_t" value="0.001"/>
    <define name="rs_postacc_electrode_deburring_r" value="0.00025"/>
    <loop variable="i" start="1" end="3" step="1">
        <define name="rs_postacc_electrode[i]_z" value="0."/>
    </loop>
    <define name="rs_postacc_electrode1_pos" value="0."/>
    <define name="rs_postacc_electrode1_r" value="0.058"/>
    <global_define name="rs_postacc_electrode1_l" value="0.395"/>
    <global_define name="rs_postacc_electrode2_pos" value="{[rs_postacc_electrode1_pos]+[
        rs_postacc_electrode1_l]-0.019}"/>
    <define name="rs_postacc_electrode2_r" value="0.043"/>
    <global_define name="rs_postacc_electrode2_l" value="0.079"/>
    <global_define name="rs_postacc_electrode3_pos" value="{[rs_postacc_electrode2_pos]+[
        rs_postacc_electrode2_l]-0.019}"/>
    <define name="rs_postacc_electrode3_r" value="0.050"/>
    <define name="rs_postacc_electrode3_l" value="0.1"/>

    <!-- global meshing parameters for the post acceleration geometry -->
    <define name="rs_postacc_curvature_n" value="2"/>
    <define name="rs_postacc_opening_curvature_n" value="9"/>
    <define name="rs_postacc_arc_count" value="96"/>
    <define name="rs_postacc_mesh_scale" value="10"/>
    <define name="rs_postacc_mesh_power" value="1.5"/>

    <!-- post acceleration electrode surface -->
    <!-- reference point is back z value of each electrode -->
    <tag name="all_tag" name="electrode_tag" name="rs_electrode_tag" name="
        rs_axial_electrode_tag" name="rs_postacc_electrode_tag" >
        <loop variable="i" start="1" end="3" step="1">
```

```
30          <tag name="rs_postacc_electrode[i]_tag">
31
32              <rotated_poly_loop_surface name="rs_postacc_electrode[i]_surface"
                    rotated_mesh_count="[rs_postacc_arc_count]">
33              <poly_loop>
34                  <!--start at left down corner after arc -->
35                  <start_point x="{[rs_postacc_electrode[i]_z]+[
                        rs_postacc_electrode_deburring_r]}" y="{[rs_postacc_electrode[i]_r
                        ]}"/>
36                  <next_line
37                      x="{[rs_postacc_electrode[i]_z]+[rs_postacc_electrode[i]_l]-[
                            rs_postacc_electrode_deburring_r]}"
38                      y="{[rs_postacc_electrode[i]_r]}"
39                      line_mesh_count="{1.5*[rs_postacc_mesh_scale]}"
40                      line_mesh_power="[rs_postacc_mesh_power]"
41                  />
42                  <!-- right down corner arc -->
43                  <next_arc
44                      x="{[rs_postacc_electrode[i]_z]+[rs_postacc_electrode[i]_l]}"
45                      y="{[rs_postacc_electrode[i]_r]+[rs_postacc_electrode_deburring_r
                            ]}"
46                      radius="{[rs_postacc_electrode_deburring_r]}"
47                      right="true"
48                      short="true"
49                      arc_mesh_count="{[rs_postacc_curvature_n]}"
50                  />
51                  <!-- right side -->
52                  <next_line
53                      x="{[rs_postacc_electrode[i]_z]+[rs_postacc_electrode[i]_l]}"
54                      y="{[rs_postacc_electrode[i]_r]+[rs_postacc_electrode_t]-[
                            rs_postacc_electrode_deburring_r]}"
55                      line_mesh_count="{0.2*[rs_postacc_mesh_scale]}"
56                      line_mesh_power="[rs_postacc_mesh_power]"
57                  />
58                  <!-- right top corner arc -->
59                  <next_arc
60                      x="{[rs_postacc_electrode[i]_z]+[rs_postacc_electrode[i]_l]-[
                            rs_postacc_electrode_deburring_r]}"
61                      y="{[rs_postacc_electrode[i]_r]+[rs_postacc_electrode_t]}"
62                      radius="{[rs_postacc_electrode_deburring_r]}"
63                      right="true"
64                      short="true"
65                      arc_mesh_count="{[rs_postacc_curvature_n]}"
66                  />
67                  <!-- top side -->
68                  <next_line
69                      x="{[rs_postacc_electrode[i]_z]+[rs_postacc_electrode_deburring_r
                            ]}"
70                      y="{[rs_postacc_electrode[i]_r]+[rs_postacc_electrode_t]}"
71                      line_mesh_count="{1.5*[rs_postacc_mesh_scale]}"
72                      line_mesh_power="[rs_postacc_mesh_power]"
73                  />
74                  <!-- left top corner arc -->
75                  <next_arc
76                      x="{[rs_postacc_electrode[i]_z]}"
77                      y="{[rs_postacc_electrode[i]_r]+[rs_postacc_electrode_t]-[
                            rs_postacc_electrode_deburring_r]}"
78                      radius="{[rs_postacc_electrode_deburring_r]}"
79                      right="true"
```

```
                    short="true"
                    arc_mesh_count="{[rs_postacc_curvature_n]}"
                />
                <!-- left side -->
                <next_line
                    x="{[rs_postacc_electrode[i]_z]}"
                    y="{[rs_postacc_electrode[i]_r]+[rs_postacc_electrode_deburring_r]}"
                    line_mesh_count="{0.2*[rs_postacc_mesh_scale]}"
                    line_mesh_power="[rs_postacc_mesh_power]"
                />
                <!-- left down corner arc, closing the surface -->
                <last_arc
                    radius="{[rs_postacc_electrode_deburring_r]}"
                    right="true"
                    short="true"
                    arc_mesh_count="{[rs_postacc_curvature_n]}"
                />
            </poly_loop>
        </rotated_poly_loop_surface>

        </tag> <!-- rs_postacc_electrode[i]_tag -->
    </loop> <!-- -->
</tag> <!--all_tag -->
</geometry>
```

A.4. Electric dipole electrodes geometry definitions

```
<!-- XML geometry for the rearsection electric dipoles -->
<!-- shape parameters for the electric dipole geometry -->
<geometry>
    <!-- global meshing parameters for the ElectricDipoles geometry -->
    <define name="rs_electricdipoles_mesh_scale" value="10"/>
    <define name="rs_electricdipoles_mesh_power" value="2."/>

    <!-- large plate -->
    <!-- reference point is left side at y=0 -->
    <tag name="all_tag" name="rs_electrode_tag" name="rs_electricdipole_system_tag"
         name="rs_electricdipole_tag" name="rs_electricdipole_large_tag">
        <extruded_line_segment_surface name="rs_electricdipole_surface_large" zmin="0."
            zmax="1.0" extruded_mesh_count="{10*[rs_electricdipoles_mesh_scale]}"
            extruded_mesh_power="{0.75*[rs_electricdipoles_mesh_power]}">
            <line_segment x1="0." y1="-0.03" x2="0." y2="0.03" line_mesh_count="{0.75*[
                rs_electricdipoles_mesh_scale]}" line_mesh_power="{0.75*[
                rs_electricdipoles_mesh_power]}"/>
        </extruded_line_segment_surface>
    </tag>

    <!-- small plate -->
    <!-- reference point is left side at y=0 -->
    <tag name="all_tag" name="rs_electrode_tag" name="rs_electricdipole_system_tag"
         name="rs_electricdipole_tag" name="rs_electricdipole_small_tag">
        <extruded_line_segment_surface name="rs_electricdipole_surface_small" zmin="0."
            zmax="0.1" extruded_mesh_count="{3*[rs_electricdipoles_mesh_scale]}"
            extruded_mesh_power="{0.75*[rs_electricdipoles_mesh_power]}">
            <line_segment x1="0." y1="-0.03" x2="0." y2="0.03" line_mesh_count="{0.75*[
                rs_electricdipoles_mesh_scale]}" line_mesh_power="{0.75*[
                rs_electricdipoles_mesh_power]}"/>
```

```
21          </extruded_line_segment_surface>
22      </tag>
23
24      <!-- rs_electricdipole_system assembly -->
25      <space name="rs_electricdipole_system_assembly">
26          <!-- front plate -->
27          <surface name="rs_electricdipole_front_small1" node="
                rs_electricdipole_surface_small ">
28              <transformation rotation_axis_angle="{-165.96} {90.} {90.}"/> <!-- rotation
                    around y axis -->
29              <transformation displacement="-0.02 0. 0."/>
30          </surface>
31          <surface name="rs_electricdipole_front_large" node="
                rs_electricdipole_surface_large ">
32              <transformation rotation_axis_angle="{0.} {90.} {90.}"/> <!-- rotation
                    around y axis -->
33              <transformation displacement="-0.02 0. 0."/>
34          </surface>
35          <surface name="rs_electricdipole_front_small2" node="
                rs_electricdipole_surface_small ">
36              <transformation rotation_axis_angle="{-(180.-165.96)} {90.} {90.}"/> <!--
                    rotation around y axis -->
37              <transformation displacement="-0.02 0. 1.0"/>
38          </surface>
39
40          <!-- rear plate -->
41          <surface name="rs_electricdipole_rear_small1" node="
                rs_electricdipole_surface_small ">
42              <transformation rotation_axis_angle="{165.96} {90.} {90.}"/> <!-- rotation
                    around y axis -->
43              <transformation displacement="0.02 0. 0."/>
44          </surface>
45          <surface name="rs_electricdipole_rear_large" node=" rs_electricdipole_surface_large
                ">
46              <transformation rotation_axis_angle="{0.} {90.} {90.}"/> <!-- rotation
                    around y axis -->
47              <transformation displacement="0.02 0. 0."/>
48          </surface>
49          <surface name="rs_electricdipole_rear_small2" node="
                rs_electricdipole_surface_small ">
50              <transformation rotation_axis_angle="{180.-165.96} {90.} {90.}"/> <!--
                    rotation around y axis -->
51              <transformation displacement="0.02 0. 1.0"/>
52          </surface>
53      </space>
54  </geometry>
```

A.5. Solenoid geometry definitions

```
1  <!-- XML geometry for the rearsection magnets -->
2  <geometry>
3      <!-- shape parameters for the magnets geometry -->
4      <define name="rs_solenoid_z1" value="0."/>
5      <define name="rs_solenoid_z2" value="0.796"/>
6      <define name="rs_solenoid_r1" value="0.1095"/>
7      <define name="rs_solenoid_r2" value="0.154"/>
8      <define name="rs_solenoid1_pos" value="0."/>
```

```
    <define name="rs_solenoid2_pos" value="0.824"/>
    <define name="rs_solenoid3_pos" value="1.648"/>
    <define name="rs_solenoid_booster_z1" value="0."/>
    <define name="rs_solenoid_booster_z2" value="0.1"/>
    <define name="rs_solenoid_booster_r1" value="0.194"/>
    <define name="rs_solenoid_booster_r2" value="0.244"/>
    <define name="rs_EGun_solenoid_z1" value="0."/>
    <define name="rs_EGun_solenoid_z2" value="0.05"/>
    <define name="rs_EGun_solenoid_r1" value="0.105"/>
    <define name="rs_EGun_solenoid_r2" value="0.205"/>
    <define name="rscm_main_z1" value="0."/>
    <define name="rscm_main_z2" value="0.63"/>
    <define name="rscm_main_r1" value="0.16"/>
    <define name="rscm_main_r2" value="0.18616"/>
    <define name="rscm_main_booster_z1" value="0."/>
    <define name="rscm_main_booster_z2" value="0.0805"/>
    <define name="rscm_main_booster_r1" value="[rscm_main_r2]"/>
    <define name="rscm_main_booster_r2" value="0.21101"/>

    <!-- global meshing parameters for the magnet geometry -->
    <define name="magnet_longitudinal_mesh_count" value="10"/>
    <define name="magnet_radial_mesh_count" value="12"/>
    <define name="magnet_axial_mesh_count" value="128"/>
    <define name="magnet_mesh_scale" value="10"/>
    <define name="magnet_mesh_power" value="2."/>

    <!-- rs solenoid surface -->
    <!-- reference point is back z value of each solenoid -->
    <tag name="all_tag" name="magnet_tag" name="rs_magnet_tag">
        <tag name="rs_solenoid_tag">
            <cylinder_tube_space
                name="rs_solenoid_space"
                z1="[rs_solenoid_z1]"
                r1="[rs_solenoid_r1]"
                z2="[rs_solenoid_z2]"
                r2="[rs_solenoid_r2]"
                longitudinal_mesh_count="[magnet_longitudinal_mesh_count]"
                longitudinal_mesh_power="[magnet_mesh_power]"
                radial_mesh_count="{0.5*[magnet_radial_mesh_count]}"
                radial_mesh_power="[magnet_mesh_power]"
                axial_mesh_count="[magnet_axial_mesh_count]"
            />
        </tag>
        <tag name="rs_solenoid_booster_tag">
            <cylinder_tube_space
                name="rs_solenoid_booster_space"
                z1="[rs_solenoid_booster_z1]"
                r1="[rs_solenoid_booster_r1]"
                z2="[rs_solenoid_booster_z2]"
                r2="[rs_solenoid_booster_r2]"
                longitudinal_mesh_count="{0.5*[magnet_longitudinal_mesh_count]}"
                longitudinal_mesh_power="[magnet_mesh_power]"
                radial_mesh_count="{0.5*[magnet_radial_mesh_count]}"
                radial_mesh_power="[magnet_mesh_power]"
                axial_mesh_count="[magnet_axial_mesh_count]"
            />
        </tag>
    </tag>
```

```
68      <!-- rs EGun solenoid surface -->
69      <!-- reference point is back z value of EGun solenoid -->
70      <tag name="all_tag" name="magnet_tag" name="rs_magnet_tag" name="
            rs_EGun_solenoid_tag">
71          <cylinder_tube_space
72              name="rs_EGun_solenoid_space"
73              z1="[rs_EGun_solenoid_z1]"
74              r1="[rs_EGun_solenoid_r1]"
75              z2="[rs_EGun_solenoid_z2]"
76              r2="[rs_EGun_solenoid_r2]"
77              longitudinal_mesh_count="{0.5*[magnet_longitudinal_mesh_count]}"
78              longitudinal_mesh_power="[magnet_mesh_power]"
79              radial_mesh_count="{0.5*[magnet_radial_mesh_count]}"
80              radial_mesh_power="[magnet_mesh_power]"
81              axial_mesh_count="[magnet_axial_mesh_count]"
82          />
83      </tag>
84
85      <!-- rs superconducting magnet surface -->
86      <!-- reference point is back z value of sc magnet -->
87      <tag name="all_tag" name="magnet_tag" name="rs_magnet_tag" name="rscm_tag">
88          <tag name="rscm_main_tag">
89              <cylinder_tube_space
90                  name="rscm_main_space"
91                  z1="[rscm_main_z1]"
92                  r1="[rscm_main_r1]"
93                  z2="[rscm_main_z2]"
94                  r2="[rscm_main_r2]"
95                  longitudinal_mesh_count="[magnet_longitudinal_mesh_count]"
96                  longitudinal_mesh_power="[magnet_mesh_power]"
97                  radial_mesh_count="{0.5*[magnet_radial_mesh_count]}"
98                  radial_mesh_power="[magnet_mesh_power]"
99                  axial_mesh_count="[magnet_axial_mesh_count]"
100             />
101         </tag>
102
103         <tag name="rscm_main_booster_tag">
104             <cylinder_tube_space
105                 name="rscm_main_booster_space"
106                 z1="[rscm_main_booster_z1]"
107                 r1="[rscm_main_booster_r1]"
108                 z2="[rscm_main_booster_z2]"
109                 r2="[rscm_main_booster_r2]"
110                 longitudinal_mesh_count="{0.5*[magnet_longitudinal_mesh_count]}"
111                 longitudinal_mesh_power="[magnet_mesh_power]"
112                 radial_mesh_count="{0.5*[magnet_radial_mesh_count]}"
113                 radial_mesh_power="[magnet_mesh_power]"
114                 axial_mesh_count="[magnet_axial_mesh_count]"
115             />
116         </tag>
117     </tag>
118 </geometry>
```

A.6. Magnetic dipoles geometry definitions

```
1 <!-- XML geometry for the rearsection magnetic dipoles -->
2 <geometry>
```

```
3   <!-- shape parameters for the magnetic dipoles geometry -->
4   <define name="rs_magnetic_dipole1_width" value="0.285"/>
5   <global_define name="rs_magnetic_dipole1_length" value="1.095"/>
6   <global_define name="rs_magnetic_dipole1_centerpos_z" value="-3.4163"/>
7   <define name="rs_magnetic_dipole1_tube_diameter" value="0.03"/>
8   <define name="rs_magnetic_dipole1_corner_radius" value="0.0325"/>
9   <define name="rs_magnetic_dipole1_corner_nsegments" value="7"/>
10
11  <define name="rs_magnetic_dipole2_width" value="0.285"/>
12  <global_define name="rs_magnetic_dipole2_length" value="0.675"/>
13  <global_define name="rs_magnetic_dipole2_centerpos_z" value="-2.3053"/>
14  <define name="rs_magnetic_dipole2_tube_diameter" value="0.03"/>
15  <define name="rs_magnetic_dipole2_corner_radius" value="0.0325"/>
16  <define name="rs_magnetic_dipole2_corner_nsegments" value="7"/>
17
18  <!-- magnetic dipole coil, reference point is centered back value name="magnet_tag"
        -->
19  <tag name="all_tag" name="magnet_tag" name="rs_magnet_tag" name="
        rs_magnetic_dipole_tag">
20      <loop variable="j" start="1" end="2" step="1">
21          <tag name="rs_magnetic_dipole[j]_tag">
22              <rod_space name="rs_magnetic_dipole[j]_space">
23                  <rod radius="{[rs_magnetic_dipole[j]_tube_diameter]/2}"
                        longitudinal_mesh_count="10" axial_mesh_count="12">
24                      <vertex x="0" y="0" z="{-[rs_magnetic_dipole[j]_length]/2}"/>
25
26                      <loop variable="i" start="0" end="{[rs_magnetic_dipole[j]
                            _corner_nsegments]}" step="1">
27                          <vertex
28                              x="{-[rs_magnetic_dipole[j]_width]/2+[rs_magnetic_dipole[j
                                ]_corner_radius]*(1-TMath::Sin(0.5*TMath::Pi()*[i]/[
                                rs_magnetic_dipole[j]_corner_nsegments]))}"
29                              y="{0}"
30                              z="{-[rs_magnetic_dipole[j]_length]/2+[rs_magnetic_dipole[
                                j]_corner_radius]*(1-TMath::Cos(0.5*TMath::Pi()*[i
                                ]/[rs_magnetic_dipole[j]_corner_nsegments]))}"
31                          />
32                      </loop>
33
34                      <loop variable="i" start="0" end="{[rs_magnetic_dipole[j]
                            _corner_nsegments]}" step="1">
35                          <vertex
36                              x="{-[rs_magnetic_dipole[j]_width]/2+[rs_magnetic_dipole[j
                                ]_corner_radius]*(1-TMath::Cos(0.5*TMath::Pi()*[i]/[
                                rs_magnetic_dipole[j]_corner_nsegments]))}"
37                              y="{0}"
38                              z="{-[rs_magnetic_dipole[j]_length]/2+[rs_magnetic_dipole[
                                j]_length]-[rs_magnetic_dipole[j]_corner_radius]*(1-
                                TMath::Sin(0.5*TMath::Pi()*[i]/[rs_magnetic_dipole[j]
                                _corner_nsegments]))}"
39                          />
40                      </loop>
41
42                      <loop variable="i" start="0" end="{[rs_magnetic_dipole[j]
                            _corner_nsegments]}" step="1">
43                          <vertex
44                              x="{[rs_magnetic_dipole[j]_width]/2-[rs_magnetic_dipole[j]
                                _corner_radius]+[rs_magnetic_dipole[j]_corner_radius]*
                                TMath::Sin(0.5*TMath::Pi()*[i]/[rs_magnetic_dipole[j]
```

```
                                    _corner_nsegments])}"
45                                  y="{0}"
46                                  z="{-[rs_magnetic_dipole[j]_length]/2+[rs_magnetic_dipole[
                                        j]_length]-[rs_magnetic_dipole[j]_corner_radius]*(1-
                                        TMath::Cos(0.5*TMath::Pi()*[i]/[rs_magnetic_dipole[j]
                                        _corner_nsegments]))}"
47                              />
48                          </loop>
49
50                          <loop variable="i" start="0" end="{[rs_magnetic_dipole[j]
                                _corner_nsegments]}" step="1">
51                              <vertex
52                                  x="{[rs_magnetic_dipole[j]_width]/2-[rs_magnetic_dipole[j]
                                        _corner_radius]*(1-TMath::Cos(0.5*TMath::Pi()*[i]/[
                                        rs_magnetic_dipole[j]_corner_nsegments]))}"
53                                  y="{0}"
54                                  z="{-[rs_magnetic_dipole[j]_length]/2+[rs_magnetic_dipole[
                                        j]_corner_radius]*(1-TMath::Sin(0.5*TMath::Pi()*[i]/[
                                        rs_magnetic_dipole[j]_corner_nsegments]))}"
55                              />
56                          </loop>
57
58                          <vertex x="0" y="0" z="{-[rs_magnetic_dipole[j]_length]/2}"/>
59                      </rod>
60                  </rod_space>
61              </tag>
62          </loop>
63      </tag>
64  </geometry>
```

APPENDIX B

REAR SECTION ASSEMBLY OF COMPONENTS

B.1. Rear Section complete geometry

```
<!-- XML geometry for the complete rearsection -->
<define name="rearsection_config_path" value="@KSC_CONFIG_INSTALL_DIR@"/>

<!-- global variables -->
<external_define name="dps1r_flange_reference" value="{0.}"/>
<external_define name="rs_egun_tilt_angle" value="{10.}"/>

<!-- include geometry config files of different parts of rearsection -->
<include path="[rearsection_config_path]/../TheBag/Rearsection" base="
    RearsectionGroundElectrodeGeometry.xml"/>
<include path="[rearsection_config_path]/../TheBag/Rearsection" base="
    RearsectionEGunGeometry.xml"/>
<include path="[rearsection_config_path]/../TheBag/Rearsection" base="
    RearsectionPostAccelerationElectrodesGeometry.xml"/>
<include path="[rearsection_config_path]/../TheBag/Rearsection" base="
    RearsectionElectricDipolesGeometry.xml"/>
<include path="[rearsection_config_path]/../TheBag/Rearsection" base="
    RearsectionMagnetsGeometry.xml"/>
<include path="[rearsection_config_path]/../TheBag/Rearsection" base="
    RearsectionMagDipolesGeometry.xml"/>

<geometry>
    <space name="rearsection_assembly">
        <!-- rs electrodes -->
        <surface name="rs_ground_assembly" node="rs_ground_electrode_surface" >
            <transformation displacement="{0.} {0.} {0.}"/>
        </surface>
        <tag name="rs_egun_assembly_tag">
            <space name="rs_egun_assembly" tree="rs_egun_plate_system_assembly">
                <transformation rotation_axis_angle="{[rs_egun_tilt_angle]} {90.} {90.}"/
                    > <!-- rotation around y axis -->
                <transformation displacement="{0.} {0.} {[dps1r_flange_reference]+ -4.58}
                    "/>
            </space>
        </tag>

```

```
29      <surface name="rs_postacc_electrode1_assembly" node="
            rs_postacc_electrode1_surface" >
30          <transformation displacement="{0.} {0.} {[dps1r_flange_reference]+ -4.615}"/
                >
31      </surface>
32      <surface name="rs_postacc_electrode2_assembly" node="
            rs_postacc_electrode2_surface" >
33          <transformation displacement="{0.} {0.} {[dps1r_flange_reference]+ -4.615 +[
                rs_postacc_electrode2_pos]}"/>
34      </surface>
35      <surface name="rs_postacc_electrode3_assembly" node="
            rs_postacc_electrode3_surface" >
36          <transformation displacement="{0.} {0.} {[dps1r_flange_reference]+ -4.615 +[
                rs_postacc_electrode3_pos]}"/>
37      </surface>
38
39      <space name="rs_electricdipoles_assembly" tree="rs_electricdipole_system_assembly"
            >
40          <transformation displacement="{0.} {0.} {[dps1r_flange_reference]+ -3.805}"/
                >
41      </space>
42
43      <space name="rs_diaphragm_assembly" tree="rs_diaphragm_system_assembly">
44          <transformation displacement="0. 0. {[rs_ground_electrode_z2] + [
                rs_ground_dps1r-flange_reference] -0.003}"/>
45      </space>
46
47      <!-- rs magnets -->
48      <space name="rs_EGun_solenoid_assembly" tree="rs_EGun_solenoid_space">
49              <transformation displacement="{0.} {0.} {[dps1r_flange_reference]+
                    -4.6266}"/>
50      </space>
51
52      <space name="rs_solenoid_booster_assembly" tree="rs_solenoid_booster_space" >
53          <transformation displacement="{0.} {0.} {[dps1r_flange_reference]+ -4.3266}"/
                >
54      </space>
55
56      <space name="rs_solenoid1_assembly" tree="rs_solenoid_space" >
57          <transformation displacement="{0.} {0.} {[dps1r_flange_reference]+ -4.3466}"/
                >
58      </space>
59      <space name="rs_solenoid2_assembly" tree="rs_solenoid_space" >
60          <transformation displacement="{0.} {0.} {[dps1r_flange_reference]+ -4.3466 +
                0.824}"/>
61      </space>
62      <space name="rs_solenoid3_assembly" tree="rs_solenoid_space" >
63          <transformation displacement="{0.} {0.} {[dps1r_flange_reference]+ -4.3466 +
                1.648}"/>
64      </space>
65
66      <space name="rs_magnetic_dipole1_top_assembly" tree="rs_magnetic_dipole1_space"
            >
67          <transformation displacement="0. 0.178 {[dps1r_flange_reference]+ [
                rs_magnetic_dipole1_centerpos_z]}"/>
68      </space>
69      <space name="rs_magnetic_dipole1_bottom_assembly" tree="
            rs_magnetic_dipole1_space" >
```

```
70              <transformation displacement="0. -0.178 {[dps1r_flange_reference]+ [
                    rs_magnetic_dipole1_centerpos_z]}"/>
71          </space>
72          <space name="rs_magnetic_dipole1_front_assembly" tree="
                rs_magnetic_dipole1_space" >
73              <transformation rotation_axis_angle="90. 0. -90."/>
74              <transformation displacement="-0.178 0. {[dps1r_flange_reference]+ [
                    rs_magnetic_dipole1_centerpos_z]}"/>
75          </space>
76          <space name="rs_magnetic_dipole1_rear_assembly" tree="rs_magnetic_dipole1_space
                " >
77              <transformation rotation_axis_angle="90. 0. -90."/>
78              <transformation displacement="0.178 0. {[dps1r_flange_reference]+ [
                    rs_magnetic_dipole1_centerpos_z]}"/>
79          </space>
80          <space name="rs_magnetic_dipole2_top_assembly" tree="rs_magnetic_dipole2_space"
                >
81              <transformation displacement="0. 0.178 {[dps1r_flange_reference]+ [
                    rs_magnetic_dipole2_centerpos_z]}"/>
82          </space>
83          <space name="rs_magnetic_dipole2_bottom_assembly" tree="
                rs_magnetic_dipole2_space" >
84              <transformation displacement="0. -0.178 {[dps1r_flange_reference]+ [
                    rs_magnetic_dipole2_centerpos_z]}"/>
85          </space>
86          <space name="rs_magnetic_dipole2_front_assembly" tree="
                rs_magnetic_dipole2_space" >
87              <transformation rotation_axis_angle="90. 0. -90."/>
88              <transformation displacement="-0.178 0. {[dps1r_flange_reference]+ [
                    rs_magnetic_dipole2_centerpos_z]}"/>
89          </space>
90          <space name="rs_magnetic_dipole2_rear_assembly" tree="rs_magnetic_dipole2_space
                " >
91              <transformation rotation_axis_angle="90. 0. -90."/>
92              <transformation displacement="0.178 0. {[dps1r_flange_reference]+ [
                    rs_magnetic_dipole2_centerpos_z]}"/>
93          </space>
94
95          <space name="rscm_main_booster1_assembly" tree="rscm_main_booster_space">
96              <transformation displacement="{0.} {0.} {[dps1r_flange_reference]+ -1.0784}"/
                    >
97          </space>
98          <space name="rscm_main_assembly" tree="rscm_main_space">
99              <transformation displacement="{0.} {0.} {[dps1r_flange_reference]+ -1.0784}"/
                    >
100         </space>
101         <space name="rscm_main_booster2_assembly" tree="rscm_main_booster_space">
102             <transformation displacement="{0.} {0.} {[dps1r_flange_reference]+ -1.0784 +
                    0.63 - 0.0805}"/>
103         </space>
104
105     </space>
106 </geometry>
```

B.2. Rear Section object properties

```
1 <define name="rearsection_config_path" value="@KSC_CONFIG_INSTALL_DIR@"/>
```

```
2
3 <include path="[rearsection_config_path]/../TheBag/Rearsection" base="
      RearsectionGeometry.xml"/>
4
5 <geometry>
6     <!-- appearance -->
7     <appearance name="app_rs_magnet" color="102 30 0 255" arc="72" spaces="
          rearsection_assembly/@rs_magnet_tag"/>
8     <appearance name="app_rs_magdipoles" color="255 140 0 255" arc="72" spaces="
          rearsection_assembly/@rs_magnetic_dipole_tag"/>
9
10    <appearance name="app_rs_ground_electrode" color="128 128 128 255" arc="72"
          surfaces="rearsection_assembly/@rs_ground_electrode_tag"/>
11    <appearance name="app_rs_ground_diaphragm" color="128 128 128 255" arc="72"
          surfaces="rearsection_assembly/@rs_diaphragm_tag" spaces="rearsection_assembly/
          @rs_diaphragm_tag"/>
12    <appearance name="app_rs_postacc_electrode" color="0 128 0 255" arc="72" surfaces="
          rearsection_assembly/@rs_postacc_electrode_tag"/>
13    <appearance name="app_rs_egun" color="0 128 0 255" arc="72" surfaces="
          rearsection_assembly/@rs_egun_tag"/>
14    <appearance name="app_rs_eldipoles" color="255 255 0 255" arc="72" surfaces="
          rearsection_assembly/@rs_electricdipole_tag"/>
15
16    <define name="b_factor" value="1.1"/>
17    <!-- magnet current values in At -->
18    <define name="rs_solenoid1_current" value="{36.5 * 777 * [b_factor]}"/>
                              <!-- 40.15 A * 777 t = 31196.55 At -->
19    <define name="rs_solenoid2_current" value="{32. * 777 * [b_factor]}"/>
                              <!-- 35.2 A * 777 t = 27350.4 At -->
20    <define name="rs_solenoid3_current" value="{32. * 777 * [b_factor]}"/>
                              <!-- 35.2 A * 777 t = 27350.4 At -->
21    <define name="rs_solenoid_booster_current" value="{53.6 * 84 * [b_factor]}"/>
                          <!-- 58.96 A * 84 t = 4952.64 At -->
22    <define name="rs_EGun_solenoid_current" value="{59.5 * 84 * [b_factor] * 0.83333333}"
          /> <!-- 54.5416 A * 84 t = 4581.5 At -->
23    <define name="rscm_main_current" value="{70 * 35314}"/>
                                          <!-- 70 A * 35314 t = 2471980 At -->
24    <define name="rscm_main_booster_current" value="{70 * 4287}"/>
                                      <!-- 70 A * 4287 t = 300090 At -->
25    <define name="rs_magnetic_dipole1_current" value="{140}" />
                                        <!-- 140 At -->
26    <define name="rs_magnetic_dipole2_current" value="{110}" />
                                        <!-- 110 At -->
27    <!-- magnetic dipoles top/bottom -->
28    <if condition="{[use_magnetic_dipoles_top_bottom]}">
29        <define name="rs_magnetic_dipole1_top_current" value="[
              rs_magnetic_dipole1_current]" />
30        <define name="rs_magnetic_dipole1_bottom_current" value="[
              rs_magnetic_dipole1_current]" />
31        <define name="rs_magnetic_dipole1_front_current" value="0" />
32        <define name="rs_magnetic_dipole1_rear_current" value="0" />
33        <define name="rs_magnetic_dipole2_top_current" value="[
              rs_magnetic_dipole2_current]" />
34        <define name="rs_magnetic_dipole2_bottom_current" value="[
              rs_magnetic_dipole2_current]" />
35        <define name="rs_magnetic_dipole2_front_current" value="0" />
36        <define name="rs_magnetic_dipole2_rear_current" value="0" />
37    </if>
38    <!-- magnetic dipoles front/rear -->
```

```
39      <if condition="{![use_magnetic_dipoles_top_bottom]}">
40          <define name="rs_magnetic_dipole1_top_current" value="0" />
41          <define name="rs_magnetic_dipole1_bottom_current" value="0" />
42          <define name="rs_magnetic_dipole1_front_current" value="[
                rs_magnetic_dipole1_current]" />
43          <define name="rs_magnetic_dipole1_rear_current" value="[
                rs_magnetic_dipole1_current]" />
44          <define name="rs_magnetic_dipole2_top_current" value="0" />
45          <define name="rs_magnetic_dipole2_bottom_current" value="0" />
46          <define name="rs_magnetic_dipole2_front_current" value="[
                rs_magnetic_dipole2_current]" />
47          <define name="rs_magnetic_dipole2_rear_current" value="[
                rs_magnetic_dipole2_current]" />
48      </if>
49
50      <!-- set values to magnets -->
51      <!-- rs solenoids -->
52      <loop variable="i" start="1" end="3" step="1">
53          <electromagnet
54              spaces="rearsection_assembly/rs_solenoid[i]_assembly"
55              current="[rs_solenoid[i]_current]"
56          />
57      </loop>
58      <!-- rs solenoid booster -->
59      <electromagnet
60          spaces="rearsection_assembly/rs_solenoid_booster_assembly"
61          current="[rs_solenoid_booster_current]"
62      />
63      <!-- EGun solenoid -->
64      <electromagnet
65          spaces="rearsection_assembly/rs_EGun_solenoid_assembly"
66          current="[rs_EGun_solenoid_current]"
67      />
68      <!-- sc magnet system -->
69      <loop variable="i" start="1" end="2" step="1">
70          <electromagnet
71              spaces="rearsection_assembly/rscm_main_booster[i]_assembly"
72              current="[rscm_main_booster_current]"
73          />
74      </loop>
75      <electromagnet
76          spaces="rearsection_assembly/rscm_main_assembly"
77          current="[rscm_main_current]"
78      />
79      <!-- magnetic dipoles -->
80      <loop variable="i" start="1" end="2" step="1">
81          <electromagnet
82              spaces="rearsection_assembly/rs_magnetic_dipole[i]_top_assembly"
83              current="[rs_magnetic_dipole[i]_top_current]"
84          />
85          <electromagnet
86              spaces="rearsection_assembly/rs_magnetic_dipole[i]_bottom_assembly"
87              current="[rs_magnetic_dipole[i]_bottom_current]"
88          />
89          <electromagnet
90              spaces="rearsection_assembly/rs_magnetic_dipole[i]_front_assembly"
91              current="[rs_magnetic_dipole[i]_front_current]"
92          />
93          <electromagnet
```

```
94              spaces="rearsection_assembly/rs_magnetic_dipole[i]_rear_assembly"
95              current="[rs_magnetic_dipole[i]_rear_current]"
96          />
97      </loop>
98
99      <!-- electric potential values -->
100     <define name="rs_backplate_potential" value="-18600."/> <!-- -->
101     <external_define name="rs_frontplate_potential" value="-15000."/>
102     <define name="rs_ground_electrode_potential" value="0."/>
103     <external_define name="rs_postacc_electrode1_potential" value="-15000."/>
104     <external_define name="rs_postacc_electrode2_potential" value="-10000"/>
105     <external_define name="rs_postacc_electrode3_potential" value="-5000"/>
106     <define name="rs_dipole_electrode_front_potential" value="-200."/>
107     <define name="rs_dipole_electrode_rear_potential" value="200."/>
108
109     <!-- EGun plates -->
110     <!--
111     < electrostatic_dirichlet
112         name="rs_EGun_beamspot"
113         surfaces="rearsection_assembly/rs_egun_assembly/rs_egun_beamspot"
114         value="{[rs_backplate_potential]}"
115     />
116     < electrostatic_dirichlet
117         name="rs_EGun_goldcoating"
118         surfaces="rearsection_assembly/rs_egun_assembly/rs_egun_goldcoating"
119         value="{[rs_backplate_potential]}"
120     />
121     -->
122     < electrostatic_dirichlet
123         name="rs_EGun_backplate"
124         surfaces="rearsection_assembly/rs_egun_assembly/@rs_egun_backplate_system_tag"
125         value="{[rs_backplate_potential]}"
126     />
127     <!--
128         surfaces="rearsection_assembly/rs_egun_assembly/@rs_egun_backplate_system_tag"
129         surfaces="rearsection_assembly/rs_egun_assembly/rs_egun_backplate"
130     -->
131
132     < electrostatic_dirichlet
133         name="rs_EGun_frontplate"
134         surfaces="rearsection_assembly/rs_egun_assembly/rs_egun_frontplate"
135         value="{[ rs_frontplate_potential ]}"
136     />
137     <!-- ground electrode -->
138     < electrostatic_dirichlet
139         name="rs_ground_electrode"
140         surfaces="rearsection_assembly/rs_ground_assembly"
141         value="{[rs_ground_electrode_potential]}"
142     />
143     <!-- post acceleration electrodes -->
144     <loop variable="i" start="1" end="3" step="1">
145         < electrostatic_dirichlet
146             name="rs_postacc_electrode[i]"
147             surfaces="rearsection_assembly/rs_postacc_electrode[i]_assembly"
148             value="{[rs_postacc_electrode[i]_potential]}"
149         />
150     </loop>
151     <!-- electric dipoles -->
152     < electrostatic_dirichlet
```

```
153         name="rs_electricdipole_front_small1_pot"
154         surfaces="rearsection_assembly/rs_electricdipoles_assembly/
                rs_electricdipole_front_small1 "
155         value="{[ rs_dipole_electrode_front_potential ]}"
156     />
157     < electrostatic_dirichlet
158         name="rs_electricdipole_front_large_pot"
159         surfaces="rearsection_assembly/rs_electricdipoles_assembly/
                rs_electricdipole_front_large "
160         value="{[ rs_dipole_electrode_front_potential ]}"
161     />
162     < electrostatic_dirichlet
163         name="rs_electricdipole_front_small1_pot"
164         surfaces="rearsection_assembly/rs_electricdipoles_assembly/
                rs_electricdipole_front_small1 "
165         value="{[ rs_dipole_electrode_front_potential ]}"
166     />
167
168     < electrostatic_dirichlet
169         name="rs_electricdipole_rear_small1_pot"
170         surfaces="rearsection_assembly/rs_electricdipoles_assembly/
                rs_electricdipole_rear_small1 "
171         value="{[ rs_dipole_electrode_rear_potential ]}"
172     />
173     < electrostatic_dirichlet
174         name="rs_electricdipole_rear_large_pot"
175         surfaces="rearsection_assembly/rs_electricdipoles_assembly/
                rs_electricdipole_rear_large "
176         value="{[ rs_dipole_electrode_rear_potential ]}"
177     />
178     < electrostatic_dirichlet
179         name="rs_electricdipole_rear_small1_pot"
180         surfaces="rearsection_assembly/rs_electricdipoles_assembly/
                rs_electricdipole_rear_small1 "
181         value="{[ rs_dipole_electrode_rear_potential ]}"
182     />
183
184 </geometry>
```

APPENDIX C

REAR SECTION SIMULATION

```
<define name="log_path" value="@KSC_LOG_INSTALL_DIR@"/>
<define name="rearsection_config_path" value="@KSC_CONFIG_INSTALL_DIR@"/>
<external_define name="dps1r_flange_reference" value="{0.}"/> <!-- 4.73 -->
<external_define name="use_magnetic_dipoles_top_bottom" value="1" />
<external_define name="rs_egun_tilt_angle" value="{10.}"/> <!-- tilt angle of EGun in deg relative to z axis; the EGun is tilted around y axis with z=egun_position (center of front plate) -->
<external_define name="rs_frontplate_potential" value="-15000."/>
<external_define name="rs_postacc_electrode1_potential" value="-15000."/>
<external_define name="rs_postacc_electrode2_potential" value="-10000"/>
<external_define name="rs_postacc_electrode3_potential" value="-5000"/>
<external_define name="index" value=""/>
<external_define name="seed_value" value="51385"/>
<external_define name="n_events" value="1"/>
<external_define name="use_OpenCL" value="false"/>
<external_define name="use_CacheMatrixElements" value="[use_OpenCL]"/>

<messages>
    <file path="[log_path]" base="RearsectionSimulationLog_[index]_[rs_egun_tilt_angle]_[n_events]_[seed_value].txt"/>
    <message key="k_file" terminal="normal" log="warning"/>
    <message key="k_initialization" terminal="normal" log="warning"/>
    <message key="kg_core" terminal="normal" log="warning"/>
    <message key="kg_shape" terminal="normal" log="warning"/>
    <message key="kg_mesh" terminal="normal" log="warning"/>
    <message key="kg_axial_mesh" terminal="normal" log="warning"/>
    <message key="ks_object" terminal="normal" log="normal"/>
    <message key="ks_operator" terminal="normal" log="normal"/>
    <message key="ks_field" terminal="normal" log="normal"/>
    <message key="ks_generator" terminal="normal" log="normal"/>
    <message key="ks_trajectory" terminal="normal" log="normal"/>
    <message key="ks_interaction" terminal="normal" log="normal"/>
    <message key="ks_terminator" terminal="normal" log="normal"/>
    <message key="ks_writer" terminal="normal" log="normal"/>
    <message key="ks_navigator" terminal="normal" log="normal"/>
    <message key="ks_main" terminal="normal" log="normal"/>
    <message key="ks_run" terminal="normal" log="normal"/>
    <message key="ks_event" terminal="normal" log="normal"/>
    <message key="ks_track" terminal="normal" log="normal"/>
```

```
37      <message key="ks_step" terminal="normal" log="normal"/>
38  </messages>
39
40  <!-- include geometryEMD -->
41  <include name="[rearsection_config_path]/../TheBag/Rearsection/
        RearsectionExtendedGeometry.xml"/>
42  <include name="[rearsection_config_path]/../TheBag/Rearsection/DPS1-
        R_ExtendedGeometry.xml"/>
43
44  <geometry>
45      <!-- world cylinder space -->
46      <cylinder_space name="world_space" z1="-50" z2="50" r="20"/>
47      <!-- adiabatic cylinder space, if particle is in this space, it is tracked
            adiabatically -->
48      <cylinder_space name="adiabatic_trajectory_space" z1="-1.07" z2="15" r="19"/>
49      <!-- min_distance cylinder space, if particle is in this space, its minimum distance
            to the egun frontplate is calculated -->
50      <cylinder_space name="min_distance_frontplate_space" z1="-0.03" z2="0.01" r="1"/>
51      <!-- min_distance cylinder space, if particle is in this space, its minimum distance
            to the diaphragm is calculated -->
52      <cylinder_space name="min_distance_diaphragm_space" z1="-2.668" z2="-2.664" r="1
            "/>
53      <!-- assembling rearsection to world cylinder -->
54      <space name="world" node="world_space">
55          <space name="rearsection" tree="rearsection_assembly">
56              <transformation displacement="{0.} {0.} {[dps1r_flange_reference]}"/>
57          </space>
58          <space name="dps1-r" tree="dps1-r_assembly">
59              <transformation displacement="{0.} {0.} {[dps1r_flange_reference]}"/>
60          </space>
61          <space name="adiabatic_space" node="adiabatic_trajectory_space"/>
62          <space name="min_distance_space" tree="min_distance_frontplate_space">
63              <transformation displacement="{0.} {0.} {[dps1r_flange_reference]-4.58}"/>
64          </space>
65          <space name="min_distance_diaphragm" node="min_distance_diaphragm_space"/>
66      </space>
67
68      <!-- mesh -->
69      <mesh name="world_mesh" surfaces="world/#" spaces="world/#"/>
70  </geometry>
71
72  <kassiopeia>
73      <!-- fields -->
74      <!-- magnetic fields -->
75      <ksfield_electromagnet
76          name="magnetic_field"
77           file ="RearsectionMagnets.kbd"
78          system="world"
79          spaces="world/@magnet_tag"
80      >
81          <zonal_harmonic_field_solver
82              number_of_bifurcations="-1"
83              convergence_ratio=".99"
84              convergence_parameter="1.e-15"
85              proximity_to_sourcepoint="1.e-12"
86               number_of_central_coefficients ="500"
87               use_fractional_central_sourcepoint_spacing ="true"
88               central_sourcepoint_fractional_distance ="1e-2"
89              central_sourcepoint_spacing="1.e-2"
```

```
90              number_of_remote_coefficients="200"
91          />
92      </ksfield_electromagnet>
93
94      <!-- electric fields -->
95      < ksfield_electrostatic
96          name="electric_field"
97           file ="RearsectionChargeDensities_[index]_[ rs_egun_tilt_angle ]. kbd"
98          system="world"
99          surfaces="world/rearsection/@rs_electrode_tag"
100         symmetry="none"
101     >
102         <robin_hood_bem_solver
103         tolerance="1.e-12"
104         check_sub_interval="100"
105          display_interval ="1"
106         cache_matrix_elements="[use_CacheMatrixElements]"
107         use_opencl="[use_OpenCL]"
108         />
109         <!--<fast_multipole_bem_solver
110             tolerance="1.e-6"
111             krylov_solver_type="gmres"
112              restart_cycle_size ="30"
113              spatial_division ="3"
114             expansion_degree="4"
115             neighbor_order="1"
116             maximum_tree_depth="5"
117             region_expansion_factor="2"
118              use_region_size_estimation ="true"
119             use_caching="true"
120             use_opencl="[use_OpenCL]"
121             use_vtk="true"
122         /> -->
123         < fast_multipole_field_solver
124              spatial_division ="3"
125             expansion_degree="9"
126             neighbor_order="1"
127             maximum_tree_depth="5"
128             region_expansion_factor="3"
129              use_region_size_estimation ="true"
130             use_caching="true"
131             use_opencl="[use_OpenCL]"
132         />
133         <!--integrating_field_solver
134             use_opencl="[use_OpenCL]"
135         /-->
136         <!--zonal_harmonic_field_solver
137             number_of_bifurcations="-1"
138             convergence_ratio=".99"
139             convergence_parameter="1.e-15"
140             proximity_to_sourcepoint="1.e-12"
141              number_of_central_coefficients ="500"
142              use_fractional_central_sourcepoint_spacing ="true"
143              central_sourcepoint_fractional_distance ="1e-2"
144             central_sourcepoint_spacing="1e-3"
145                     number_of_remote_coefficients="200"
146         /> -->
147     </ ksfield_electrostatic >
148
```

```
149     <!-- generators -->
150     <!-- EGun generators -->
151     <external_define name="rs_egun_starting_fiber" value="world/@rs_egun_fiber_0_tag"/>
152     <external_define name="rs_egun_starting_radius" value="{100.e-6}"/>
153         <!-- fix values -->
154         <ksgen_generator_composite name="generator_egun_fix">
155             <position_rectangular_composite surface="[rs_egun_starting_fiber]">
156                 <x_fix value="0."/>
157                 <y_fix value="0."/>
158                 <z_fix value="{1.e-8}"/>
159             </position_rectangular_composite>
160             <direction_spherical_composite surface="[rs_egun_starting_fiber]">
161                 <theta_fix value="20."/>
162                 <phi_fix value="0."/>
163             </direction_spherical_composite>
164             <energy_composite>
165                 <energy_fix value="0.15"/>
166             </energy_composite>
167             <time_composite>
168                 <time_fix value="0."/>
169             </time_composite>
170         </ksgen_generator_composite>
171 
172         <!-- monte carlo values -->
173         <ksgen_generator_composite name="generator_egun_MC">
174             <position_cylindrical_composite surface="[rs_egun_starting_fiber]">
175                 <r_cylindrical radius_min="0." radius_max="[rs_egun_starting_radius]"/>
176                 <phi_uniform value_min="0." value_max="360."/>
177                 <z_gauss value_min="{1.e-9}" value_max="{1.e-7}" value_mean="{1.e-8}
                        " value_sigma="{2.e-8}"/>
178             </position_cylindrical_composite>
179             <direction_spherical_composite surface="[rs_egun_starting_fiber]">
180                 <theta_spherical angle_min="0." angle_max="90"/>
181                 <phi_uniform value_min="0." value_max="360."/>
182             </direction_spherical_composite>
183             <energy_composite>
184                 <energy_gauss value_min="0." value_max="0.4" value_mean="0.15"
                        value_sigma="0.075"/>
185             </energy_composite>
186             <time_composite>
187                 <time_fix value="0."/>
188             </time_composite>
189         </ksgen_generator_composite>
190 
191     <!-- trajectories -->
192     <kstraj_trajectory_exact name="trajectory_exact_EGun">
193         <interpolator_fast name="interpolator_fast"/>
194         <integrator_rk8 name="integrator_rk8"/>
195         <term_propagation name="term_propagation"/>
196         <control_length name="trajectory_step_length" length="0.0005"/>
197     </kstraj_trajectory_exact>
198     <kstraj_trajectory_exact name="trajectory_exact">
199         <interpolator_fast name="interpolator_fast"/>
200         <integrator_rk8 name="integrator_rk8"/>
201         <term_propagation name="term_propagation"/>
202     </kstraj_trajectory_exact>
203     <kstraj_trajectory_adiabatic name="trajectory_adiabatic">
204         <integrator_rk8 name="integrator_rk8"/>
205         <term_propagation name="term_propagation"/>
```

```
206         <term_drift name="term_drift"/>
207         <term_gyration name="term_gyration"/>
208         <control_cyclotron name="control_cyclotron" fraction="{10. / 1.}"/>
209     </kstraj_trajectory_adiabatic>
210     <!-- <kstraj_magnetic_trajectory name="magnetic_trajectory"/> -->
211     <!-- <kstraj_control_length name="trajectory_step_length" length="0.005"/> -->
212     <kstraj_control_cyclotron name="control_cyclotron_1_4" fraction="{1. / 4.}"/>
213     <kstraj_control_cyclotron name="control_cyclotron_1_8" fraction="{1. / 8.}"/>
214     <kstraj_control_cyclotron name="control_cyclotron_1_16" fraction="{1. / 16.}"/>
215     <kstraj_control_cyclotron name="control_cyclotron_1_32" fraction="{1. / 32.}"/>
216     <kstraj_control_cyclotron name="control_cyclotron_1_64" fraction="{1. / 64.}"/>
217     <kstraj_control_cyclotron name="control_cyclotron_1_128" fraction="{1. / 128.}"/>
218     <kstraj_control_cyclotron name="control_cyclotron_1_256" fraction="{1. / 256.}"/>
219     <kstraj_control_cyclotron name="control_cyclotron_1_512" fraction="{1. / 512.}"/>
220
221     <external_define name="term_max_z_value" value="0.66261" />
222     <!-- terminators -->
223     <ksterm_death name="term_death"/>
224     <ksterm_max_steps name="term_max_steps" steps="20485760"/> <!-- 2048576 -->
225     <ksterm_max_z name="term_max_z" z="[term_max_z_value]"/> <!-- 0.66261 -->
226     <ksterm_min_z name="term_min_z" z="-4.7"/>
227     <ksterm_min_distance name="term_min_distance_frontplate" surfaces="world/
          @rs_egun_frontplate_tag" min_distance="50.e-6"/>
228     <!-- ksterm_min_distance name="term_min_distance_backplate" surfaces="world/
          @rs_egun_backplate_tag" min_distance="9.e-10"/-->
229     <!-- ksterm_min_distance name="term_min_distance_diaphragm" surfaces="world/
          @rs_diaphragm_tag" min_distance="10.e-6"/-->
230     <ksterm_min_distance name="term_min_distance_all" surfaces="world/@all_tag"
          min_distance="50.e-6"/>
231
232     <!-- output -->
233     <include name="[rearsection_config_path]/Katrin/RearsectionOutput.xml"/>
234     <kswrite_root name="write_root" base="RearsectionSimulation_[index]_[
          rs_egun_tilt_angle]_[n_events]_[seed_value].root"/>
235     <!--kswrite_vtk name="write_vtk" base="RearsectionSimulation_[index]_[n_events]_[
          seed_value]"/-->
236
237     <!-- space navigators -->
238     <ksnav_space name="nav_space" enter_split="false" exit_split="false" tolerance="1.e-6
          "/> <!-- 1.e-6 -->
239
240     <!-- surface navigators -->
241     <ksnav_surface name="nav_surface" transmission_split="true" reflection_split ="false"/
          >
242
243     <!-- navigation structure -->
244     <ksgeo_space name="command_world_group" spaces="world">
245         <command parent="root_terminator" field="add_terminator" child="
              term_max_steps"/>
246         <command parent="root_terminator" field="add_terminator" child="term_min_z"/>
247         <command parent="root_terminator" field="add_terminator" child="term_max_z"/
              >
248         <command parent="root_terminator" field="add_terminator" child="
              term_min_distance_all"/>
249         <command parent="write_root" field="add_track_output" child="
              component_track_world"/>
250         <!--command parent="write_root" field="add_step_output" child="
              component_step_world"/-->
```

```
251         <!--command parent="write_vtk" field="set_step_point" child="
                component_step_position"/-->
252         <!--command parent="write_vtk" field="set_step_data" child="
                component_step_length"/-->
253         <command parent="root_trajectory" field="set_trajectory" child="trajectory_exact"
                />
254             <command parent="trajectory_exact" field="add_control" child="
                    control_cyclotron_1_16"/>
255
256         <!--geo_space name="egun_tracking" spaces="world/rearsection/rs_egun_assembly
                ">
257             <command parent="trajectory_exact" field="remove_control" child="
                    control_cyclotron_1_16"/>
258             <command parent="trajectory_exact" field="add_control" child="
                    control_cyclotron_1_256"/>
259         </geo_space-->
260         <geo_space name="adiabatic_tracking" spaces="world/adiabatic_space">
261             <command parent="root_trajectory" field="clear_trajectory" child="
                    trajectory_exact"/>
262             <command parent="root_trajectory" field="set_trajectory" child="
                    trajectory_adiabatic"/>
263         </geo_space>
264         <geo_space name="min_distance" spaces="world/min_distance_space">
265             <command parent="trajectory_exact" field="remove_control" child="
                    control_cyclotron_1_16"/>
266             <command parent="trajectory_exact" field="add_control" child="
                    control_cyclotron_1_128"/>
267             <command parent="root_terminator" field="add_terminator" child="
                    term_min_distance_frontplate"/>
268             <command parent="write_root" field="add_step_output" child="
                    component_step_min_distance"/>
269         </geo_space>
270         <geo_space name="min_distance_diaphragm_nav" spaces="world/
                min_distance_diaphragm">
271             <command parent="trajectory_exact" field="remove_control" child="
                    control_cyclotron_1_16"/>
272             <command parent="trajectory_exact" field="add_control" child="
                    control_cyclotron_1_128"/>
273             <command parent="root_terminator" field="add_terminator" child="
                    term_min_distance_diaphragm"/>
274             <!--command parent="write_root" field="add_step_output" child="
                    component_step_min_distance_diaphragm"/-->
275         </geo_space>
276
277         <geo_surface name="surface_death" surfaces="world/#" spaces="world/@all_tag">
278             <command parent="root_terminator" field="add_terminator" child="
                    term_death"/>
279         </geo_surface>
280     </ksgeo_space>
281
282     <!-- simulation -->
283     <ks_simulation
284         name="rearsection_simulation"
285         run="1"
286         seed="[seed_value]"
287         events="[n_events]"
288         magnetic_field="magnetic_field"
289          electric_field =" electric_field "
290         space="command_world_group"
```

```
291             generator="generator_egun_MC"
292
293             space_navigator="nav_space"
294             surface_navigator="nav_surface"
295             writer="write_root"
296             />
297
298 </kassiopeia>
```

APPENDIX D

REAR SECTION SETTINGS

Table D.1.: **Rear Section simulation performance tests** - Different GPU tracking configurations of KASSIOPEIA, fixed generator ($\alpha = 10°$, $\theta_{\text{start}} = 20°$, $\Delta U = 3.6\,\text{keV}$, fiberID=0, tracking until the mid of the first WGTS magnet)

method	EGun space	world	adiabatic	time CPU	time GPU	total steps
FFTM	1/256	1/16	10	-	18 s	5000
FFTM	1/128	1/16	10	-	16 s	4917
FFTM	1/64	1/16	10	-	15 s	4878
FFTM	1/32	1/16	10	-	15 s	4852
FFTM	1/16	1/16	10	-	15 s	4827
FFTM	1/16	1/16	-	-	2 : 44 min	57448
FFTM	1/32	1/32	-	-	5 : 23 min	116013
4 FFTM	1/256	1/16	10	-	1 : 14 min	4884
3 FFTM	1/256	1/16	10	-	1 : 00 min	ca 5000

Table D.2.: **Rear Section settings for** $\alpha = 15°$ - Electrostatic settings of the Rear Section with the corresponding θ_{WGTS} for $\alpha = 15°$. Simulated are 1000 electrons; if the number of electrons reaching the WGTS is lower than this value, the missing electrons hit the diaphragm or the E-gun frontplate. Some of the electrons are also reflected and afterwards removed at the diaphragm or the E-gun frontplate. The potential of the E-gun back plate is kept constant at $-18600\,\mathrm{V}$, whereas the front plate potential U_1 is varied to fulfill the plate potential difference. Accordingly, the post acceleration electrodes $U_{2,3}$ are varied to enable equidistant potential differences on the acceleration steps.

α (°)	ΔU (V)	U_1 (V)	U_2 (V)	U_3 (V)	Fiber ID	θ_{WGTS} (°)	$\sigma_{\theta_{\mathrm{WGTS}}}$ (°)	e^-_{WGTS}	$e^-_{\mathrm{reflected}}$	$e^-_{\mathrm{non\text{-}reflected}}$
15	2100	-16500	-11500	-5500	0	50.9535	1.83265	426	0	574
15	2100	-16500	-11500	-5500	1	47.2293	0.689761	432	0	568
15	2100	-16500	-11500	-5500	2	44.4472	1.83123	976	0	54
15	2100	-16500	-11500	-5500	3	38.0233	1.19039	860	0	140
15	2300	-16300	-10866	-5433	0	-	-	0	0	1000
15	2300	-16300	-10866	-5433	1	-	-	0	0	1000
15	2300	-16300	-10866	-5433	2	-	-	0	0	1000
15	2300	-16300	-10866	-5433	3	40.8331	0.552472	68	0	932
15	2600	-16000	-10666	-5333	0	60.5661	0.0647488	2	614	384
15	2600	-16000	-10666	-5333	1	59.6548	0.67684	138	95	767
15	2600	-16000	-10666	-5333	2	57.409	1.59798	719	35	246
15	2600	-16000	-10666	-5333	3	51.0342	0.782747	417	0	583

Table D.3.: **Rear Section settings for** $\alpha = 10°$ - Electrostatic settings of the Rear Section with the corresponding θ_{WGTS} for $\alpha = 10°$. Simulated are 1000 electrons; if the number of electrons reaching the WGTS is lower than this value, the missing electrons hit the diaphragm or the E-gun frontplate. Some of the electrons are also reflected and afterwards removed at the diaphragm or the E-gun frontplate. The potential of the E-gun back plate is kept constant at $-18600\,\mathrm{V}$, whereas the front plate potential U_1 is varied to fulfill the plate potential difference. Accordingly, the post acceleration electrodes $U_{2,3}$ are varied to enable equidistant potential differences on the acceleration steps.

α (°)	ΔU (V)	U_1 (V)	U_2 (V)	U_3 (V)	Fiber ID	θ_{WGTS} (°)	$\sigma_{\theta_{\mathrm{WGTS}}}$ (°)	e^-_{WGTS}	$e^-_{\mathrm{reflected}}$	$e^-_{\mathrm{non\text{-}reflected}}$
10	3600	-15000	-10000	-5000	0	48.2581	1.23566	231	0	769
10	3600	-15000	-10000	-5000	1	43.6477	1.92911	1000	0	0
10	3600	-15000	-10000	-5000	2	45.1346	2.21043	990	0	10
10	3600	-15000	-10000	-5000	3	39.1872	2.02446	1000	0	0
10	3800	-14800	-9866	-4933	0	52.4126	2.69158	817	0	183
10	3800	-14800	-9866	-4933	1	45.3546	2.19066	994	0	6
10	3800	-14800	-9866	-4933	2	47.12	1.98753	974	0	26
10	3800	-14800	-9866	-4933	3	40.9528	1.62979	1000	0	0
10	4100	-14500	-9666	-4833	0	-	-	0	0	1000
10	4100	-14500	-9666	-4833	1	-	-	0	0	1000
10	4100	-14500	-9666	-4833	2	-	-	0	0	1000
10	4100	-14500	-9666	-4833	3	45.0884	1.97759	1000	0	0
10	4400	-14200	-9466	-4733	0	-	-	0	0	1000

Continued on next page

123

Continued from previous page

10	4400	-14200	-9466	-4733	1	48.57	0.51578	18	0	982
10	4400	-14200	-9466	-4733	2	52.5807	1.44987	259	0	741
10	4400	-14200	-9466	-4733	3	49.3401	2.09059	1000	0	0
10	4500	-14100	-9400	-4700	0	-	-	0	0	1000
10	4500	-14100	-9400	-4700	1	53.4211	2.18936	884	0	116
10	4500	-14100	-9400	-4700	2	56.3368	2.13395	813	54	133
10	4500	-14100	-9400	-4700	3	50.341	2.67234	1000	0	0
10	4600	-14000	-9333	-4666	0	59.4696	0.750724	145	35	820
10	4600	-14000	-9333	-4666	1	54.5269	2.96975	936	0	64
10	4600	-14000	-9333	-4666	2	57.6376	2.31801	751	59	190
10	4600	-14000	-9333	-4666	3	51.1838	2.25275	1000	0	0

Table D.4.: **Rear Section settings for** $\alpha = 7°$ - Electrostatic settings of the Rear Section with the corresponding θ_{WGTS} for $\alpha = 7°$. Simulated are 1000 electrons; if the number of electrons reaching the WGTS is lower than this value, the missing electrons hit the diaphragm or the E-gun frontplate. Some of the electrons are also reflected and afterwards removed at the diaphragm or the E-gun frontplate. The potential of the E-gun back plate is kept constant at $-18600\,\mathrm{V}$, whereas the front plate potential U_1 is varied to fulfill the plate potential difference. Accordingly, the post acceleration electrodes $U_{2,3}$ are varied to enable equidistant potential differences on the acceleration steps.

α (°)	ΔU (V)	U_1 (V)	U_2 (V)	U_3 (V)	Fiber ID	θ_{WGTS} (°)	$\sigma_{\theta_{\mathrm{WGTS}}}$ (°)	e^-_{WGTS}	$e^-_{\mathrm{reflected}}$	$e^-_{\mathrm{non\text{-}reflected}}$
7	6600	-12000	-8000	-4000	0	-	-	0	0	1000
7	6600	-12000	-8000	-4000	1	-	-	0	0	1000
7	6600	-12000	-8000	-4000	2	48.7548	2.08954	964	0	36
7	6600	-12000	-8000	-4000	3	46.5031	2.15705	1000	0	0
7	7100	-11500	-7666	-3833	0	-	-	0	0	1000
7	7100	-11500	-7666	-3833	1	46.3314	2.66944	993	0	7
7	7100	-11500	-7666	-3833	2	52.8194	2.3506	963	0	37
7	7100	-11500	-7666	-3833	3	50.6056	2.47188	1000	0	0
7	7600	-11000	-7333	-3666	0	56.114	2.60977	591	139	270
7	7600	-11000	-7333	-3666	1	48.4605	2.4885	988	0	12
7	7600	-11000	-7333	-3666	2	55.149	2.7358	859	34	107
7	7600	-11000	-7333	-3666	3	53.3537	2.48097	997	1	2

125

LIST OF FIGURES

2.1. Standard Model of particle physics 5
2.2. Neutrino mass hierarchy 11
2.3. Double beta decay spectrum 14
2.4. Example β-decay spectrum 18

3.1. Overview of the KATRIN experiment 23
3.2. MAC-E filter principle 25
3.3. Transmission function 27

4.1. CAD half cut of the Rear Section 33
4.2. Half cut schema of the Rear Section 34
4.3. Rear Section geometry in KASSIOPEIA 34
4.4. Magnetic field of the Rear Section 35
4.5. Electric potential and electric field of the Rear Section 36
4.6. Trapped electron removal 38
4.7. Quarter cut of Rear Section geometry in KASSIOPEIA 39
4.8. Example meshing and aspect ratio 42
4.9. Monte Carlo distribution of the initial parameters 44
4.10. Polar angle to z in WGTS θ_{WGTS} 47
4.11. Tracking configuration 48
4.12. Optimum starting positions of the electrons for selected E-gun pitch angles 51
4.13. Optical fiber positioning due to optimum starting position 52
4.14. Visualization of different configurations 54

5.1. Energy density distribution of CMB and Cνb 58
5.2. Relic neutrino overdensity in the Milky Way 64
5.3. Effect of Z bursts in UHECR spectra 66
5.4. Torsion oscillator 67
5.5. Example induced β-decay spectrum 68
5.6. Relic neutrino capture spectra with FSD and Doppler effect on/off . . 71
5.7. Final states of the tritium daughter molecules 77
5.8. Log likelihood comparison 79
5.9. Relic neutrino capture spectra on top of the tritium β-decay spectrum 80

5.10. Upper limit on the relic neutrino overdensity depending on background and neutrino mass 81
5.11. Sensitivity of KATRIN for the relic neutrino overdensity depending on the used MTD 82
5.12. Systematic shifts caused by high voltage fluctuations 84
5.13. Ensemble test limit 86

LIST OF TABLES

2.1. Experimental results of the neutrino oscillation parameters 9

4.1. Requirements for the Rear Section of the KATRIN experiment 32
4.2. Results of the Rear Section simulation performance tests 49
4.3. Optical fiber positions and IDs 53
4.4. Rear Section settings to achieve $\theta_{\mathrm{WGTS}} \approx 51^{\circ}$ 55

5.1. Cosmological proportionalities 59
5.2. Reevaluated neutrino mass sensitivity 83

D.1. Rear Section simulation performance tests 121
D.2. Rear Section settings for $\alpha = 15^{\circ}$ 122
D.3. Rear Section settings for $\alpha = 10^{\circ}$ 123
D.4. Rear Section settings for $\alpha = 7^{\circ}$ 125

BIBLIOGRAPHY

[A+01] Ahmad, Q. R. et al.: Measurement of the rate of $\nu_e + d \rightarrow p + p + e^-$ interactions produced by ^8B solar neutrinos at the Sudbury Neutrino Observatory. In: *Phys.Rev.Lett.* 87 (2001), S. 071301. http://dx.doi.org/10.1103/PhysRevLett.87.071301. – DOI 10.1103/PhysRevLett.87.071301

[AAA+13] Aprile, E. ; Alfonsi, M. ; Arisaka, K. ; Arneodo, F. et al.: Limits on Spin-Dependent WIMP-Nucleon Cross Sections from 225 Live Days of XENON100 Data. In: *Phys. Rev. Lett.* 111 (2013), Jul, 021301. http://dx.doi.org/10.1103/PhysRevLett.111.021301. – DOI 10.1103/PhysRevLett.111.021301

[ABB+11] Antcheva, I. ; Ballintijn, M. ; Bellenot, B. ; Biskup, M. ; Brun, Rene ; Buncic, N. ; Canal, Ph. ; Casadei, D. ; Couet, O. ; Fine, V. et al.: ROOT – A C++ framework for petabyte data storage, statistical analysis and visualization. In: *Computer Physics Communications* 182 (2011), Nr. 6, S. 1384–1385

[ABD+96] Assamagan, K. ; Brönnimann, Ch. ; Daum, M. ; Forrer, H. ; Frosch, R. ; Gheno, P. ; Horisberger, R. ; Janousch, M. ; Kettle, P.-R. ; Spirig, Th. et al.: Upper limit of the muon-neutrino mass and charged-pion mass from momentum analysis of a surface muon beam. In: *Physical Review D* 53 (1996), Nr. 11, S. 6065

[Ade14] Ade, P. et al. (Planck Collaboration): Planck 2013 results. XVI. Cosmological parameters. In: *Astronomy and Astrophysics* (2014). http://dx.doi.org/10.1051/0004-6361/201321591. – DOI 10.1051/0004–6361/201321591

[Ago13] Agostini, M. et al. (GERDA Collaboration): Results on Neutrinoless Double-β Decay of ^{76}Ge from Phase I of the GERDA Experiment. In: *Physical Review Letters* 111 (2013), S. 122503. http://dx.doi.org/10.1103/PhysRevLett.111.122503. – DOI 10.1103/PhysRevLett.111.122503

[ATL12] ATLAS Collaboration: Observation of a new particle in the search for the Standard Model Higgs boson with the ATLAS detector at the LHC.

In: *Phys.Lett.* B716 (2012), S. 1–29. http://dx.doi.org/10.1016/j.physletb.2012.08.020. – DOI 10.1016/j.physletb.2012.08.020

[B+98] Barate, R. et al.: An upper limit on the τ neutrino mass from three-and five-prong tau decays. In: *The European Physical Journal C-Particles and Fields* 2 (1998), Nr. 3, S. 395–406

[B+13] Babutzka, M. et al.: KATRIN Rear Section Technical Design Document / KATRIN rear section working group. 2013. – Forschungsbericht

[Bab14] Babutzka, M.: *Design and development for the Rearsection of the KATRIN experiment*, Karlsruher Institut für Technologie (KIT), Diss., 2014

[BBB+87] Bionta, R. M. ; Blewitt, G. ; Bratton, C. B. ; Casper, D. ; Ciocio, A. ; Claus, R. ; Cortez, B. ; Crouch, M. ; Dye, S. T. ; Errede, S. et al.: Observation of a neutrino burst in coincidence with supernova 1987A in the Large Magellanic Cloud. In: *Physical Review Letters* 58 (1987), Nr. 14, S. 1494

[BBC+13] Betts, S. ; Blanchard, W. R. ; Carnevale, R. H. et al.: Development of a Relic Neutrino Detection Experiment at PTOLEMY: Princeton Tritium Observatory for Light, Early-Universe, Massive-Neutrino Yield. In: *ArXiv e-prints* (2013), july

[Ber12] Beringer, J. et al. (Particle Data Group): Review of Particle Physics. In: *Physical Review D* 86 (2012), S. 010001. http://dx.doi.org/10.1103/PhysRevD.86.010001. – DOI 10.1103/PhysRevD.86.010001

[BFFP86] Blumenthal, G. R. ; Faber, S. M. ; Flores, R. ; Primack, J. R.: Contraction of dark matter galactic halos due to baryonic infall. In: *The Astrophysical Journal* 301 (1986), S. 27–34

[BG97] Beatson, R. ; Greengard, L.: A short course on fast multipole methods. In: *Wavelets, multilevel methods and elliptic PDEs* 1 (1997), 1–37. https://math.berkeley.edu/~strain/273.F10/beatson.greengard.short.course.fmm.pdf

[BLM10] Bahr, M. ; Leber, M. ; Monreal, B.: *Simulations for the Post-acceleration Electron Gun for the KATRIN Rear System*. September 2010. – Department of Physics, University of California, Santa Barbara, CA

[BP34] Bethe, H. ; Peierls, R.: The "neutrino". In: *Nature* 133 (1934), S. 532

[CGR99] Cheng, H. ; Greengard, L. ; Rokhlin, V.: A fast adaptive multipole algorithm in three dimensions. In: *Journal of Computational Physics* 155 (1999), Nr. 2, 468–498. http://www.sciencedirect.com/science/article/pii/S0021999199963556

[Cha14] Chadwick, J.: Intensitätsverteilung im magnetischen Spectrum der β-Strahlen von Radium B + C. In: *Verhandl. d. Dtsch. Phys. Ges.* 16 (1914), S. 383

[Cha32] Chadwick, J.: The Existence of a Neutron. In: *Proceedings of the Royal Society of London. Series A* 136 (1932), Nr. 830, 692-708. http://dx.doi.org/10.1098/rspa.1932.0112. – DOI 10.1098/rspa.1932.0112

[CMM07] Cocco, A. G. ; Mangano, G. ; Messina, M.: Probing low energy neutrino backgrounds with neutrino capture on beta decaying nuclei. In: *Journal of Cosmology and Astroparticle Physics* 2007 (2007), Nr. 06, 015. http://stacks.iop.org/1475-7516/2007/i=06/a=015

[CMS12] CMS Collaboration: Observation of a new boson at a mass of 125 GeV with the CMS experiment at the LHC. In: *Phys.Lett.* B716 (2012), S. 30–61. http://dx.doi.org/10.1016/j.physletb.2012.08.021. – DOI 10.1016/j.physletb.2012.08.021

[Cor14] Corona, T. J.: *Methodology and Application of High Performance Electrostatic Field Simulation in the KATRIN Experiment*, UNC Chapel Hill, Diss., 2014

[Cou14] Courville, G.: *personal communication*. February 2014

[D+89] Decamp, D. et al.: Determination of the Number of Light Neutrino Species. In: *Phys.Lett.* B231 (1989), S. 519. http://dx.doi.org/10.1016/0370-2693(89)90704-1. – DOI 10.1016/0370–2693(89)90704–1

[DGG+62] Danby, G. ; Gaillard, J.-M. ; Goulianos, K. ; Lederman, L. M. ; Mistry, N. ; Schwartz, M. ; Steinberger, J.: Observation of High-Energy Neutrino Reactions and the Existence of Two Kinds of Neutrinos. In: *Phys. Rev. Lett.* 9 (1962), Jul, 36–44. http://dx.doi.org/10.1103/PhysRevLett.9.36. – DOI 10.1103/PhysRevLett.9.36

[DHH68] Davis, R. ; Harmer, Don S. ; Hoffman, Kenneth C.: Search for Neutrinos from the Sun. In: *Phys. Rev. Lett.* 20 (1968), May, 1205–1209. http://dx.doi.org/10.1103/PhysRevLett.20.1205. – DOI 10.1103/PhysRevLett.20.1205

[E+04] Eidelman, S. et al.: Review of Particle Physics. In: *Physics Letters B* 592 (2004), Nr. 1-4, 1-5. http://dx.doi.org/10.1016/j.physletb.2004.06.001. – DOI 10.1016/j.physletb.2004.06.001. – ISSN 0370–2693. – Review of Particle Physics

[Ein05] Einstein, A.: Über einen die Erzeugung und Verwandlung des Lichtes betreffenden heuristischen Gesichtspunkt. In: *Annalen der Physik* 322 (1905), Nr. 6, S. 132–148

[F+98] Fukuda, Y. et al.: Evidence for oscillation of atmospheric neutrinos. In: *Phys.Rev.Lett.* 81 (1998), S. 1562–1567. http://dx.doi.org/10.1103/PhysRevLett.81.1562. – DOI 10.1103/PhysRevLett.81.1562

[F+12] Formaggio, J. et al.: Solving for micro- and macro-scale electrostatic configurations using the Robin Hood algorithm. In: *Progress in Electromagnetics Research B* 39 (2012), Nr. 1

[Fäs14] Fässler, Amand: *personal communication*. April 2014

[Fer34] Fermi, E.: Versuch einer Theorie der β-Strahlen. In: *Zeitschrift für Physik* 88 (1934), Nr. 3–4, S. 161–177. http://dx.doi.org/10.1007/BF01351864. – DOI 10.1007/BF01351864

[FG+15] Furse, D. ; Groh, S. et al.: *Kassiopeia: A Modern, Extensible C++ Particle Tracking Package*. 2015. – to be published

[FHKŠ11] Fässler, A. ; Hodak, R. ; Kovalenko, S. ; Šimkovic, F.: Tritium and rhenium as a probe of cosmic neutrino background. In: *J.Phys.* G38 (2011), S. 075202. http://dx.doi.org/10.1088/0954-3899/38/7/075202. – DOI 10.1088/0954–3899/38/7/075202

[FHKŠ13] Fässler, A. ; Hodak, R. ; Kovalenko, S. ; Šimkovic, F.: Search for the Cosmic Neutrino Background and KATRIN. In: *Rom.J.Phys.* 58 (2013), Nr. 9-10, S. 1221–1231

[FHKŠ14] Fässler, A. ; Hodak, R. ; Kovalenko, S. ; Šimkovic, F.: Beta Decay and the Cosmic Neutrino Background. In: *EPJ Web of Conferences* Bd. 71 EDP Sciences, 2014, S. 00044

[Fis14] Fischer, S.: *Commissioning of the KATRIN Raman system and durability studies of optical coatings in glove box and tritium atmospheres*, Karlsruher Institut für Technologie (KIT), Diss., 2014. http://nbn-resolving.org/urn:nbn:de:swb:90-436973

[FKR02] Fodor, Z. ; Katz, S. D. ; Ringwald, A.: Determination of Absolute Neutrino Masses from Bursts of Z Bosons in Cosmic Rays. In: *Phys. Rev. Lett.* 88 (2002), Apr, 171101. http://dx.doi.org/10.1103/PhysRevLett.88.171101. – DOI 10.1103/PhysRevLett.88.171101

[Fur39] Furry, W. H.: On transition probabilities in double beta-disintegration. In: *Physical Review* 56 (1939), Nr. 12, S. 1184

[Fur15] Furse, D., MIT, Diss., 2015. – in preparation

[GGP+06] Gatti, F. ; Gallinaro, G. ; Pergolesi, D. ; Repetto, P. ; Ribeiro-Gomez, M. ; Kelley, R. ; Kilbourne, C. A. ; Porter, F. S. ; Enss, C. ; Fleischmann, A. et al.: Microcalorimeter Arrays for a Rhenium Experiment. (2006). http://pessina.mib.infn.it/Biblio/Biblio_Articoli/proposal_MARE_v2.6.pdf

[GGS58] Goldhaber, M. ; Grodzins, L. ; Sunyar, A. W.: Helicity of Neutrinos. In: *Phys. Rev.* 109 (1958), Feb, 1015–1017. http://dx.doi.org/10.1103/PhysRev.109.1015. – DOI 10.1103/PhysRev.109.1015

[Glü11] Glück, F.: Axisymmetric Magnetic Field Calculation with Zonal Harmonic Expansion. In: *Progress In Electromagnetics Research B* 32 (2011), S. 351–388. http://dx.doi.org/10.2528/PIERB11042108. – DOI 10.2528/PIERB11042108

[GR87] Greengard, L. ; Rokhlin, V.: A fast algorithm for particle simulations. In: *Journal of computational physics* 73 (1987), Nr. 2, 325–348. http://www.sciencedirect.com/science/article/pii/0021999187901409

[Gro15] Groh, S.: *Global Tracking of Electrons and Transmission properties of the KATRIN Experiment*, Karlsruher Institut für Technologie (KIT), Diss., 2015. – in preparation

[Hag99] Hagmann, C.: A relic neutrino detector. In: *arXiv preprint astro-ph/9902102* (1999)

[HKK+88] Hirata, K. S. ; Kajita, T. ; Koshiba, M. ; Nakahata, M. ; Oyama, Y. ; Sato, N. ; Suzuki, A. ; Takita, M. ; Totsuka, Y. ; Kifune, T. et al.: Observation in the Kamiokande-II detector of the neutrino burst from supernova SN1987A. In: *Physical Review D* 38 (1988), Nr. 2, S. 448

[HM05] Hwang, W.-Y. P. ; Ma, B.-Q.: Detection of cosmic neutrino clustering by cosmic ray spectra. In: *New Journal of Physics* 7 (2005), Nr. 1, 41. http://stacks.iop.org/1367-2630/7/i=1/a=041

[Höt12] Hötzel, M.: *Simulation and analysis of source-related effects for KATRIN*, Karlsruher Institut für Technologie (KIT), Diss., 2012. http://digbib.ubka.uni-karlsruhe.de/volltexte/1000031259

[Hug08] Hugenberg, K.: *Design of the electrode system of the KATRIN main spectrometer*, Westfälische Wilhelms-Universität Münster, Diploma Thesis, 2008. http://www.uni-muenster.de/Physik.KP/AGWeinheimer/theses/Diplom_Karen_Hugenberg.pdf

[Jac62] Jackson, J. D.: *Classical electrodynamics*. Bd. 3. John Wiley & Sons, Inc., 1962

[JKG96] Jungman, G. ; Kamionkowski, M. ; Griest, K.: Supersymmetric dark matter. In: *Physics Reports* 267 (1996), Nr. 5, 195–373. http://dx.doi.org/http://dx.doi.org/10.1016/0370-1573(95)00058-5. – DOI http://dx.doi.org/10.1016/0370–1573(95)00058–5

[JR75] James, F. ; Roos, M.: Minuit-a system for function minimization and analysis of the parameter errors and correlations. In: *Computer Physics Communications* 10 (1975), Nr. 6, 343–367. http://www.sciencedirect.com/science/article/pii/0010465575900399

[K+01] Kodama, K. et al.: Observation of tau neutrino interactions. In: *Phys.Lett.* B504 (2001), S. 218–224. http://dx.doi.org/10.1016/S0370-2693(01)00307-0. – DOI 10.1016/S0370–2693(01)00307–0

[Kab12] Kaboth, A. C.: *Detecting the invisible universe with neutrinos and dark matter*, Massachusetts Institute for Technology (MIT), Diss., 2012. http://hdl.handle.net/1721.1/76980

[Käf12] Käfer, W.: *Sensitivity studies of the KATRIN experiment*, Karlsruher Institut für Technologie (KIT), Diss., 2012. http://digbib.ubka.uni-karlsruhe.de/volltexte/1000026021

[KAT05] KATRIN collaboration: KATRIN Design Report. In: *FZKA scientific report* 7090 (2005). http://bibliothek.fzk.de/zb/berichte/FZKA7090.pdf

[KFM10] Kaboth, A. ; Formaggio, J. A. ; Monreal, B.: Sensitivity of neutrino mass experiments to the cosmic neutrino background. In: *Phys. Rev. D* 82 (2010), Sep, 062001. http://dx.doi.org/10.1103/PhysRevD.82.062001. – DOI 10.1103/PhysRevD.82.062001

[Kle14] Kleesiek, M.: *A Data-Analysis and Sensitivity-Optimization Framework for the KATRIN Experiment*, Karlsruher Institut für Technologie (KIT), Diss., 2014

[Leb11] Leber, M.: *Optimization of KATRIN Egun parameters*. July 2011. – Department of Physics, University of California, Santa Barbara, CA

[LL02] Loredo, T. J. ; Lamb, D. Q.: Bayesian analysis of neutrinos observed from supernova SN 1987A. In: *Physical Review D* 65 (2002), Nr. 6, S. 063002

[LS85] Lobashev, V.M. ; Spivak, P.E.: A method for measuring the electron antineutrino rest mass. In: *Nuclear Instruments and Methods in Physics Research Section A: Accelerators, Spectrometers, Detectors and Associated Equipment* 240 (1985), Nr. 2, S. 305–310. http://dx.doi.org/10.1016/0168-9002(85)90640-0. – DOI 10.1016/0168–9002(85)90640–0

[LVV08] Lazauskas, R. ; Vogel, P. ; Volpe, C.: Charged current cross section for massive cosmological neutrinos impinging on radioactive nuclei. In: *Journal of Physics G: Nuclear and Particle Physics* 35 (2008), Nr. 2, 025001. http://stacks.iop.org/0954-3899/35/i=2/a=025001

[MNS62] Maki, Z. ; Nakagawa, M. ; Sakata, S.: Remarks on the unified model of elementary particles. In: *Prog.Theor.Phys.* 28 (1962), S. 870–880. http://dx.doi.org/10.1143/PTP.28.870. – DOI 10.1143/PTP.28.870

[NFW96] Navarro, J. F. ; Frenk, C. S. ; White, S. D. M.: The Structure of cold dark matter halos. In: *Astrophys. J.* 462 (1996), S. 563–575. http://dx.doi.org/10.1086/177173. – DOI 10.1086/177173

[Oli14] Olive, K. A. et al. (Particle Data Group): In: *Chin. Phys. C* 38 (2014). http://pdg.lbl.gov

[OLL04] Ong, E. T. ; Lee, K. H. ; Lim, K. M.: A fast algorithm for three-dimensional electrostatics analysis: fast Fourier transform on multipoles (FFTM). In: *International journal for numerical methods in engineering* 61 (2004), Nr. 5, 633–656. http://onlinelibrary.wiley.com/doi/10.1002/nme.1081/abstract

[PBB+92] Picard, A. ; Backe, H. ; Barth, H. ; Bonn, J. ; Degen, B. ; Edling, Th. ; Haid, R. ; Hermanni, A. ; Leiderer, P. ; Loeken, Th. ; Molz, A. ; Moore, R.B. ; Osipowicz, A. ; Otten, E.W. ; Przyrembel, M. ; Schrader, M. ; Steininger, M. ; Weinheimer, C.: A solenoid retarding spectrometer with high resolution and transmission for keV electrons. In: *Nuclear Instruments and Methods in Physics Research Section B: Beam Interactions with Materials and Atoms* 63 (1992), Nr. 3, S. 345–358. http://dx.doi.org/10.1016/0168-583X(92)95119-C. – DOI 10.1016/0168–583X(92)95119–C

[Per09] Perkins, D. H.: *Particle astrophysics*. 2. ed. Oxford : Oxford University Press, 2009 (Oxford master series in physics ; no. 10). http://www.gbv.de/dms/goettingen/570868491.pdf. – ISBN 0–19–954546–4; 978–0–19–954546–9; 0–19–954545–6; 978–0–19–954545–2. – Includes bibliographical references and index. - Previous ed.: 2003

[PKW64] Pauli, W. E. F. ; Kronig, R. ; Weisskopf, V. F.: *Collected scientific papers*. New York, NY : Interscience, 1964. – Offener Brief an die Gruppe der Radioaktiven bei der Gauvereinstagung zu Tübingen (datiert 4. Dez. 1930)

[Pon57] Pontecorvo, B.: Mesonium and anti-mesonium. In: *Sov.Phys.JETP* 6 (1957), S. 429

[Pon58] Pontecorvo, B.: Inverse beta processes and nonconservation of lepton charge. In: *Sov.Phys.JETP* 7 (1958), S. 172–173

[Pon68] Pontecorvo, B.: Neutrino Experiments and the Problem of Conservation of Leptonic Charge. In: *Sov.Phys.JETP* 26 (1968), S. 984–988

[PW65] Penzias, A. A. ; Wilson, R. W.: A Measurement of Excess Antenna Temperature at 4080 Mc/s. In: *The Astrophysical Journal* 142 (1965), S. 419–421

[RC53] Reines, F. ; Cowan, C. L.: Detection of the Free Neutrino. In: *Physical Review* 92 (1953), S. 830–831. http://dx.doi.org/10.1103/PhysRev.92.830. – DOI 10.1103/PhysRev.92.830

[RCH+60] Reines, F. ; Cowan, C. L. ; Harrison, F. B. ; McGuire, A. D. ; Kruse, H. W.: Detection of the Free Antineutrino. In: *Phys. Rev.* 117 (1960), Jan, 159–173. http://dx.doi.org/10.1103/PhysRev.117.159. – DOI 10.1103/PhysRev.117.159

[RK88] Robertson, R. G. H. ; Knapp, D. A.: Direct Measurements of Neutrino Mass. In: *Annual Review of Nuclear and Particle Science* 38 (1988), Nr. 1, 185-215. http://dx.doi.org/10.1146/annurev.ns.38.120188.001153. – DOI 10.1146/annurev.ns.38.120188.001153

[RLC05] Rolke, W. A. ; Lopez, A. M. ; Conrad, J.: Limits and confidence intervals in the presence of nuisance parameters. In: *Nuclear Instruments and Methods in Physics Research Section A: Accelerators, Spectrometers, Detectors and Associated Equipment* 551 (2005), Nr. 2, S. 493–503

[RW83] Repko, W. W. ; Wu, C.-E.: Radiative corrections to the end point of the tritium β decay spectrum. In: *Physical Review C* 28 (1983), Nr. 6, S. 2433

[RW04] Ringwald, A. ; Wong, Y. Y. Y.: Gravitational clustering of relic neutrinos and implications for their detection. In: *Journal of Cosmology and Astroparticle Physics* 2004 (2004), Nr. 12, S. 005

[SAB+04] Sisti, M. ; Arnaboldi, C. ; Brofferio, C. ; Ceruti, G. ; Cremonesi, O. ; Fiorini, E. ; Giuliani, A. ; Margesin, B. ; Martensson, L. ; Nucciotti, A. et al.: New limits from the Milano neutrino mass experiment with thermal microcalorimeters. In: *Nuclear Instruments and Methods in Physics Research Section A: Accelerators, Spectrometers, Detectors and Associated Equipment* 520 (2004), Nr. 1, S. 125–131

[The14] The EXO-200 Collaboration: Search for Majorana neutrinos with the first two years of EXO-200 data. In: *Nature* 510 (2014), S. 229–234. http://dx.doi.org/10.1038/nature13432. – DOI 10.1038/nature13432

[Thü07] Thümmler, Thomas: *Präzisionsüberwachung und Kalibration der Hochspannung für das KATRIN-Experiment*, Westfälische Wilhelms-Universität Münster, Diss., 2007. http://nbn-resolving.de/urn:nbn:de:hbz:6-16539562785

[Wei62] Weinberg, S.: Universal Neutrino Degeneracy. In: *Phys. Rev.* 128 (1962), Nov, 1457–1473. http://dx.doi.org/10.1103/PhysRev.128.1457. – DOI 10.1103/PhysRev.128.1457

[Wil38] Wilks, S. S.: The large-sample distribution of the likelihood ratio for testing composite hypotheses. In: *The Annals of Mathematical Statistics* 9 (1938), Nr. 1, S. 60–62

[WS12] Winslow, L. ; Simpson, R.: Characterizing Quantum-Dot-Doped Liquid Scintillator for Applications to Neutrino Detectors. In: *JINST* 7 (2012), S. P07010. http://dx.doi.org/10.1088/1748-0221/7/07/P07010. – DOI 10.1088/1748–0221/7/07/P07010

[Yep14] Yepez, Krochin P. A.: *Investigations on the influence of the ortho-para tritium ratio on the neutrino mass sensitivity of KATRIN*, Karlsruher Institut für Technologie (KIT), Bachelor Thesis, 2014

LIST OF ACRONYMS

CAD	computer-aided design
CMB	cosmic microwave background
CMS	calibration and monitoring system
CP	charge parity
CPS	cryogenic pumping section
CPU	central processing unit
CR	cosmic ray
DPS	differential pumping section
E-gun	electron gun
EMD	electromagnetic design
FFTM	fast Fourier transform of multipoles
FSD	final state distribution
GPU	graphics processing unit
KATRIN	KArlsruhe TRItium Neutrino
KGS	KATRIN global simulation
KIT	Karlsruher Institut für Technologie
MIT	Massachusetts Institute of Technology
MTD	measuring time distribution
RSCM	recondensing super conducting magnet
SM	Standard Model of particle physics
SSM	standard solar model
STS	source and transport section
TMP	turbo-molecular pump
UHECR	ultra-high-energy cosmic ray
WGTS	windowless gaseous tritium source

ACKNOWLEDGEMENTS

Finally, I want to express my gratitude that I was given the chance of being part of the KATRIN collaboration during this work. I would like to thank all the persons supporting me friendly and professionally during the work on this thesis. In particular, I want to give thanks to

- Prof. Guido Drexlin for the interesting and challenging scope of this work; and for providing the possibility to participate in the Neutrino2014 conference in Boston with subsequent stay at MIT,
- Prof. Ulrich Husemann for the evaluation of this thesis as second reviewer,
- Dr. Kathrin Valerius for her supervision, reflecting her enthusiasm for physics, and her great effort in proofreading this document,
- Dr. Martin Babutzka for sharing my office and the Döner excursions; furthermore for explaining the Rear Section to me and solving numerous general computing problems (especially with regards to Kalinka and Tesla), not to forget his lovely relationship to apples and his effort in proofreading this thesis,
- Dr. Marco Kleesiek for the exhaustive KaFit support, especially for MINUIT & MINOS, answering general statistics questions and providing corrections to this thesis,
- the Richard-Winter Stiftung for financial support of this thesis,
- Prof. Joe Formaggio for inviting me to the MIT and encouraging me in the relic neutrino topic,
- John Barrett for answering my countless computing questions during my stay at MIT,
- Katharina Fischer and Marie-Christine Kauffmann for their patience in planning my stay abroad,
- Laura Kuckert for sharing my office and amusing Martin and me with her cellphone ringtones,
- Birgit Adams for sharing the way to work,

- Dr. Susanne Mertens for fruitful discussions on the relic neutrino topic,
- Nikolaus Trost, Daniel Hilk and Stefan Groh for extensive KASSIOPEIA support,
- all readers and correctors of this thesis,
- all who have been forgotten on this list...

Special thanks goes to my family and all my friends, especially F. Tresp, for their patience and support during this work.

AFFIDAVIT

Herewith I affirm that I wrote the current thesis on my own and without the usage of any other sources or tools than the cited ones and that this thesis has not been handed neither in this nor in equal form at any other official comission.

Florian Heizmann